EFFECTS OF THERMAL PROCESSING VARIATIONS ON MICROSTRUCTURE AND HIGH CYCLE FATIGUE OF BETA-STOA TI-6AL-4V

by

Byron McArthur

A thesis submitted to the Faculty and the Board of Trustees of the Colorado School of Mines in partial fulfillment of the requirements for the degree of Master of Science (Metallurgical and Materials Engineering).

Golden, Colorado

Date _____

Signed: _____
Byron McArthur

Signed: _____
Dr. Michael Kaufman
Thesis Advisor

Signed: _____
Dr. Amy Clarke
Thesis Advisor

Signed: _____
Dr. Angus Rockett
Department Head of
Metallurgical and Materials Engineering

ABSTRACT

Titanium alloys are often used in fatigue-limited structural applications within the aerospace industry. Because of the primary processing control and reactivity of titanium, the fatigue life of the material is predominantly dependent upon the α-phase microstructure, rather than internal defects such as voids or inclusions. For titanium alloy Ti – 6 wt % aluminum - 4 wt % vanadium (Ti-6Al-4V), the influence of cooling rate from above the ß-transus is known to affect the resulting microstructure and influence high cycle fatigue life. The transfer time from the furnace to the water-quenching bath significantly influences the cooling rate, and thus controls the microstructural development and fatigue properties. A hydraulic actuator produced from a Ti-6Al-4V forging failed prematurely during fatigue testing, and provided the industrial motivation for this work. A quench dilatometer was used, along with subsequent scanning electron microscopy, to explore the microstructural variations produced as a function of thermal history. Rotating bending fatigue testing in the high cycle fatigue regime highlighted a two orders of magnitude reduction in fatigue life due to an increased quenching transfer time. The increased quench transfer time was shown to create packets of co-oriented α laths that facilitated crack initiation. Fatigue crack growth rate measurements were also used to quantify post-initiation crack growth rates in microstructures produced by different quench delay times. Long crack growth rates were found to be similar for short and long quench delay times. Post-mortem fractographic analysis and electron back scattered diffraction aided in determining the microstructural influence on fatigue crack initiation and propagation, indicating that long, planar basal slip lengths contribute to crack nucleation. Based upon these findings, it is found that even minor variations in quench transfer time can significantly influence the high cycle fatigue life of titanium alloys.

TABLE OF CONTENTS

LIST OF FIGURES

LIST OF TABLES

ACKNOWLEDGEMENTS

Without the guidance and assistance from a multitude of people, the author would not have had the opportunity to pursue this project. The group at Triumph Aerospace Systems – Seattle, including Dr. Nicholas Nagel, Gordon Francis, Brian Reiling, Russel Gibson and James Garnish, gave the author the chance to explore an industrially-relevant metallurgical topic in an academic environment. The faculty in the Center for Advanced Non-Ferrous Structural Alloys (CANFSA) group of the Metallurgical and Materials Engineering department at Colorado School of Mines oversaw the project, with valuable input from industrial sponsors. The author's advisors for this project, Dr. Michael Kaufman and Dr. Amy Clarke, gave the freedom to approach this project from various perspectives, with a breadth of different analytical techniques, while giving great direction and insight when needed. Mentors from sponsoring companies gave perspectives on processing and material applications that were key for maintaining industrial relevance for the project. Fellow students were greatly helpful with equipment training, as well as metallurgical concept and theory discussions. Finally, the author would like to thank his family for their continuous moral support throughout graduate school.

CHAPTER 1: INTRODUCTION

The long term success of the aerospace industry is attributable to reliable, lightweight, high performance designs and materials. Fatigue limited components require material testing to determine design stresses and to evaluate "acceptable" defects for ensuring statistically-based service life remaining in the component. Coupon fatigue testing is often performed as a method of determining acceptable design stresses for the end component. Further testing of the component in higher level assemblies is performed to ensure design and manufacturing quality. Environmental contributions and surface conditions, such as rock chips, marine environments, tropic and arctic temperatures, and abrasive contaminant wear must also be considered to accurately represent service conditions.

In this project, the case study of a helicopter's hydraulic damper unit is a prime example of a fatigue limited part with demanding structural and environmental requirements. The rotation of the helicopter rotor head imparts a constant velocity and drag force on each blade. Forward motion of the aircraft creates a difference in velocity of the advancing (faster) blade and receding (slower) blade in the surrounding air. The cyclical forces on each blade creates vibrations that are damped out of the system by the hydraulic damper unit, which experiences nearly 100 million cycles over the course of its service life. To accomplish the weight, strength, service temperature and environment requirements, the component is made from a titanium alloy (Ti-6Al-4V) forging.

During controlled, accelerated laboratory testing with telemetry equipment, the loss of function of several test hydraulic damper units prompted a failure analysis. In Section 4.1 of this report, hydrogen cracking, chlorine induced corrosion-fatigue, stress corrosion cracking and undesirable microstructural features were explored as possible causes of failure. No environmental contributions were present, but anomalous crack morphology was consistently associated with the underlying microstructure. A review of the literature regarding heat treatment operations and resulting microstructures (Section 2.4) demonstrated that the Ti-6Al-4V material in question likely underwent improper heat treatments, producing the suspected deleterious microstructural features. The deformation mechanisms (Section 2.5) and anisotropic behavior of titanium alloys, combined with the microstructural dependence of short crack growth and high cycle fatigue life (Section 2.6) supported the theory of premature failure.

Unfortunately, existing literature [1] connecting heat treatment operations to produced microstructures, in the form of constant cooling rate transformation (CCT) and time-temperature-transformation (TTT) plots, is limited and often produced from questionable testing methods. To address this, these respective plots were created through dilatometry, as reported in Section 4.2. Slow cooling from the furnace temperature, due to radiative and convective cooling during the material transfer time from the furnace to quenching media, produced the microstructural features observed in the original

material of the case study, confirming an improper heat treatment via retrospective analysis of the microstructure.

Anomalous crack paths observed in metallographic specimens of the case study material were characterized based upon relation to the microstructure and crystallographic orientation. Section 4.4 shows the short cracks propagate through low energy dissipation mechanisms. Fatigue crack paths were observed to propagate through grain boundaries and across multiple microstructural features, with little impedance to growth.

Rotating bending fatigue testing of smooth Ti-6Al-4V specimens heat treated in accordance with the titanium alloy specification (termed “ideal”) in comparison to the improper heat treatment (termed “representative”) in Section 4.5 demonstrates a reduction in fatigue life of smooth specimens of more than two orders of magnitude. Measurement of the initiated fatigue crack growth rates in Section 4.6 were similar for both microstructures, indicating the importance of heat treatment on the fatigue crack initiation stage, as well as overall high cycle fatigue life. Through heat treatment mapping, microstructural development analysis, fatigue crack path analysis, and fatigue testing, the effects of a delayed water quench operation were demonstrated to reduce the high cycle fatigue performance of the material.

CHAPTER 2: LITERATURE REVIEW

2.1 Introduction to Titanium Alloys

Titanium and its alloys offer material properties, including high specific strength, excellent corrosion resistance, biocompatibility and moderate temperature (540°C) mechanical properties [2] that are attractive for many industries and applications. However, due to high material, processing and machining costs, titanium is predominantly used by the aerospace and medical industries [2]. These high material costs are associated with the reduction process to remove oxygen from the titanium minerals rutile (TiO_2) and ilmenite ($FeTiO_2$) [3].

The titanium alloy containing 6 wt% aluminum and 4 wt% vanadium (commonly referred to as Ti-6Al-4V or Ti-6-4) is the predominant alloy used by many industries. Applications within the aerospace industry include turbine discs, compressor blades, actuator housings, helicopter rotor heads, airframe components, and more. Ti-6-4 was developed in the 1950's for high strength properties at low to moderate (400 °C) temperatures. The specific strength of Ti-6-4 is rivaled only by ultra-high strength steels and a few aluminum alloys, and in many cases, still offers better heat treatment section thickness capabilities (to retain homogenous properties) and corrosion resistance.

Unalloyed titanium undergoes an allotropic phase transformation with increasing temperature, going from a hexagonal close packed (HCP) α phase to a body centered cubic (BCC) β phase at 883 °C [3]. Impurity elements such as oxygen, hydrogen, nitrogen, carbon, and iron may exist as a result of primary solidification and secondary thermomechanical processing; the interstitial elements have a significant solid solution strengthening effect on the α phase. Commercially pure (CP) titanium grades 1-4 designate allowable impurity contents and minimum mechanical properties, with tensile yield strengths ranging from 240 MPa to 550 MPa.

Titanium alloys are separated into groups based upon their phase fractions of α and β. Alloying elements are separated into groups based upon which phase they stabilize. Simple metals, whose conduction electrons are in the *s* or *p* shells, are often α stabilizers; transition metals, whose conduction electrons are in the *d* shell, are often β stabilizers. Examples of α stabilizers are aluminum, gallium, and tin. Stabilizing elements for the β phase are further classified into isomorphous or eutectoid. Isomorphous β stabilizers, such as vanadium, molybdenum and zirconium, promote a mixed two phase region of α + β that leads to increasing amounts of retained β. Eutectoid β stabilizers, such as chromium, iron, manganese, and nickel act similarly to isomorphous β stabilizers, but they promote the formation of an intermetallic compound at higher alloying contents and/or lower temperatures [3].

The combined effect of 6 wt% aluminum and 4 wt% vanadium, α and β stabilizers, respectively, in Ti-6-4 is to increase the ß-transus temperature from 883 °C to approximately 995 °C [3] and create a two-phase field of α + β. The phase fraction of remaining β in Ti-6-4 at room temperature is approximately 2-5% and varies with thermomechanical processing and heat treatment.

2.2 Post-Casting Titanium Processing

Microstructures of α + β and near-α titanium alloys are characterized based upon the α morphology. These microstructures are produced through several operations after the material is solidified from casting. Ingots of titanium are cycled through forging operations above and below the β transus to obtain higher compositional homogeneity. The last operation of thermomechanical processing (TMP) is a high deformation/reduction operation in the α + β phase field that results in equiaxed α dispersed throughout the β matrix; this α morphology is often incorrectly described as "primary-α" (the equiaxed α do not form upon solidification), but the nomenclature persists. The microstructure resulting from high amounts of deformation during the α + β phase field hot working operation is called the mill annealed condition, which is illustrated schematically as the first operation in Figure 2.1. A microstructure produced from this is represented in Figure 2.2a. Heating this material into the α + β phase field, typically 50-150 °C below the β-transus, transforms a fraction of the α to ß as defined by the pseudo-binary (equilibrium) phase diagram and hold temperature. Cooling from this intermediate temperature produces a "duplex" microstructure composed of the pre-existing equiaxed α and newly formed laths of α [3].

Heating the mill-annealed microstructure above the β-transus transforms all of the equiaxed α into ß. Through competitive grain growth mechanisms and a lack of grain boundary α (GBα) to pin β grain boundaries, the β grains grow at a logarithmic rate to rapidly reach 300 µm in diameter within 4 minutes [4]. Due to the low thermal conductivity and large section thicknesses, industrial specifications [5] require all regions of the material are soaked above the β-transus for at least 30 minutes, which produces β grain sizes on the order of 500 µm in diameter.

Cooling from the β phase field produces lath-shaped α; equiaxed α only occurs as a result of hot deformation processing. These α laths may form in two different morphologies, depending on the cooling rate. Slower cooling promotes allotriomorphic α formation at the grain boundaries that subsequently form colonies (or packets) of α side plates that grow into the β grain as cooling proceeds. The colony size, α side plate thickness, and inter-lath retained β increase as the cooling rate decreases. This microstructure is often called β-annealed, due to the slow cooling rates, and is sometimes incorrectly described as a lamellar microstructure due to the α morphology. The processing route for ß annealed microstructures is

illustrated schematically in Figure 2.1, along with a typical microstructure in Figure 2.2b. Rapid cooling, often achieved through water quenching, promotes an acicular microstructure of multi-variant α' laths through a reported martensitic transformation of β → α'. This microstructure is also described as Widmänstatten, and is produced from the ß solution treated steps in the processing schematic of Figure 2.1, resulting in the microstructure in Figure 2.2c.

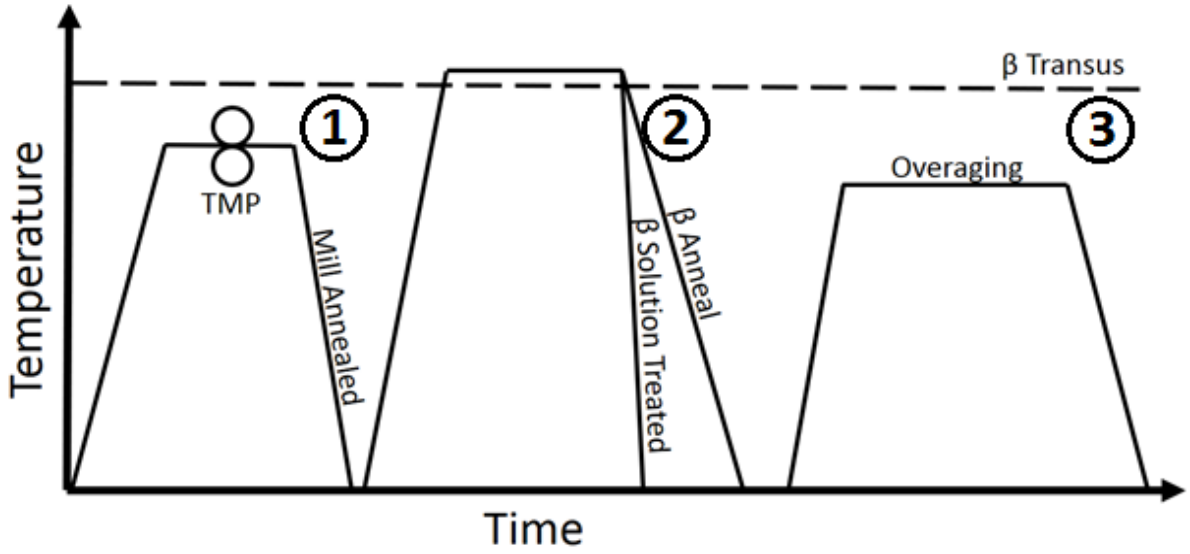

Figure 2.1: Schematic of heat treatment operations to produce varying microstructures of α + ß titanium alloys. Elevated temperature thermomechanical processing (TMP) of the material in Stage 1 breaks up the α laths and produces spherical or elliptical α. Stage 2 is performed when ß heat treating of the material is required, and varying cooling rates produce different α morphologies. Stage 3 represents the aging or overaging procedure performed for relief of residual stresses and partitioning of vanadium after any preceding quenching operations.

2.3 Industrially-Relevant Titanium Heat Treatments and Microstructures

Industrial use of Ti-6Al-4V is often in the mill annealed (MA), duplex annealed (DA), or solution treated and aged (STA) condition. In each case, the material starts from a condition with equiaxed α grains within a β matrix, resulting from thermomechanical processing; this is the "as-received", or MA condition produced in Stage 1 of Figure 2.1. One parameter that subsequent heat treatments vary is the peak temperature that determines the phase fraction of α that is transformed into the ß matrix at a given temperature. Cooling rate is the other controllable variable, which establishes the α lath morphology that forms. The cooling rate is the difference between the ß anneal (low) and ß solution (high) treatment of Stage 2 of Figure 2.1. Duplex annealed microstructures form from heating the starting MA material into

the sub-ß-transus region, which varies the fractions of initial equiaxed α and α laths (in co-oriented packets), depending upon the peak temperature, "soak" time at temperature, and the ß-transus of each specific lot of material. Unintentional DA microstructures may occur from insufficient thermomechanical processing (TMP) during precursor processing, particularly in large-section thicknesses. The STA heat

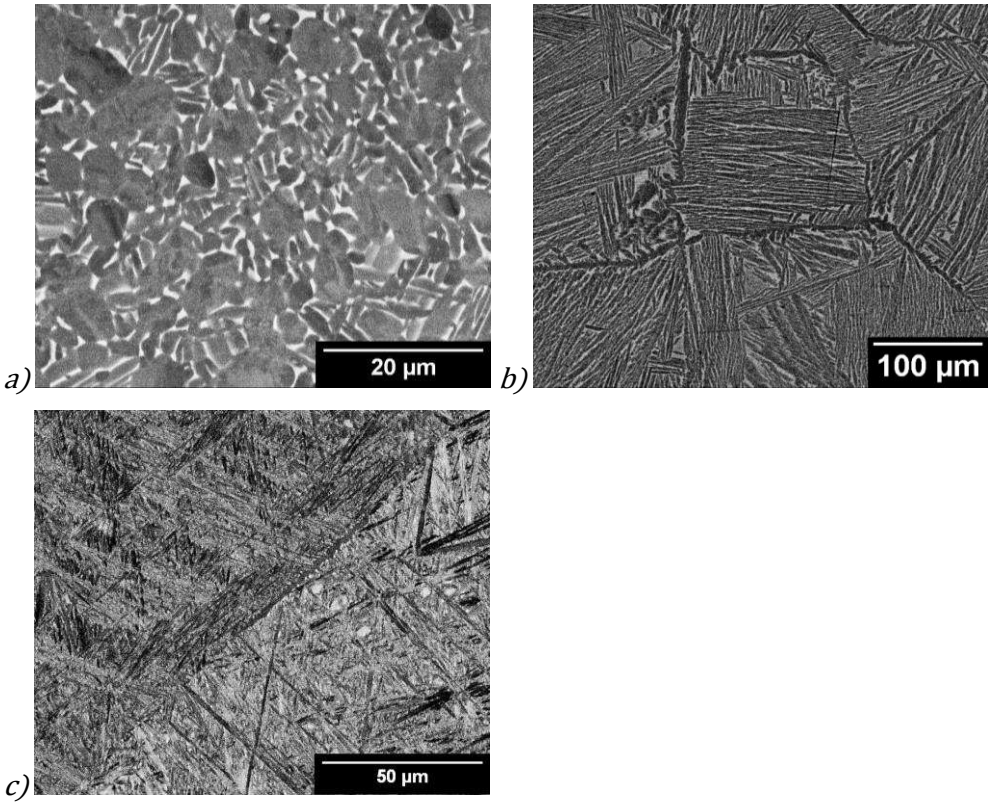

Figure 2.2: a) Mill annealed, b) Beta annealed and c) Beta solution treated and overaged Ti-6-4 microstructures.

treatment is one of the most common heat treatment conditions for Ti-6-4 and other α + ß titanium alloys. The heating for STA is similar to the DA, in that the peak temperature is sub-ß-transus, but rapid water quenching produces multi-variant α' laths between dispersed, equiaxed α. Water quenched material is often aged at intermediate temperatures, as shown schematically as Stage 3 in Figure 2.1, to allow for vanadium partitioning and stress relief, while not transforming an appreciable amount of α to ß.

Industrial use of ß heat treatments (exceeding the ß-transus) in α + ß alloys is not typical. Low thermal conductivity of titanium requires relatively long hold times (typically 30 minutes to 2 hours, depending on section size) to achieve full transformation of α to ß. This atmospheric exposure at high temperature and times causes increased oxygen and hydrogen absorption that is undesirable. Alloy segregation in the ingot from primary and secondary processing may cause variations in ß-transus

temperature; a super-heat of 50 °C is often required to compensate for this, but also increases the oxygen absorption and ß grain growth. ß-annealing is the common industrial ß heat treatment, in which a slow cooling may be performed by removing the part from the furnace, or simply turning off the furnace (i.e. furnace cool). Alternatively, water quenching from above the ß-transus can be performed, which produces the ß solution treated condition. After quenching, the part is then overaged, as previously discussed, and this process is called a ß solution treated overaged, or ß-STOA. The over-aging temperature of 700°C to allow vanadium partitioning is low enough that there is no appreciable increase in ß phase fraction (still only 4.6 volumetric percent at 700°C), and is high enough that short range ordering or precipitation of Ti_3Al does not occur. Vanadium partitioning to equilibrium phase compositions allows for stable mechanical properties and decomposition of any soft orthorhombic α" martensite [3].

2.4 Phase Transformations of ß to α in Ti-6Al-4V

As reflected by industrial use, literature on ß heat treatments, particularly the ß-STOA condition, is sparse. Several unconfirmable anecdotes from U.S. D.O.D. suppliers suggest that the ß-STOA heat treatment may have been internally explored (at competing corporations) during the 1980's, and only some companies decided to pursue its use. This industry research was likely never published for intellectual property and/or government restrictions. As this project primarily focuses on the influence of industrially relevant heat treatments, particularly above the ß-transus, the morphology that results from the ß → α transformation and effects from crystallographic relations is explored.

Ahmed et al. [1] examined the phase transformations in Ti-6Al-4V utilizing a Jominy end quench bar. In this test, a bar of material insulated along its sides is quenched on one end from an elevated temperature. This process results in varying cooling rates as a function of distance from the quenched end. The bar is then sectioned and analyzed to create a continuous cooling transformation (CCT) diagram. Ahmed used a ß solution temperature of 1050 °C for 30 minutes for ß-STOA heat treatment. High cooling rates of 525 °C/s were reported to produce purely martensitic multivariant α', as shown through micrographs and transmission electron microscopy (TEM) analysis, displaying regions of stacking faults and twin substructures in the α' laths. At a lower cooling rate of 410 °C/s, grain boundary α (GBα) formation was observed, with a massive transformation reportedly occurring in colonies dispersing from the GBα. This massive transformation was reported to increase in phase fraction relative to α' with decreasing cooling rates (down to 20 °C/s) at prior ß GBs, as well as through sympathetic growth off of martensitic α' plates. At cooling rates lower than 20 °C/s, Ahmed et al. reported increasing diffusional growth of GBα extending into prior ß grains. At these lower cooling rates, two types of GBα were observed. Jagged, discontinuous GBα was associated with a lower transformation temperature, controlled

by interfacial diffusion and ledgewise diffusional growth. Straighter, and more continuous GBα was associated with higher transformation temperatures.

Surprisingly, the work performed by Ahmed et al. provides some of the only available ß heat treated transformation-temperature information for Ti-6Al-4V. However, the test method for the Jominy end bar provided a variable cooling rate as a function of temperature, as seen in Figure 2.3, and transformation temperatures as a function of cooling rate were unresolvable. Despite this, a CCT plot was constructed for the reported cooling rates (Figure 2.4). This CCT diagram shows a massive transformation (α_m) occurring between cooling rates between 20°C/s and 410°C/s, between diffusional (α) and martensitic (α') transformations. Additionally, the identification of GBα, massive α and α laths were based upon light optical microscopy (LOM), TEM, and energy dispersive spectroscopy (EDS) techniques, which may be explainable through alternative theories of allotriomorphic side plate growth.

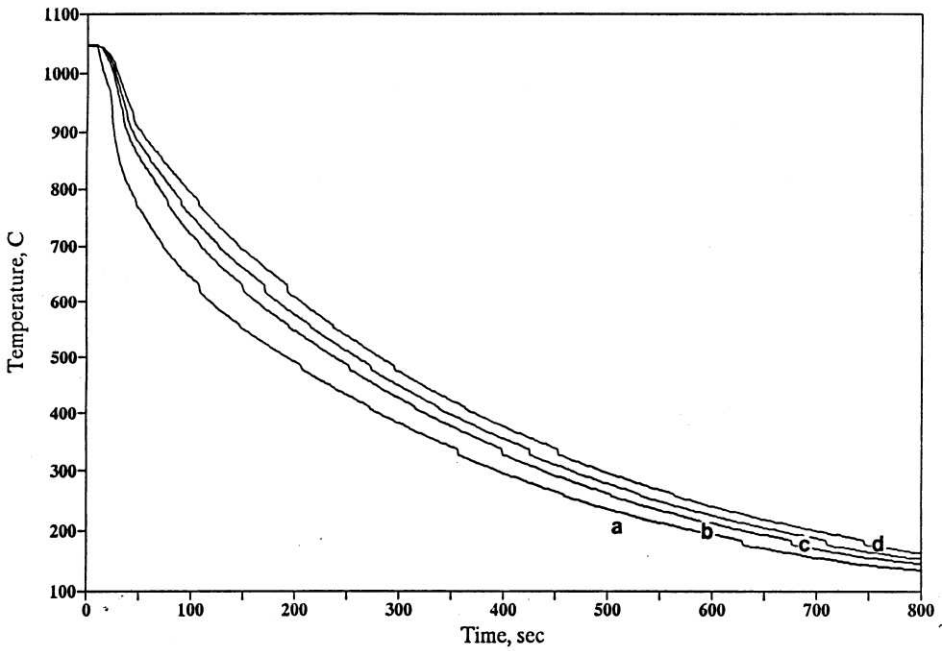

Figure 2.3: Temperature vs. time plots for distances from quench surface of a) 3.2, b) 9.5, c) 12 and d) 15.2mm from Jominy end bar tests. [1]

Microstructures produced from lower cooling rates of 0.24 °C/s to 5 °C/s were explored by Gil et al. [6]. ß solutionizing temperatures and times were also varied to explore the effects on ß grain size and precipitated α morphology. These cooling rates and temperatures are within the range of ß annealed heat treatments for varying section thicknesses. The authors reported α colonies of decreasing sizes and thicknesses associated with increasing cooling rates, as expected with lower bulk diffusion rates at lower temperatures. Additionally, the GBα continuity and thickness decreased with increasing cooling rates.

Jagged GBα morphology was occasionally observed, but no association with cooling rate was discernable. Interestingly, as the ß grain size increased by increased temperature above the ß transus or at longer times, the α lath thicknesses decreased. This was reported by Gil et al. to be caused by the

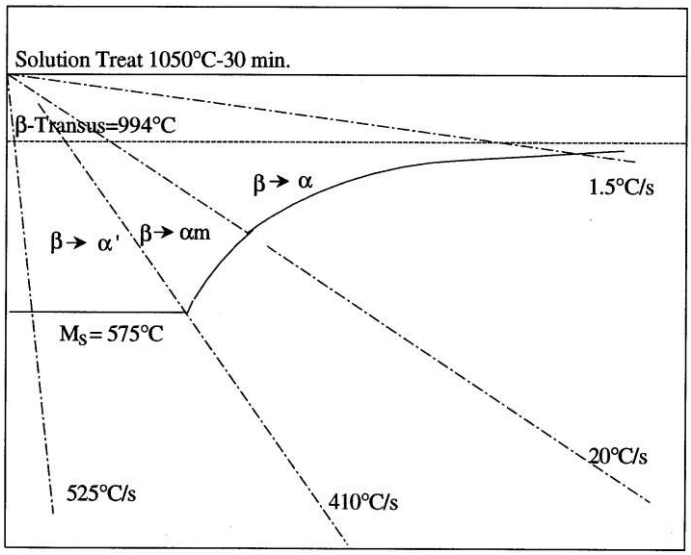

Figure 2.4: CCT plot by Ahmed et al. for Ti-6-4 showing microstructures produced with various cooling rates. [1]

decreased starting temperature for the ß → α diffusional transformation associated with longer diffusion distances, due to less GB area.

The α precipitation that occurs through long-range diffusional growth appears to be preceded and controlled by allotriomorphic GBα formation. This is expected, as grain boundaries offer easy nucleation sites for second phase precipitation, as well as faster diffusion than within the bulk of the grain [7]. The morphology of GBα is of interest, as it has an influence on the subsequent colony growth of α side plates that form. A 3-D reconstructive analysis of GBα was performed by Sharma et al. [8] on an α + ß titanium alloy (Ti-4.3Fe-6.7Mo-1.5Al) with a high volume fraction ß that was held in the α + ß temperature region to promote diffusional growth. Serial sectioning and electron back scattered diffraction (EBSD) analysis allowed for combined information of ß grain orientations and true morphologies of various α precipitates. Initial observations prior to sectioning showed apparent discontinuous, jagged (or "zig-zag") GBα morphology and intragranularly precipitated α. By performing serial sectioning, the discontinuous GBα was shown to be a single (continuous) grain branching out in a coral like fashion, as seen in Figure 2.5. This microstructural reconstruction, and others, showed the GBα appearing to originate from ß-GB corners and/or edges, growing into the rest of the GB.

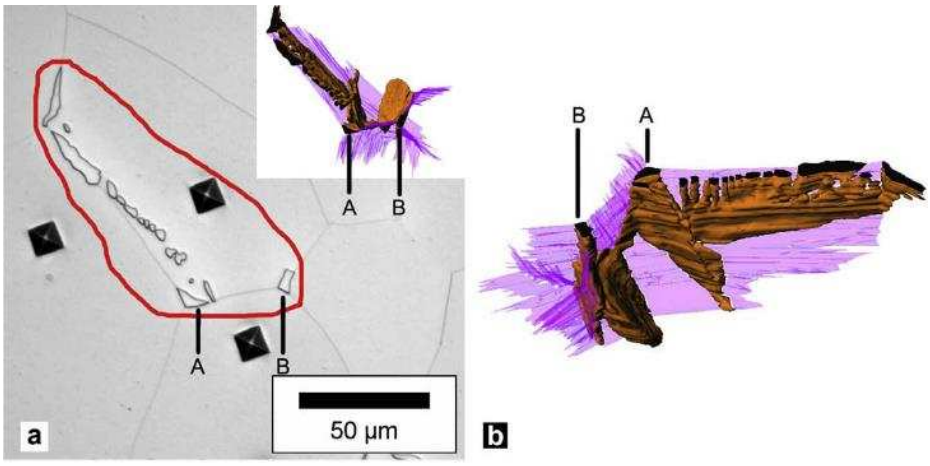

Figure 2.5: (a) 2-D viewing of zig zag GBα and (b) 3-D representation showing seemingly discontinuous GBα as a single α grain. GBα is denoted by the orange, and prior ß GBs shown in purple [8].

From EBSD orientation information, the authors demonstrated the zig-zag morphology to occur with branched GBα growth between the ß grains that maintain a low misorientation angle between $\{110\}_{ß}$ planes. This is caused by the $\{110\}_{ß}||\{0001\}_{\alpha}<\bar{1}11>_{ß}||<11\bar{2}0>_{\alpha}$ Burger's orientation relationship (BOR) [9] that the hexagonal close packed (HCP) α maintains with the matrix body centered cubic (BCC) ß phase. Accordingly, the α attempts to maintain $(0001)_{\alpha}$ alignment with $\{110\}_{ß}$ of both ß grains when possible and forms branches with steps. Note that the {110}ß planes are not the habit planes of the GBα. The remaining $ß_1$-$ß_2$ grain boundary between GBα, Figure 2.6, orients itself during α growth to maintain low interfacial area and energy. Higher misorientations of the $\{110\}_{ß}$ planes of neighboring ß grains (with respect to each other) were found to create more steps and branches required for growing GBα.

Two additional observations were made by the authors [8]. The first is that the α formation that appeared to be intragranularly precipitated via 2-D viewing actually grew from the GBα. This is in contradiction with the 2-D based observations from Ahmed [1]. Sharma et al. provided more compelling evidence through serial sectioning observed in Figure 2.5. The second important observation is that the GB between two ß grains that have near $\{110\}_{ß}$ planes is preferred for nucleation and growth of α. ß grains with higher misorientation angles follow at higher undercoolings and driving forces.

After GBα formation, intragranular α formation occurs through primarily through two mechanisms; diffusional side plate growth off of GBα (as previously described to occur in the mill annealed condition) at slow cooling rates, or through more displacive/reconstructive methods at higher cooling rates (typical for solution treated/quenched conditions). Note that sufficiently high cooling rates, as shown later, may suppress GBα formation entirely. The diffusionally formed, large α colonies are sometimes hundreds of microns in length and width, and are thought to negatively influence mechanical properties. Because of this, understanding their growth and characteristics is important.

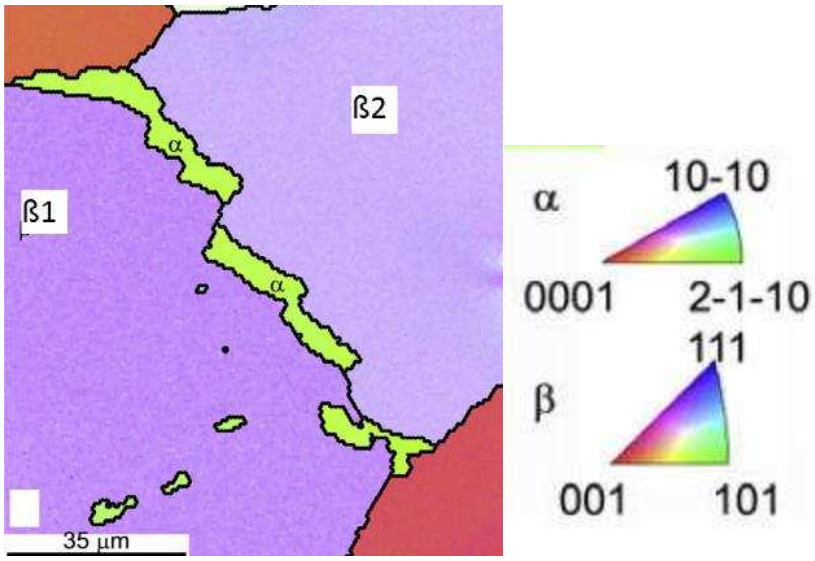

Figure 2.6: Jagged GBα formation between two ß grains that have a low misorientation angle between {110} planes. This particular pair of ß1 and ß2 neighboring grains were close to a common {110}, thus producing few steps in the GBα. [8]

Bhattacharyya et al. [10] performed an orientation analysis using EBSD and TEM on a ß annealed α + ß titanium alloy. Of the α colonies formed, there appear to be similar orientations between colonies of significantly different growth directions, as depicted in two pairs of colonies in Figure 2.7. Orientation analysis showed roughly a 10.5° rotation about the $(0001)_\alpha$ plane between the like colored colonies.

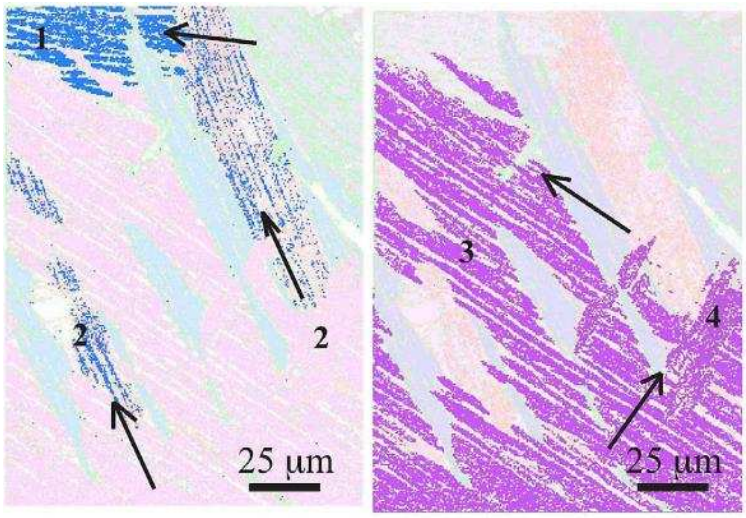

Figure 2.7: Two pairs (1-2 and 3-4) of α colonies with similar orientations, but different spatial alignment in Ti-6Al-2Sn-4Zr-6Mo. [10]

This 10.5° angle is associated with a different α variant that is on the same {110} plane. This small crystallographic angle rotation causes a different $<11\bar{2}0>_{\alpha}||<111>_{ß}$ pair to be active and creates a 70.5° misorientation. The invariant lines (i.e.; growth directions) for the α laths along the $<335>_{ß}$ directions change in a similar manner. The invariant line and the $<110>_{ß}$ form the macroscopic plane of $\{11\ \overline{11}\ 13\}_{ß}$ that the α laths lie on, which forms an 80.6° angle when viewing down the $<0001>_{\alpha}$ [10]. It should be noted that the habit plane can change with composition that modifies the c/a ratio of the α phase. This explanation is shown schematically in Figure 2.8, producing large misorientations between α lath habit planes for a small crystallographic misorientation angle, due to different variant selections.

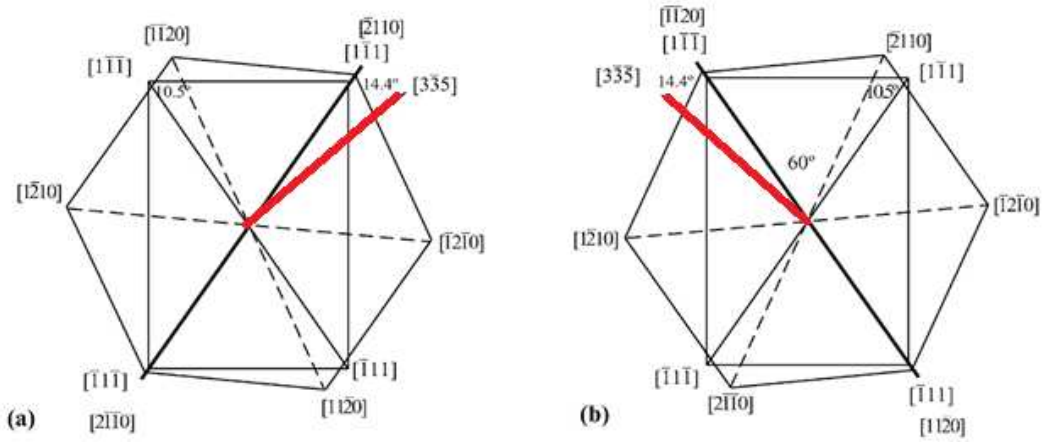

Figure 2.8: Orientation overlays for $\{110\}_{ß}$ and $(0001)_{\alpha}$ planes of two different variants (a) and (b) for an ideal Burger's orientation relationship, with habit planes for α precipitation highlighted in red. Note the large angular shift in the habit plane resulting from a 10.5° rotation in the α structure [10].

Changing focus from comparing α colonies within one ß grain to those on either side of a GB, Bhattacharya et al. found the GBα to form with a Burger's orientation relationship (BOR) to the ß grain that maintained the smallest angle between the closest packed planes and the ß GB plane, corroborating Sharma's results. The two ß grains nearly shared a common $\{110\}_{ß}$ plane (with a rotation about the $\{110\}_{ß}$ pole) that permitted colony α formation into both ß grains sharing the same $(0001)_{\alpha}$ plane. This occurred quite commonly, despite many other $\{110\}_{ß}$ planes available to the side plate α. The α colony in the second ß grain (denoted 'Q' in Figure 2.9) does not maintain a perfect orientation with the GBα, but grows via the closest variant and maintains nearly the same $\{110\}_{ß}$ to form on. Selection for the 'Q' variant follows the rule supported by Bhattacharya et al.'s work for minimizing the angle between the $[11\bar{2}0]_{\alpha}||[111]_{ß}$ and the geometric GB plane.

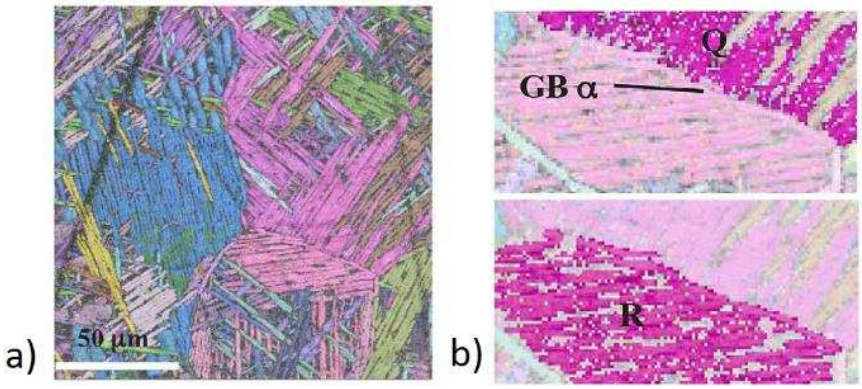

Figure 2.9: a) Orientation map of α colonies within 3 separate ß grains. b) Higher magnification of two colonies on opposite sides of a prior ß-GB. Material is Ti-6Al-2Sn-4Zr-6Mo. [10]

Alternatively, rapid quenching from above the ß-transus reportedly causes martensitic transformation that forms mixed orientation α laths in a non-packet-like morphology, as shown in Figure 2.10. In HCP α' formation, a near perfect BOR of the closest packed planes and directions within the BCC and HCP structure is maintained, with variations based upon specific alloy composition. The α' laths lie close to a {334} habit plane; minor variations in orientation relationship and habit plane are a function of alloying composition [9][11].

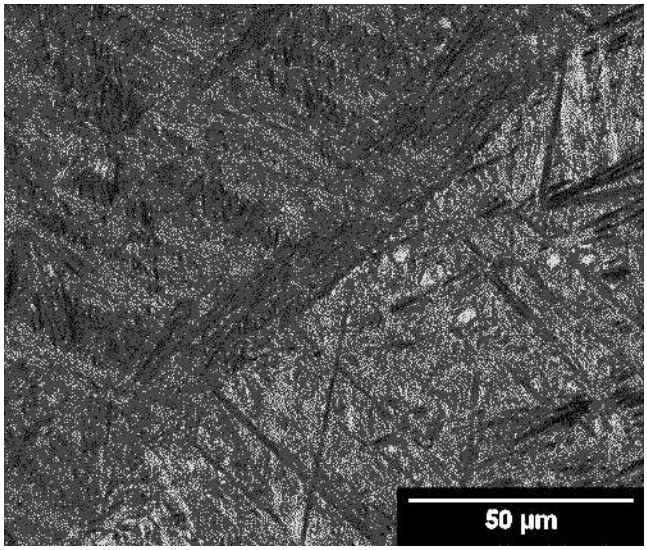

Figure 2.10: Ti-6-4 rapidly quenched from above the ß-transus to produce multivariant α'. Note that GBα is still occasionally able to form.

In a truly displacive and diffusionless trasnformation, such as martensite, a necessary reduction in symmetry must occur [12]. Thus, for the transformation of ß → α' going from a body centered cubic to hexagonal structure, an intermediate structure appears to be necessary, as well as a reconstructive method

for increasing the symmetry. An orthorhombic structure accommodates the subgroup requirements of both the BCC and HCP structures. Srinivasan et al. [13] performed pressure based modeling to view the transformation pathway of the Burger's model for BCC to HCP. A preliminary reduction in possible intermediate structures found an orthorhombic structure to meet the requirements, with the same space group as the orthorhombic α" martensite already discovered in ß-stabilized titanium alloys. Furthermore, the modeling demonstrated the orthorhombic structure existing between the BCC and HCP structures, as seen in Figure 2.11, based on energy considerations.

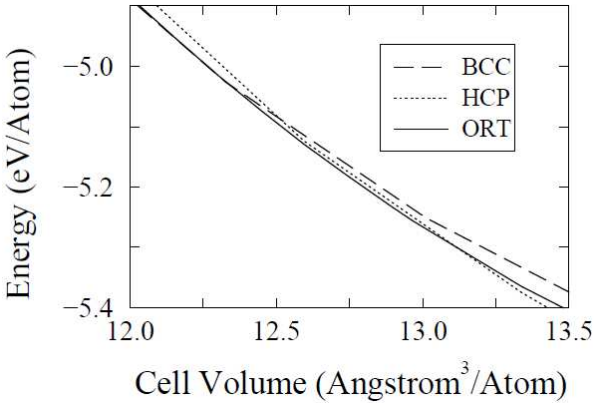

Figure 2.11: Stability of different structures during BCC:HCP transformation, showing an orthorhombic structure as a stable intermediate phase. [13]

Experimental work appears to support this theory, as the same α" structure was precipitated from the parent ß through a stress-induced transformation of a quenched metastable-ß titanium alloy [14]. Aging of this α" phase at a relatively low temperature caused both a shape memory effect, reverting back to the parent ß, as well as a α" → α decomposition. The low temperature decomposition to α supports the theory of a short-range reconstructive component from the intermediate orthorhombic structure to the HCP structure. This reconstructive component is thought to be a shuffling of alternating directions of the $\{110\}_{ß}$ planes [13]. The reversion of the α" to the parent ß phase is indicative of the displacive component of the transformation, supported by a theory requiring reversible martensite transformations to maintain a group-subgroup relation between the parent-product [12]. These group-subgroup relations allow displacive transformations [13]. While these results are not immediately or directly applicable to the results of this work at this time, acknowledging the lack of data in this area may prompt new research to further alloy and heat treatment development of titanium alloys.

A complete ß → α' transformation occurs with sufficient cooling rates, with subsequent reformation of ß upon aging; maintaining its original orientation [15]. Increased ß stabilizers, such as vanadium, promotes an α" orthorhombic structure that fully replaces α' formation at 15 wt% V in a 6 wt% Al titanium alloy, as shown in Figure 2.12.

In a study by Beladi et al. [16], two similarly processed Ti-6-4 samples were processed to evaluate the effects of different ß → α transformation morphologies. The slow cooled material with colony α formation was used as a baseline comparison for the martensitic α' microstructure. Their results showed a similar texture was produced for water quenched and annealed material, but significantly less texturing was produced for the quenched specimen. The similarity in texture is likely a result of the parent ß texturing; as for the magnitude, the α' laths initiate and propagate at higher undercoolings where the differences in activation energies between variants is less influential than when ß grain boundary and subsequent GBα promotes preferential variant selection during slow cooling. Preferred selection of α' variants was apparent through area fraction analysis of EBSD orientation maps, as shown in Figure 2.13, which shows a comparison of random (calculated) versus measured intervariant angles based upon a selected baseline variant "V1". Spatial clustering of variants was proposed to be the result of mutual accommodation of induced transformation strains.

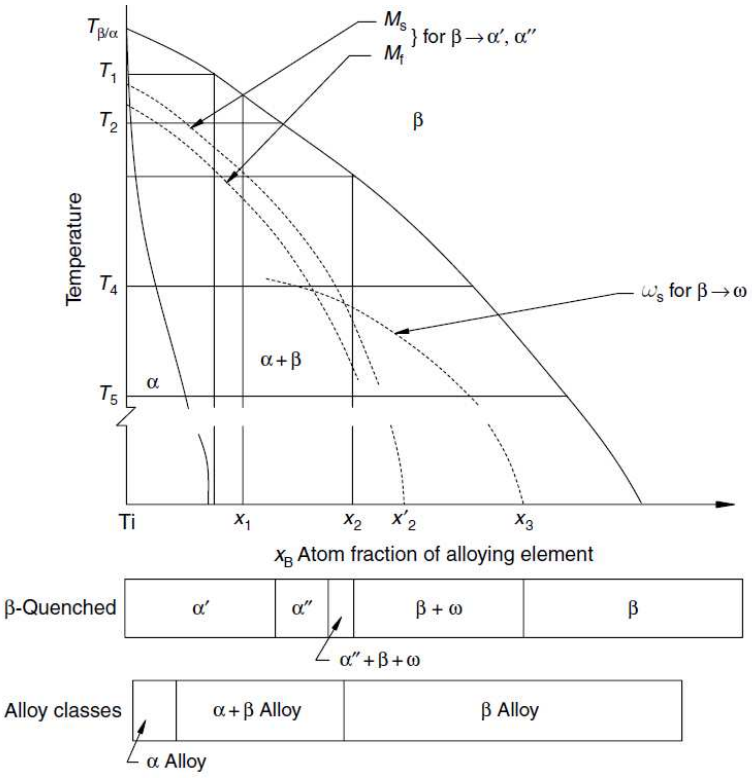

Figure 2.12: Non-equilibrium phase diagram schematic showing structures that form upon rapidly quenching different titanium alloys. [15]

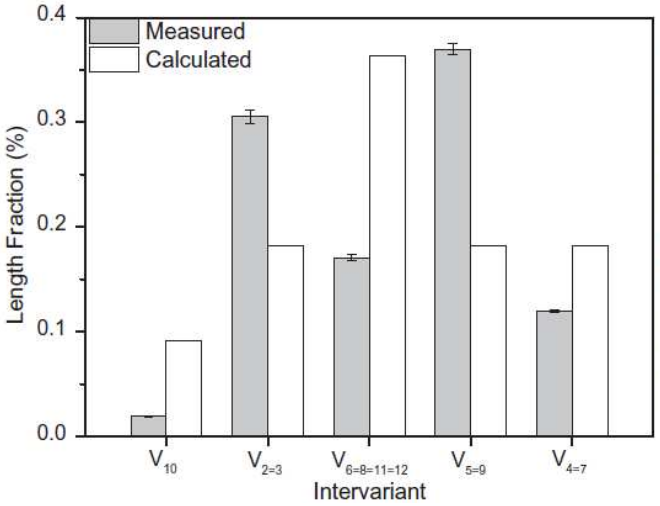

Variant	Rotation angle/axis from V1
V1	–
V2	60°/[1 1 $\bar{2}$ 0]
V3	60°/[1 1 $\bar{2}$ 0]
V4	90°/[1 $\overline{2.38}$ 1.38 0]
V5	63.26°/[$\overline{10}$ 5 5 $\bar{3}$]
V6	60.83°/[$\overline{1.377}$ $\bar{1}$ 2.377 0.359]
V7	90°/[1 $\overline{2.38}$ 1.38 0]
V8	60.83°/[$\overline{1.377}$ $\bar{1}$ 2.377 0.359]
V9	63.26°/[$\overline{10}$ 5 5 $\bar{3}$]
V10	10.53°/[000 1]
V11	60.83°/[$\overline{1.377}$ $\bar{1}$ 2.377 0.359]
V12	60.83°/[$\overline{1.377}$ $\bar{1}$ 2.377 0.359]

Figure 2.13: Measured versus calculated (random) α' variants found in a water quenched Ti-6-4 specimen [16].

2.5 Deformation Mechanisms of Titanium

The HCP structure of the α phase in titanium has slip systems of lower ability to accommodate out of plane deformation than that of cubic systems such as the BCC β phase. This has an influence on the deformation mechanisms and phase transformations that occur. The HCP structure has three types of slip systems; basal, prismatic, and pyramidal. Basal slip occurs with dislocation motion along the basal, or (0001), plane in an <a> type direction. Prismatic slip occurs on the prismatic, or {1010}, plane in the <a> type direction. Pyramidal <c + a> slip occurs along one of the three pyramidal planes in a <11$\bar{2}$3> <11$\bar{2}$0> direction. The relative ratio of the critical resolved shear stress (CRSS) values for HCP slip systems is dependent upon the c/a ratio, which is in turn dependent upon the alloy composition.

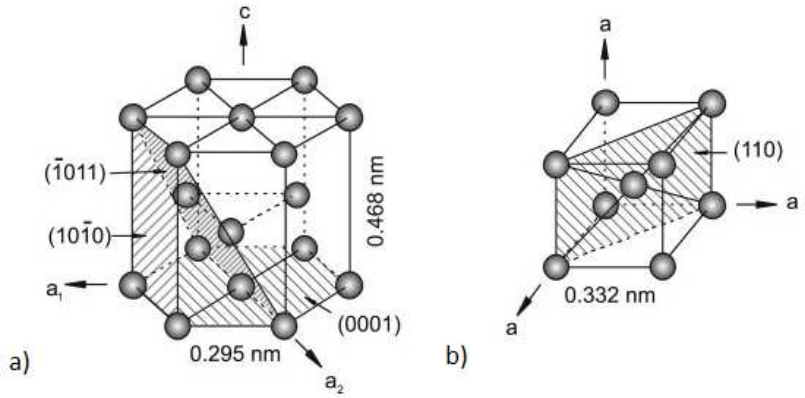

Figure 2.14: a) HCP α crystal structure with basal (0001), prismatic (10$\bar{1}$0), and one pyramidal ($\bar{1}$011) plane highlighted, and b) BCC ß crystal structure with (110) plane highlighted. [2]

Pure titanium has a c/a ratio of 1.587, lower than the ideal ratio of 1.633. This c/a ratio influences the elastic and plastic properties of the material by changing lattice parameters and packing factor of the planes and directions, respectively. Aluminum alloying increases the c/a ratio and decreases the CRSS of basal slip closer to that of prismatic slip [2]. Li et al. [17] compared a collection of experiments and simulations of the CRSS for different slip systems in Ti-6-4; their results showed that basal and prismatic slip had nearly identical CRSS values. Additionally, the aluminum additions found in Ti-6-4 have been shown to suppress twinning. With twinning suppressed, the only other mechanism for deformation that contains a c-axis component is pyramidal slip, which has been shown to have a CRSS several times that of the basal or prismatic slip systems and furthers the anisotropy of the α phase.

The BCC structure in the ß phase has slip systems that can align with the HCP slip systems due to the BOR maintaining relations between close packed planes and directions. The primary slip system for BCC is the {110} $<\bar{1}11>$, with secondary slip planes of {112} and {123}. These numerous slip planes allow for wavy slip formations in conditions that are promoted by the Schmid factor or triaxial stresses that may be created at crack tips [18]. Burger's vectors for the BCC {110}<111> and HCP (0001)$<11\bar{2}0>$ phases, calculated from lattice parameters of a_{HCP}=0.2925 nm, c_{HCP}=0.4670nm and a_{BCC}=0.319 nm [19] in slow cooled Ti-6-4 are $\frac{a}{2}<110>_{BCC} = \frac{\sqrt{3}a}{2}$ = 0.276 nm and $\frac{a}{3}<11\bar{2}0>_{HCP} = b_{HCP}$=0.2925 nm. These differences in Burger's vectors are a possible source for phase boundary strengthening effects by inhibiting dislocation motion. However, the magnitudes are not drastically different. Rotations of slip systems in relation to each other across phase boundaries are an additional source for dislocation impedance. Either forms of the mismatch must be accommodated by residual dislocations at interfaces to fulfill the Burger's vector conservation.

Anisotropic behavior can be expected for moderate to high α content titanium alloys, due to the increased presence of the HCP structure and its particularly limited c + a direction slip (containing a [0001] type component) accommodation due to the high CRSS of pyramidal slip and lack of twinning. This anisotropy is enhanced in the ß processed conditions through three primary mechanisms: 1) large ß grain growth to approximately 500 µm diameter, 2) texturing of the prior ß grains occurring through prior thermomechanical processing, and 3) α variant selection in both the annealed and quenched conditions. A consequence of the colony microstructures is an aligned dual phase structure -in both geometry and crystallographic features- that favors aligned slip systems capable of transmitting dislocations long distances with little impedance. Differences in Burgers vector magnitude, and/or misorientation angles for different slip systems result in residual dislocations at interfaces that increase phase boundary resistance to dislocation propagation.

The α-ß interface presents three opportunities for basal slip transmission, namely, <a1>, <a2>, and <a3> directions of the HCP lattice that, as defined by the specific BOR variant, have increasing misorientation angles between BCC and HCP slip systems. In a perfect BOR, the <a1> direction would lie exactly on $<111>_{BCC}$, but alloying content can shift the angle, as seen in Figure 2.15 for Ti-6242. Note the <a3> direction does not have a close correspondence with a <111> direction that would allow close(st) packed slip transmission through α-ß phase boundaries.

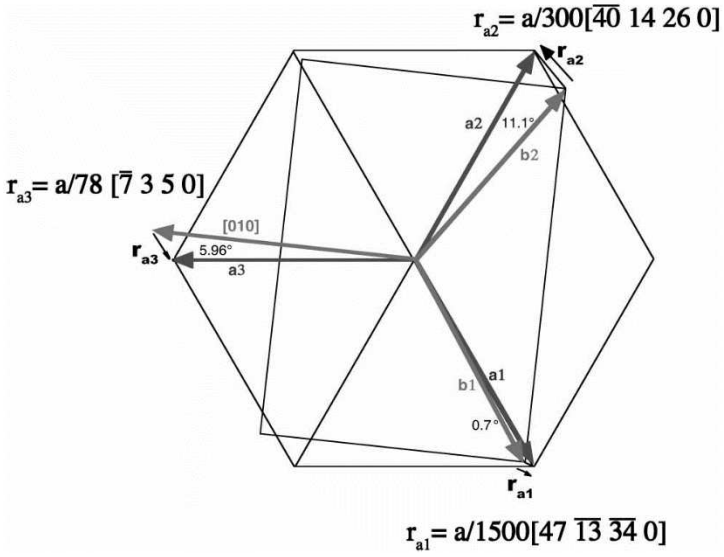

Figure 2.15: BCC:HCP orientation overlay on {110}||(0001) showing <a1>,<a2>,<a3> and their respective residual dislocations formed at phase boundaries [20].

Mechanical testing of carefully grown single colonies [20] confirmed anisotropic behavior based on CRSS, strain hardening exponent (n), and dislocation dynamics. Compression testing of single colony α demonstrated a lower yield strength, as shown in Figure 2.16, and calculated CRSS values for <a1>, <a2>, and <a3> of 330, 405, and 375 MPa, respectively. Additionally, the strain hardening exponents of n1, n2, n3 were 0.034, 0.047 and 0.052 for their respective directions. SEM analysis of polished surfaces revealed planar slip bands across α and ß phases, and their interfaces for the specimen oriented for <a1> slip. TEM observations showed no residual dislocations at phase boundaries for <a1> directions, suggesting that residual dislocations of opposite signs that formed upon entry and exit of the ß phase were able to annihilate.

In contrast to the <a1> specimens, those aligned for <a2> and <a3> basal slip displayed no planar shear bands when viewed in a similar manner (e.g., Figure 2.17). Observations of <a2> dislocation structures via TEM showed large dislocation pileups, as well as cross slip, both within the ß phase. The

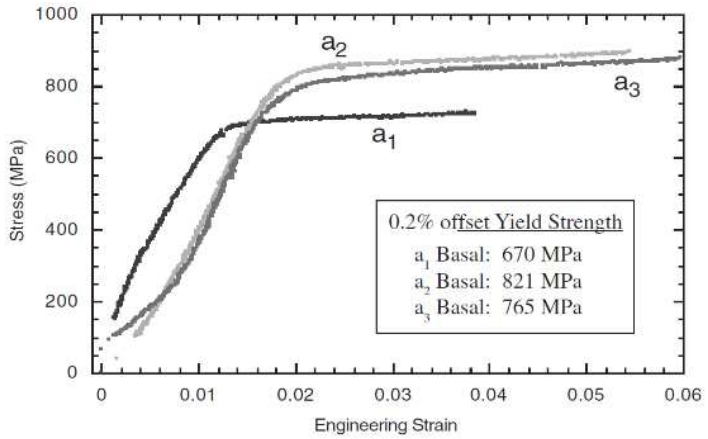

Figure 2.16: Yield strength values for <a1>, <a2> and <a3> directions in HCP α phase determined through compression of selectively grown α colonies in Ti-6242 [20].

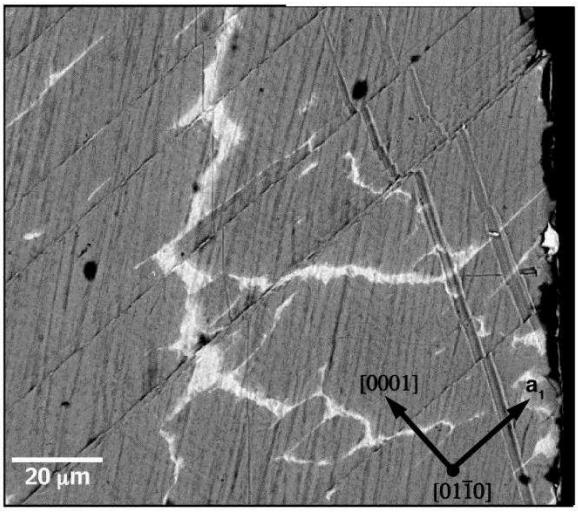

Figure 2.17: Back scatter electron image showing planar basal slip bands occurring in colonies aligned for <a1> slip in Ti-6242. In this micrograph, the lighter grey phase is ß and the darker grey phase is α. Note the shearing of the ß phase and fiducial scratch [20].

increased stress required for the formation of the significantly larger residual dislocation density, due to the larger angle mismatch, causes $(211)_{ß}$ secondary slip that prevents subsequent annihilation of the residual dislocations within the ß phase. Slip planarity across multiple α-ß boundaries is unobserved in <a2> basal slip, due to ß phase strengthening and dislocation interactions that prevent transmission of <a2> basal slip.

Lastly, <a3> basal slip interacted with α-ß phase boundaries in a much different manner. Due to not having a closely aligned $<111>_{ß}$, an alternative sessile dislocation of $\{011\}$ $<100>_{ß}$ is created but dissociates to form two $\frac{a}{2}\{111\}<110>_{ß}$ mobile dislocations. The increased required stress for slip due to

the residual dislocation creation causes pileup within the α phase at the α→ß interface. The two mobile dissociated dislocations within the ß phase form dislocation networks and cause strain hardening. [20]

2.6 Fatigue

Aerospace components are often designed around loading conditions that induce stresses below a conservative value, based upon fatigue curves (S-N plots) that show the cycles to failure (N) for a given maximum applied stress (S). Specimens of various materials, heat treatments and surface conditions are tested in rotating-bending or uniaxial tensile loading conditions. Stress ratios, maximum stresses, loading curves, frequencies, test temperature, and environment are all variables that may influence fatigue life. An example S-N fatigue curve was taken from the widely used Metallic Properties Development and Standardization (MMPDS) data set, formerly MIL-HDBK-5 [21], as shown in Figure 2.18. Note the increased scatter with increasing fatigue life, due to an increasing dependence on fatigue crack initiation at pre-existing defects, the presence of which depends on manufacturing conditions.

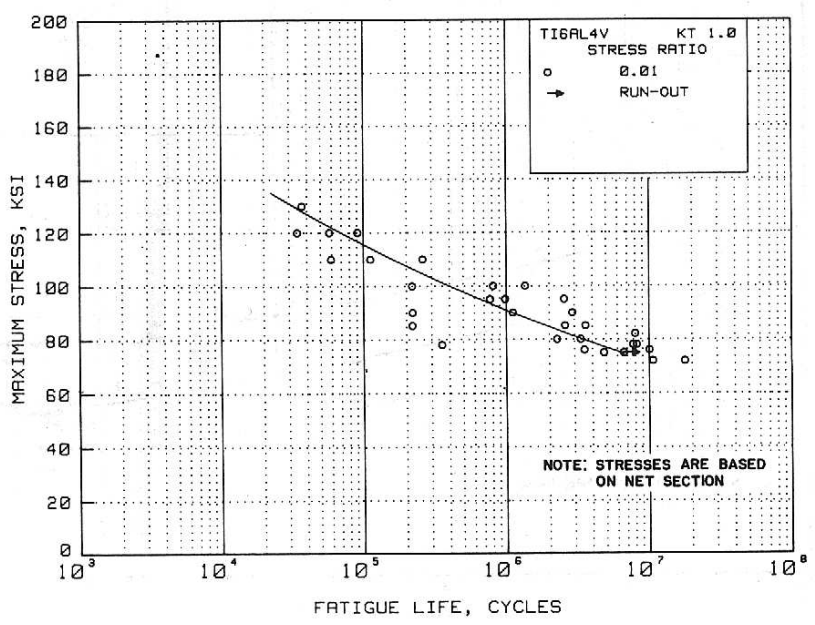

Figure 2.18: Smooth tensile fatigue testing of Ti-6Al-4V [21].

An alternative method of characterizing a material's resistance to fatigue is to perform Fatigue Crack Growth Rate (FCGR) measurements. This method utilizes the concepts of linear elastic fracture mechanics (LEFM) and the stress intensity (K) of a crack with a known length, geometry and applied stress. With the knowledge of an existing flaw in a component, the user can estimate the remaining life

before failure or unacceptable performance, based upon an integration of the crack growth curve. The initiation, propagation, and unstable growth stages (1, 2 and 3, respectively) occur as a result of increasing stress intensity during crack growth, as shown schematically in Figure 2.19. Note the variable of importance is K_{max}-K_{min}=ΔK, providing the cyclic work to initiate and propagate the crack.

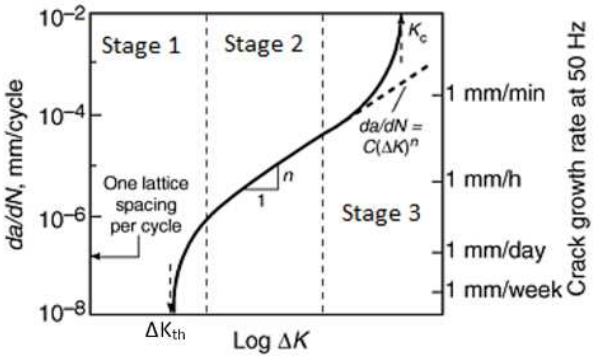

Figure 2.19: Fatigue crack growth rate plot with multiple stages of crack propagation [22].

The typical specimen geometry of a compact tension specimen with a notch for crack initiation in a controlled location is shown in Figure 2.20. Geometry factors for different crack geometries have been determined through experimental and modeling approaches and are available in databases. Assumptions made during the LEFM basis for stress intensity calculations limit applicability of the relation. Note that superposition of crack length and applied stress allow the user to determine growth rates for a desired combination of crack length and applied stress. This superposition, or similitude, breaks down for short crack lengths, due to anisotropic interactions of the cyclic plastic zone size with the microstructure and reduction in crack closure mechanisms. Such effects prevent application of traditional specimen geometry results to the initiation stage of cracking at or below the K_{th} stress intensity values [22]. The stress intensity calculation for mode 1 (tensile) loading conditions, given by Equation (2.1, utilizes the current applied stress σ, geometry factor Y, and crack length a [22].

$$K_I = \sigma \bullet Y \sqrt{\pi a} \tag{2.1}$$

A crack can be thought of as a high stress concentrator that forms a local plastic zone just ahead of the crack tip. First approximations based upon Irwin's calculations [24] can be used to calculate the radius (ry) of the plastic zone at the tip of a crack; Equation (2.2 applies for plane stress conditions of relatively thin specimens. The σys in the equation is the yield stress of the material that the crack is propagating through.

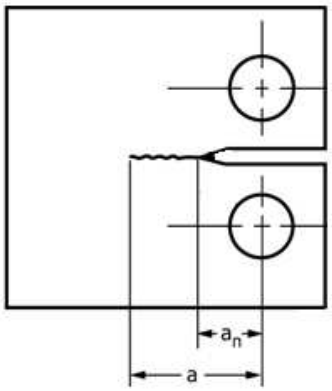

Figure 2.20: Compact tension specimen, commonly utilized for fatigue crack growth rate measurements [23].

$$r_y = \frac{1}{2\pi}\frac{K^2}{\sigma_{ys}^2} \tag{2.2}$$

For parts whose thickness imposes a triaxial tensile stress state based upon material constraint, plane strain conditions reduce this radius of plasticity by a factor of 3 [24]. Perhaps counterintuitively, the decreased plastic zone size associated with the plane strain condition is undesirable from an engineer's perspective as this decreases the energy absorption capabilities of the material by reducing the volume of interaction (ie; the work to propagate the crack).

The interactions of the plastic zone with the material transition from microstructurally-sensitive Stage 1 crack growth to a microstructurally-insensitive Stage 2 crack growth when the plastic zone size surpasses the controlling microstructural unit (CMU) size. Maintaining multiple CMU's within the plastic zone allows for isotropic strain accommodation; below this plastic zone size, the anisotropic nature of the material's slip systems become particularly influential. This CMU is often on the order of the grain size of the material; however, titanium alloys with different heat treatments have been shown to have different features tied to the CMU. The ß-annealed microstructures have been shown to have the CMU correlated to the α colony size, as seen in Figure 2.21. Distinction between variants of α colonies that do and do not share common basal planes was not taken into account by Yoder et al. [25].

Interestingly, the crack length has been shown to have a secondary effect in addition to the stress intensity factor. Shademan et al. [26] utilized notched specimens to initiate a crack with subsequent notch removal. This geometry emulates the growth of a fatigue-initiated crack and permits monitoring of

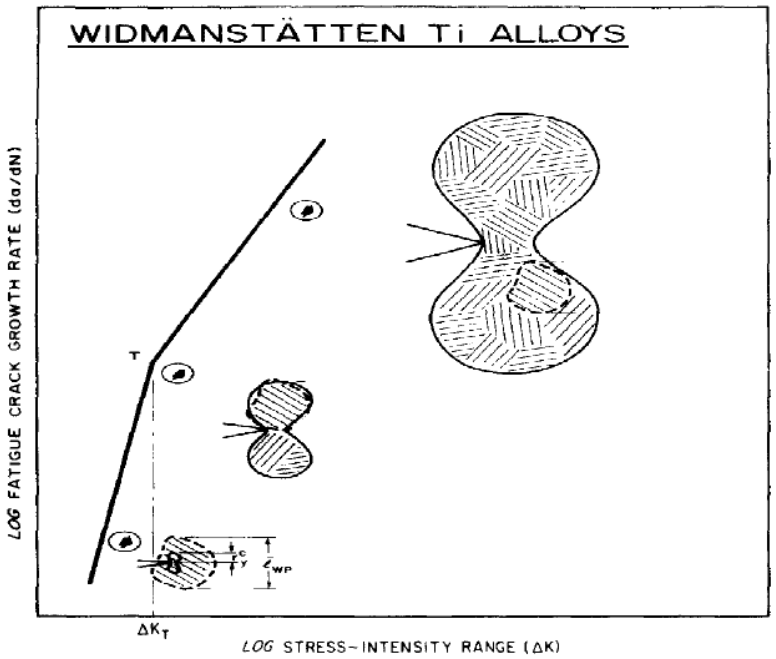

Figure 2.21: Effects of cyclic plastic zone and colony packets on fatigue crack growth rates [25].

localized crack growth. Comparisons between short and long starting crack lengths utilized for fatigue crack growth rate testing displayed a significant difference in growth rates below the reported ΔK_{th}, as shown in Figure 2.22. Through removal of the notch and most of the starter crack (created prior to monitoring growth rates), toughening mechanisms that develop in longer crack lengths, such as crack wake plasticity-induced closure and roughness-induced crack closure, are not yet present. This demonstrates the limitations of the compact tension specimen (Figure 2.20) for representing the initiation stages of crack growth.

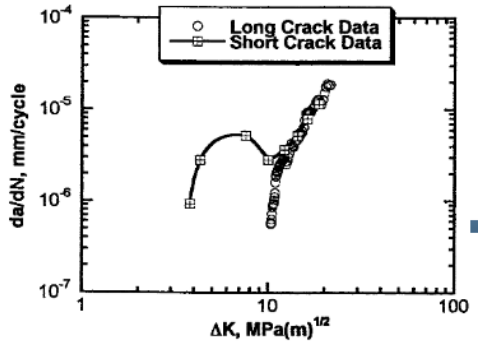

Figure 2.22: Comparison of fatigue crack growth rates for short and long crack starting lengths [26].

2.7 Facet Features – Low Stress Intensity Crack Growth

Faceted features on fracture surfaces of titanium alloys have been observed for quite some time; Eylon demonstrated their presence in 1976 while evaluating mechanical properties of an α + ß titanium alloy in the ß-annealed condition [27]. Their appearance is similar to that of a brittle cleavage facet, showing a flat, fanning out feathered surface as seen in Figure 2.23. While displaying similar features that suggest a relation to the crystallographic planes of the material, these are present in regions of fatigue crack initiation instead of fast fracture. These facets are indicative of microstructurally sensitive crack growth occurring at short crack lengths observed to occur when the plastic zone size is on the order of the α colony size [28].

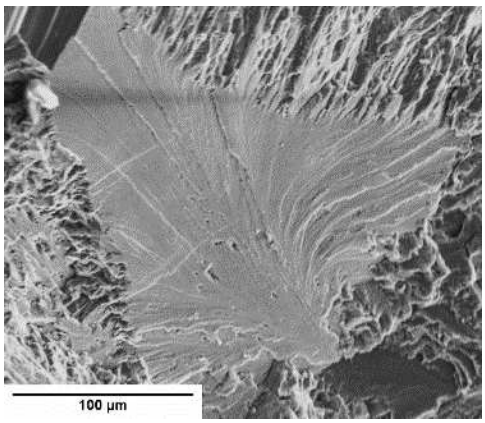

Figure 2.23: Fatigue facet feature on a Ti-6-4 fracture surface. Primary loading direction was in and out of plane, with crack propagation direction upwards.

After their discovery, there is little literature concerning the characterization of facets in titanium alloys until reports of fracture surfaces of Ti-6-4 turbine compressor blades and discs that displayed higher than normal crack initiation and growth rates [29]. These facet features have been observed for a multitude of different environmental and loading conditions. However, most notable for use in turbine engines is dwell fatigue, a cyclic loading containing a hold at the peak load for a period of time. A degradation in fatigue life exceeding an order of magnitude has been reported, due to localized planar slip within equiaxed α grains over long length scales. These regions of faceted fracture occur in microtextured regions, as a result of the forging operation.

Providing a detailed relationship between the mesoscopic facet plane, α phase basal plane, and loading direction orientation was recently addressed by Pilchak et al. [30][31]. Quantitative tilt fractography was used to provide the angular differences between the three features. This research has shown the orientation of the facet plane to be either on or near the basal plane of the α phase [32][33][30], with consistent variations in angle corresponding to different loading conditions, i.e., cyclic fatigue, dwell

fatigue, sustained load and environments, i.e., atmospheric air or aqueous 3.5% NaCl. Facet features formed through continuous cycling in air were found to be oriented on the basal plane for crack initiation facets, within 5° of the basal plane for propagation facets [34]. Facet features formed during SCC testing frequently were oriented ~15° off of the basal plane [35][31][34][36], despite the resolved shear stress often permitting easy slip on the basal plane. Dwell fatigue testing resulted in initiation facets oriented within 1° of the basal plane, and dwell fatigue propagation facets inclined 16° to 22° off of the basal plane. The fracture surfaces of sustained load, stress corrosion cracking (SCC), and dwell fatigue specimens showed microscopic tear ridges extending in the direction of crack propagation [34], akin to what is observed on the faceted features presented later in this thesis.

Another important factor is the angle of the facet normal in relation to the loading axis during the uniaxial tensile testing. Dwell fatigue testing resulted in facet features oriented perpendicular to the loading axis, indicating a Mode I stress state. Stroh's model was proposed to explain how slip was occurring on a near-basal plane oriented perpendicular to the loading axis by Evans and Bache [37]. This involves two neighboring grains with different orientations. One grain (termed the "soft grain") is inclined to the loading axis and the shear load generates slip dislocations that pile up on the grain boundary with the neighboring grain (termed the "hard grain"). This dislocation pileup induces sufficient shear stress to induce slip along the basal plane perpendicular to the loading axis within the "hard grain". However, further investigation of dwell fatigue performed by Pilchak [34] showed that the Stroh model did not explain the slip on the irrational *{hkil}* plane near {1 0 -1 7}, nor the time dependent nature of dwell fatigue. However, this fracture plane could be explained by hydride formation.

The presence of hydrogen has been proposed to influence facet formation and has been shown to have an increasingly deleterious effect on the fatigue life, notably in dwell fatigue conditions [29][34], while still below the material specification limit and observed hydride formation levels. Hydrogen's rapid diffusion and attraction to the triaxial stress state at a crack tip has been theorized to explain the time-dependent component of dwell fatigue [38]. Additionally, the mesoscopic plane of the facet features found at moderate hydrogen levels and/or dwell fatigue specimens has been characterized as lying on a known habit plane of the previously mentioned titanium hydride near {1 0 -1 7}, 15° off of the basal plane [34].

2.8 Project Background

This industry-driven project was initiated because of the failure of a hydraulic damper unit, and evolved into a study aimed at determining the sensitivity of microstructure and fatigue life to variations in cooling from above the ß-transus. The hydraulic damper units dissipate mechanical energy into heat by

the piston forcing hydraulic fluid through metered ports. The specific strength, corrosion resistance, and operating temperature requirements made titanium alloys a better alternative to aluminum alloys and steels.

The hydraulic damper, shown in Figure 2.24, can be described as operating in a relatively benign environment for titanium alloys. Operating temperatures were maintained at roughly 130 °C in an atmospheric environment. The internal diameter of the bore was electroplated with a cobalt phosphorous coating to provide a wear resistant surface for the mating bronze wear ring on the piston. Cyclic internal pressurization of the unit was provided by hydraulic fluid (MIL-PRF-83282, known to be compatible with titanium alloys) at a frequency of 3 Hz. This generated biaxial stresses nominally associated with a thin walled pressure vessel of 125MPa and 250MPa in the axial and circumferential (hoop) directions, respectively. This testing was part of a multiphase development and qualification testing of the hydraulic unit prior to flight testing. While over-conservative and accelerated, the initial testing produced a fatigue failure via through-wall-thickness crack propagation prior to the minimum desired life (quantified in operational cycles). Design stresses were based upon internally developed S-N fatigue curves with a statistically based margin of safety applied. In addition to margins of safety, a "knockdown factor" was applied to reduce the design stresses based upon prior experience with hard, wear-resistant coatings that have shown a reduction in fatigue life, due to local stress concentrations at regions of the fractured coating. These coating fractures occur as a result of residual stress buildup during processing, contact-bearing loads, or loading of the substrate that exceeds the strain capability of the coating. The combination of premature fatigue failure, possible environmental contributions, and fatigue crack morphology lead preliminary failure investigations towards the testing environment, plating operation, and heat treatment of the substrate titanium material.

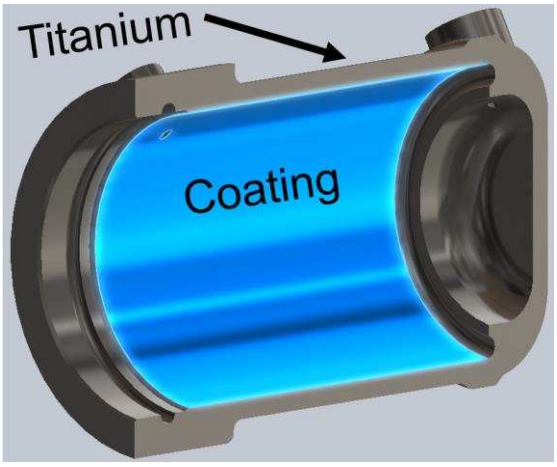

Figure 2.24: Cross section schematic of the hydraulic damper showing the cobalt-phosphorus coating on the inner diameter of the Ti-6-4 housing.

CHAPTER 3: METHODS

3.1 Initial Investigation

Analysis of the hydraulic damper units was conducted after premature failure occurred during representative testing. Failure of the unit was detected by abnormal fluid pressure measurements during testing and hydraulic fluid outside of the actuator. The actuator was then disassembled for initial non-destructive evaluation (NDE) that included fluid penetrant inspection (FPI) and optical imaging. The actuator housing, including the cobalt-phosphorous (Co-P) coated titanium, was sectioned using wire electronic discharge machining (EDM) for further analysis. Fully propagated cracks were sectioned in a manner to harvest the fracture surface; partially propagated cracks were sectioned for metallographic analysis. Imaging of the fracture surfaces and metallographic samples was performed with various scanning electron microscopes (SEM), utilizing backscattered electron (BSE) and secondary electron (SE) imaging. Two separate failed hydraulic damper units were prepared and analyzed in this manner.

3.2 Hydrogen Testing

Regions of a failed hydraulic damper unit were sectioned and prepared for hydrogen content measurements with low temperature sectioning methods. The nearly amorphous Co-P coating was removed with low temperature abrasive grinding. Thickness measurements were made during this process and X-ray diffraction (XRD) was used to confirm that the titanium substrate was exposed. Further sectioning of the material into multiple pieces was performed to investigate any possible hydrogen absorption due to the Co-P electroplating process as a function of depth. A separate set of specimens was prepared to analyze each step of the Co-P electroplating process, including pre-plating etching, plating, and chemical stripping. The chemical stripping was included, due to re-plating requirements of the units because of inconsistent adherence or thickness, which was experienced with processing the units.

Hydrogen content measurements of the material were performed with a LECO RH-404 instrument per ASTM E1447. Calibration of the RH-404 was conducted with certified titanium samples with known quantities of hydrogen (42 wppm) to ensure accurate measurements. Tin additions (1 g) were used during calibration and testing to assist in full melting of the sample material during testing. The mass of the final measurement sample was 0.2 g, which is smaller than steel specimens due to higher expected hydrogen content of titanium alloys.

3.3 Corrosion & Environmental Effect Testing

Sustained load testing was performed on threaded dog-bone cylindrical specimens to investigate any corrosive environmental effects of the plating process. Specimens were processed to evaluate effects of shot peening, electrodeposition of the coating, and heat treating of the coating. The loading schedule utilized an incremental, stepwise increase in load to compare time-until-failure for each sample set. Post-mortem fractography of the specimen fracture surfaces was performed by SEM to qualitatively detail the types of fractures induced during testing.

Attempts to measure the presence of corrosive agents were performed by means of two additional tests. The first utilized an electron dispersive spectroscopy (EDS) detector in an SEM. Various accelerating voltages were used to generate EDS spectra of features on metallographic samples and fracture surfaces in an attempt to find indications of chloride-induced corrosion. Due to concerns of environmental effects from possible halogen contamination of the hydraulic fluid, compositional analysis of the halogen content in the hydraulic fluid was measured by a third party. EPA Method 9076 was used, in which the hydraulic oil specimen from the hydraulic damper unit was combusted, and an inert carrier gas carried the halogens to be measured quantitatively by microcoulometry. This test method does not allow distinction between the type of halogen; instead, it only returns a total halogen content that must be combined with knowledge of the sample's previous processing and operating environment. Chlorine is the primary halogen measured; bromine and iodine are underrepresented by approximately two fold, and fluorine is not detected.

3.4 Water Quench Testing

Quench delay testing was performed on Ti-6-4 round stock material that started out in a MA condition per AMS 4928, as with all other Ti-6-4 material used in this project. Quartz encapsulation was performed with three cycles of rough vacuum pumping and 99.995% pure argon purging, and final sealing with an oxyhydrogen torch under a vacuum to prevent internal air pressures from breaching the tube during heat treatments. An atmospheric furnace was equilibrated at temperature for a minimum of 2 hours prior to placing the quartz encapsulated Ti-6-4 in an atmospheric furnace for 30 minutes at 1050 °C, safely above the ß-transus temperature of 985°C. Encapsulated samples were removed from the furnace and set on insulating fire bricks for the specified amount of time after the furnace door was opened. Once the specified amount of time was reached, the quartz capsules were crushed and water quenched.

Larger samples were water quenched and had an Omega K-type thermocouple (P/N: TJ36-CAXL-18U-18-SMPW-M) embedded in a 0.125" diameter hole in the 2.625" diameter by 2.630" length bar of Ti-6-4. A small layer of thermally-conductive, alumina-based high temperature adhesive was used to keep the thermocouple in place during transfer and quenching operations. The thermocouple tip was located at half the radius and half the height of the large sample. Atmospheric furnaces were used with large steel hearths as thermal mass to maintain the furnace temperature (1050 °C) as the room temperature Ti-6-4 sample was placed inside. Samples were kept in the furnace until thermocouple readings reached 1030 °C, and then rapidly water quenched while vigorously swirling the sample in the bath. Temperature versus time data collected from this experiment in conjunction with computer modeling were used for determining the quench rates.

Finite element analysis (FEA) with the ANSYS Workbench software and models imported from Solidworks was used to predict the quenching behavior. Physical material properties were imported from the database, including: density, heat capacity, thermal conductivity, and emissivity. Inputs into the FEA software included material starting temperature, surrounding media temperature, convective cooling coefficient, thermocouple location, and analytical step size. FEA with these thermal models was used to determine convective cooling coefficients by iterative curve fitting of model outputs to the large sample water quenching data. The convective cooling coefficient, a value that is related to the material surface and surrounding media properties, was then applied for retrospective FEA of water quench cooling rates of the hydraulic damper unit forging.

3.5 Dilatometry

A TA Instruments model DIL 805L quenching dilatometer was used to determine the effects of cooling rate and transformation temperature on the resulting Ti-6-4 microstructures. The dilatometer uses a high frequency (250 kHz) induction heating coil that surrounds the sample held in place with quartz rods at each end. Type S thermocouple wires were spot welded on the outer diameter surface with a DCC HotSpot I thermocouple welder at 12 volts for temperature in-situ measurements and accurate temperature control. Specimens were procured from round bar stock turned on a lathe to 4 mm diameter, and then abrasively cut to 9 mm in length to create cylinders.

Prior to heating, the dilatometer chamber was pumped down to approximately 10^{-4} torr to prevent oxidation of the material. Samples were heated from room temperature (23 °C) to 1050 °C at 8 °C/s. To fully dissolve the equiaxed "primary" α into β and obtain a representative β grain size of approximately 300 to 500 µm, samples were held at the solutionizing temperature of 1050 °C for 15 minutes prior to any subsequent cooling step. Cooling was performed an an argon gas quench supplied through internal ports

along the length of the induction coil. Thermal profiles were preprogrammed using the instrument's software. Multiple tests were performed to tune the induction coil and gas valve proportional-integral-derivative (PID) controller to maintain proper temperature control. Unstable over correction occurs without proper PID tuning at intermediate to high cooling rates, which may be avoided only by closely monitoring the induction coil and gas valve parameters. Transformation temperature interpretations were based upon deviations in slope on the change in length data during cooling operations.

3.6 Crystallographic Analysis of Fracture Surfaces

Metallographic samples sectioned from the hydraulic damper units were cold mounted in a two-part epoxy resin and ground with silicon carbide grinding paper to a 1200 grit finish before 6 µm, 3 µm, and 1 µm diamond polishing. Final sample preparation was performed using 0.05 µm colloidal silica on a vibratory polisher for 8 hours. The mounted samples were observed by light optical microscopy (LOM) to locate regions of fractured coating and titanium substrate crack propagation. Linear regions of the crack paths were identified using a FEI Quanta 600i Environmental SEM to select regions of interest for further crystallographic analysis. Crystallographic analysis was performed using an FEI Helios Nanolab 600i equipped with a field emission source, gallium focused ion beam (FIB), platinum deposition system, EDAX energy dispersive spectroscopy (EDS) system, EDAX electron back scatter diffraction (EBSD) detector, and Omniprobe nano-manipulator.

EBSD scans of linear crack path regions were obtained to characterize the α-phase (HCP) 3-D orientation. It should be noted that these regions were near prior ß grain boundaries and were partially or fully within a large α colony. Orientation Imaging Microscopy (OIM) data analysis software was used to compare the in-plane angle of the α colony basal plane trace formed when intersecting the metallographic sample surface with the in-plane orientation of the crack path (or facet trace from the fracture surface) of the metallographic sample surface. The FIB capability of the FEI Helios SEM was then used to remove a wedge of material in the linear crack region at a perpendicular angle to reveal the second trace of the facet features. The second trace of the facet feature was measured using ImageJ to account for the viewing angle. These two sets of traces were used to determine the offset angle of the facet plane relative to the α phase basal plane.

3.7 Rotating Bending Fatigue Testing

Smooth specimen, rotating bending fatigue (RBF) testing was performed using an RBF-200 machine. This equipment uses a variable speed electric motor that can rotate at 500 to 10,000 RPM; this test utilized 4,800 RPM. The motor spindle has a blind end collet that is tightened to the spindle with a

nut. The loading arm has an identical collet attachment for the other end of the specimen. The loading arm has a pivot point on one end and an applied weight that moves along the arm up to a maximum of 22.6 N*m bending moment that is transferred through the sample. After loading the specimen into the motor end collet, the free end of the specimen was measured and adjusted as required to maintain a runout less than 75 µm.

Each full rotation of the sample during operation puts the smallest diameter of the specimen into a sinusoidal tensile-compressive stress state. Due to the long moment arm and high efficiency bearings, shear and torsional stresses, respectively, were determined to be negligible and thus ignored. A steel specimen with strain gauges attached to the gauge section was utilized to confirm the applied stress for a given bending moment by calculations from the output strain and known elastic modulus. The measured strain values were found to have less than 3% error compared to those calculated. Calculations for maximum equal and opposite tensile and compressive stresses were based upon the bending beam equation:

$$\sigma_{Max} = \frac{32 \bullet Moment}{\pi \bullet Diameter^3} \tag{3.1}$$

Specimens were heat treated using quartz encapsulation as described previously to produce microstructures representing quench delay (QD) and minimal-QD material. The representative quench delay (QD) specimen was held inside the quartz capsule for approximately 90 seconds on a room temperature steel hearth outside the furnace before quenching to produce a similar microstructure to the hydraulic damper units. It should be noted that the quartz tube decreased the cooling rate by preventing convective cooling and acting as a heat shield. The minimal quench delay (QD) specimens were removed from the quartz capsule and water quenched within 5 seconds of removal from the furnace. The first specimens were machined and then heat treated to reduce damage caused by the machining process. However, water quenching and subsequent aging resulted in distortions that created extraordinary scatter in the fatigue data. The second batch of specimens (of both microstructures) were machined after completing the heat treatments. The specimen geometry included a constant radius taper with a gauge diameter of 4.89 mm at the smallest region. Gripping diameters on both sides were 9.525 mm to fit the appropriate collets.

3.8 Fatigue Crack Growth Rate Testing

Fatigue crack growth rate (FCGR) testing was performed using uniaxial tensile loading with electrical potential difference (EPD) measurements, as discussed in ASTM E647-15 section A6 for in-situ crack length data. The specimen geometry was selected for short crack length measurements with a small

notch, as opposed to the typical compact tension specimens often used when testing per ASTM E647. Fatigue testing was performed under load control settings, with a sinusoidal wave function that was tuned using PID controller adjustments under a forced square wave at 10% of the actual loads to match measured load to command load. These PID controller value adjustments were performed on a geometrically representative dummy specimen prior to utilizing the calibration specimen.

The load frame setup used was an MTS servohydraulic unit with MTS 647 hydraulic wedge grips for holding the specimen and a 10 metric ton MTS 661.21A-02 load cell for data aqcuisition. Hydraulic power was supplied through an MTS Model 505.30 SilentFlo Hydraulic Power Unit capable of 20 MPa and 110 liters per minute. The hydraulic system and load frame were controlled with an MTS TestStar IIs controller unit and software. A frequency of 20 Hz was chosen such that no strain rate effects would be present (nominally under 50 Hz [39]). The servohydraulic system was able to maintain desired loading, without excessive noise or deviations, while still producing results in an acceptable time period.

The specimens were produced from bar stock and milled to rough dimensions prior to heat treatment. Specimens were vacuum quartz encapsulated prior to both the ß solution heat treatment at 1050°C, and aging. The “minimal QD” specimens were water quenched from the ß phase field within 5 seconds after the furnace door was opened and the “representative QD” specimens were quenched 90 seconds after removal from the furnace. The “representative QD” specimens remaining in the sealed quartz tube (to prevent oxidation) had a large effect on the time required to create the representative microstructure, as the quartz tube produced an emissive thermal shielding effect and reduced direct convective cooling. After aging, the specimens were final machined to remove distortions and a notch was wire electric discharge machined (EDM). Notch geometry was chosen to be a short and sharp to maintain stress intensity similitude during short crack growth, and to ensure that the critical crack initiated at this region. The EDM wire was 0.25 mm diameter, producing a notch of 0.43 mm in maximum depth with a width of 0.30 mm. Electrodes for transmitting the current, provided by the Keithley 6220 power supply, consisted of 14-gauge copper wire attached in the grip sections by tungsten inert gas (TIG) welding (60mm away from the gauge section) with an argon shield gas. A cyanoacrylate glue was then applied as a strain relief to maintain joint stiffness and prevent separation during handling and testing. Voltage wire electrodes (22-gauge nickel wire) were applied with a thermocouple spot welder on both sides of the wire EDM notch. Cyanoacrylate glue was also applied on the voltage wire electrode junctions.

The forces applied by the hydraulic frame were selected such that the fatigue crack would initiate in the notch at a low stress intensity and short crack length. Stress intensity calculations were based upon specimen geometry, applied load and crack length. The geometry factor, specific to the specimen type and loading conditions, was used in the stress intensity calculation and is valid for a crack length to specimen

width ratio of 0.6. Under the loading conditions, the specimen reached the critical stress intensity and fractured while the geometry factor (Figure 3.1) was still within the valid crack length to specimen width ratio.

Crack growth measurements involved the pulsed marker cycles and electric potential difference (EPD) methods that allowed for retroactive recreation of the crack growth rate at known crack lengths, which correspond to stress intensities for a constant load. Pulsed marker cycles of 10 cycles at an increased stress ratio of R=0.9 every 100 regular cycles were used on the calibration specimen to correlate measured voltage and crack length. This was not used for the actual tests, in an effort to remove potential room temperature dwell fatigue effects from the testing. An accurate current source is required for this method to reduce noise and obtain meaningful data at low crack lengths. The Keithley 6220 fulfilled these requirements. A calibrated unit was supplied by the manufacturer as a demonstration unit for the duration of the test. Voltage measurements across the crack growth region were performed with a Keithley 2182A nano-volt digital multi-meter (DMM). The DMM and current source were connected and utilized in the "delta" mode that alternated the electric current signal, then calculated half of the difference between voltage readings. Because thermoelectric/EMF voltages produced by the thermocouple/Seebeck effect are biased in one direction and not current dependent, this delta mode allows for elimination of this systematic noise to produce higher fidelity data. This method is mentioned in section A6.11.3.2 of ASTM E647-15. The use of a reference specimen, as discussed in section A6.3.4 of ASTM E647-15, was attempted, but resulted in significant noise due to the thermoelectric effects of the Cu-Pb/Sn, Pb/Sn-Ni, and Ni-Ti junctions, making the method unusable.

Automated data acquisition from the Keithley units was not possible with available equipment. Instead, voltage measurements were recorded with a GoPro camera taking an image every two seconds with a digital clock in the frame to record start, stop, and interval times.

Data analysis required multiple processing steps to achieve final crack growth rates. Voltage outputs included noise effects from elastic shape change (elongation and Poisson effect) that were reduced utilizing a two-term exponential parametric curve fitting in MatLab for the short crack growth region. Curve divergence at higher crack lengths limited Stage III crack growth analysis. With known start and finish voltages and crack lengths, a correlation between voltage and crack ratios was calculated. With crack length information as a function of cycle count, the remaining variable to calculate is stress intensity. Stress intensity calculations were performed knowing the applied load, remaining cross sectional area, and geometric factor as a function of crack length to width ratio, as seen in Figure 3.1. Crack growth rates as a function of stress intensity were then calculated from these known variables.

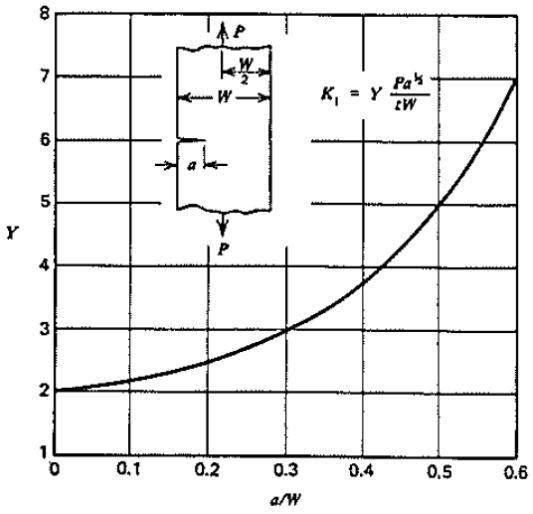

Figure 3.1: Geometry factor for single edge crack growth. K_I is the effective stress intensity, Y is the geometry factor determined by instantaneous crack length, P is the applied load, a is the crack length, t is the specimen thickness, and W is the specimen width [24].

3.9 Tensile and Hardness Testing

Quasistatic tensile testing was performed on one rotating-bending-fatigue specimen of each heat treatment condition (minimal and representative QD) to compare the ultimate tensile strengths. Tensile testing was performed in the same MTS servohydraulic frame as the fatigue crack growth rate testing with wedge grips to accommodate the circular cross section of the specimen. Displacement control was used in lieu of load control to maintain quasistatic conditions during plastic deformation.

Hardness testing utilized a Wilson Tukon Series 200 micro-Vickers indenter with parameters of 10 second dwell time and 500 gram force indentation load. Twenty indentations were performed on each specimen to obtain statistical significance. Indentations were taken on a grid near the center of the cross sectional area of the specimens for the minimal and representative QD heat treatments.

CHAPTER 4: RESULTS

4.1 Initial Investigation

Failure of the hydraulic dampers were discovered by internal pressure loss and subsequent observations of through-wall thickness crack propagation. These cracks were observed on several units not associated with any geometric features, and appeared random. After disassembly of the hydraulic actuator assemblies, NDE inspection by dye penetrant showed axial fracture of the wear resistant coating inside the bore that interfaces with the piston contact surface. Imaging of polished sections from the hydraulic actuator revealed a fractured coating with subsequent crack propagation into the substrate material as shown in Figure 4.1.

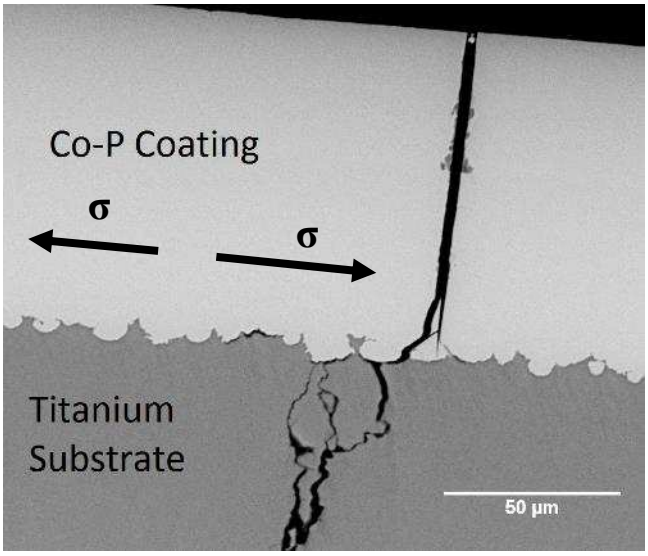

Figure 4.1: Crack propagating downward through the coating-substrate interface of the hydraulic damper in the piston side internal bore. Note the primary direction of applied stress in both the coating and titanium substrate.

The branched and tortuous crack path in the titanium substrate in Figure 4.1 typically indicates either corrosion fatigue or possible hydrogen contributions. Third party SEM/EDS analysis of a hydraulic unit that failed during fatigue testing revealed a localized region of sub-surface chlorine contamination within the titanium material (Figure 4.2). Further attempts to observe chlorine were unsuccessful; it is suspected that sample contamination during preparation was the cause.

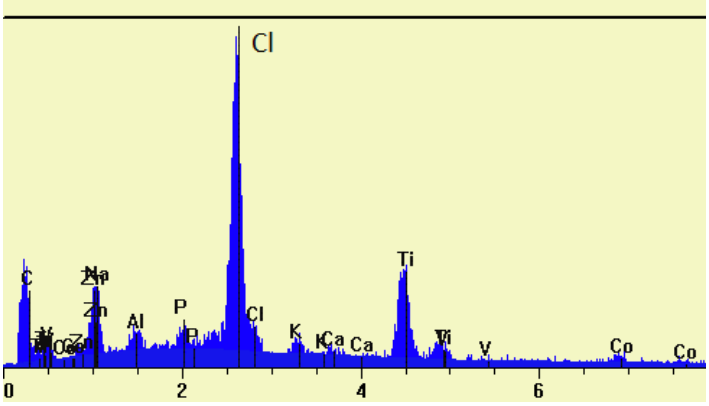

Figure 4.2: EDS results from subsurface tortuous cracking showing the presence of chlorine.

Sustained load testing with incrementally increasing loads was conducted and compared with the bare substrate material, or coupon set 1, with a cobalt phosphorous electroplated material, or coupon set 2. Results shown in Table 4.1 displayed significant scatter in each coupon set, and no conclusion could be made regarding the influence of the cobalt phosphorous electroplating process on stress corrosion cracking. The fracture surfaces of both sample sets revealed dimpled, ductile fracture occurring at prior ß grain boundaries (e.g. Figure 4.3), indicative of overload failure without environmental contributions. Note the red numbers in Table 4.1 indicate the stress and time at which failure occurred.

Table 4.1: Sustained load testing results

Applied Stress		*97.5% YTS*	*+27 MPa*	*+13 MPa*	*+13 MPa*	*+13 MPa*	*+13 MPa*
		1068 MPa	*1096 MPa*	*1110 MPa*	*1123 MPa*	*1137 MPa*	*1151 MPa*
Coupon Set	*Coupon Number*	*Time Survived at Stress [Hours]*					
1	*32*	*288*	*48*	*18.4*			
	33	*288*	*25*				
	34	*170.9*					
2	*28*	*300*	*48*	*48*	*50.7*	*48*	*56.8*
	29	*300*	*25.2*				
	30	*277*					

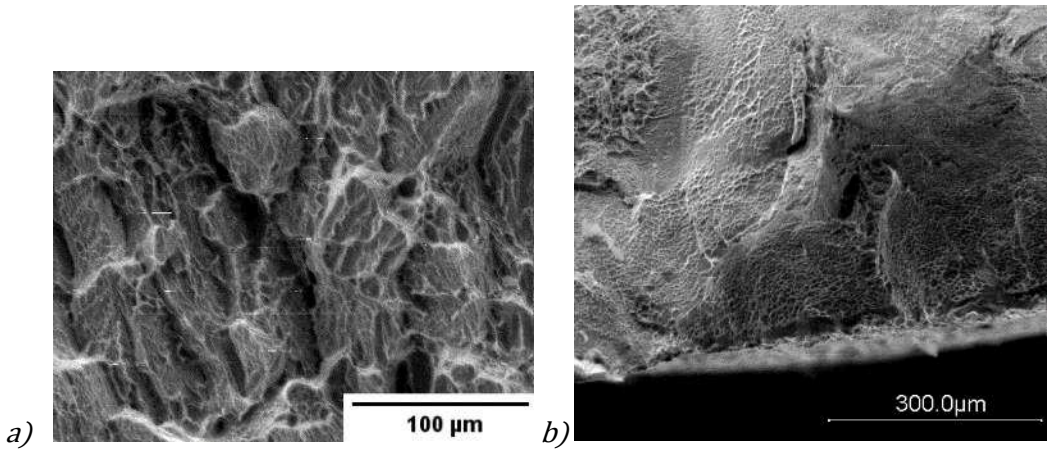

Figure 4.3: Typical fracture surfaces (a) near the central region and (b) near the circumference of sustained load specimens of either processing condition. Tensile loading direction is into and out of the plane.

The internal hydrogen content was previously measured from the same unit used for this work and was found to be 46 wppm, or well within the allowable limits. This prior testing did not specify the hydrogen content sampling location on the unit, so any localization of hydrogen content possibly from the electroplating process may not have been resolved. The coupon geometries were chosen to permit detection of a hydrogen concentration gradient with respect to depth from the plating-substrate interface into the substrate material. This is shown schematically in Figure 4.4.

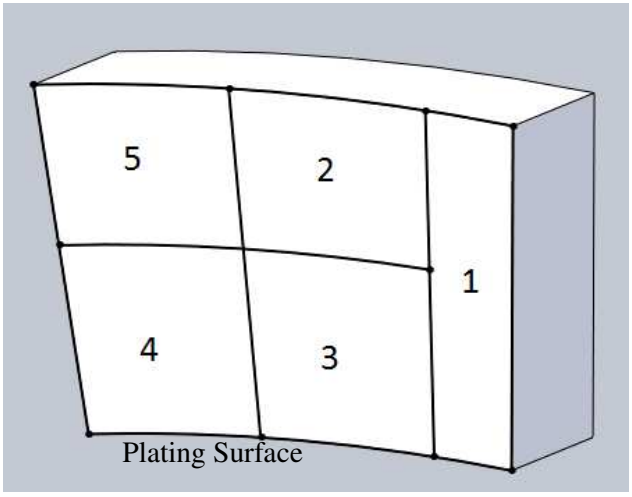

Figure 4.4: Schematic of coupon locations used for hydrogen content measurements. The plating surface is located at the bottom of Samples 4, 3 and 1.

As seen in Table 4.2, the retained hydrogen in the titanium is below the specification limit of 125 wpmm hydrogen. Furthermore, no compositional gradient of hydrogen as a function of distance from the coating-substrate interface was apparent.

Table 4.2: Hydrogen Concentration Results

Sample Number	*Hydrogen Content [wppm]*
1	*51.5*
2	*51.2*
3	*50.2*
4	*53.0*
5	*50.9*

Subsequent fractography revealed branched, tortuous crack propagation; however, linear crack growth through co-oriented α-laths was also observed. These features, shown in Figure 4.5, were thought to allow for faster crack propagation than other growth methods, due to their microstructural sensitivity and the lower plastic work done on the surrounding material, suggested by the less tortuous crack growth.

Analysis of the fracture surface from fully propagated crack regions showed a different perspective of these linear cracks in the form of facet features. Note the parallel linear cracks in Figure 4.5 and parallel planar facet features in Figure 4.6, showing different views of the same type of feature. Additionally, Figure 4.6 is located at a relatively long crack length, for observing these planar faceted features and has a rough, feathered surface similar to quasi-cleavage indicative of higher levels of plasticity associated with the higher stress intensities of a longer crack length. The secondary cracking observed is another result of the higher stress intensities. These were not isolated features, as networks of these were found to propagate across millimeters of the Ti-6-4 material, initiating at the coating-substrate interface, as shown in Figure 4.7. Site specific TEM analysis of two facet features, obtained with the FEI Helios FIB instrument, showed α laths of the same orientation in a ß matrix, indicating propagation through α colonies; however, selected area diffraction patterns were not indexed to confirm the HCP structure. The dependence of these facets on the underlying microstructure was the motivation for exploring the ß → α transformations in subsequent analyses in this project.

a)

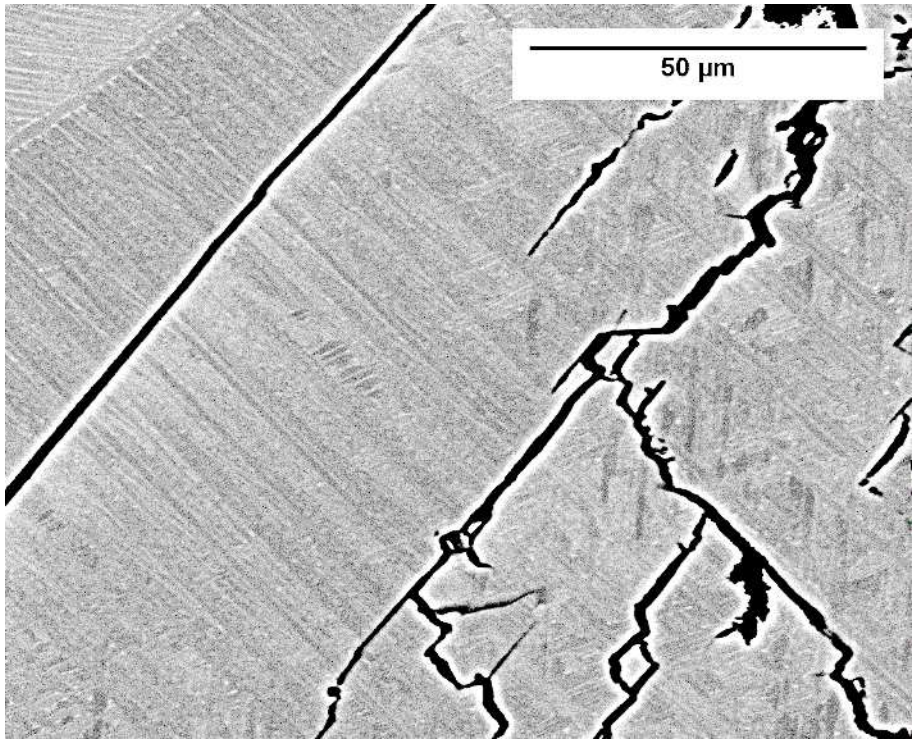

b)

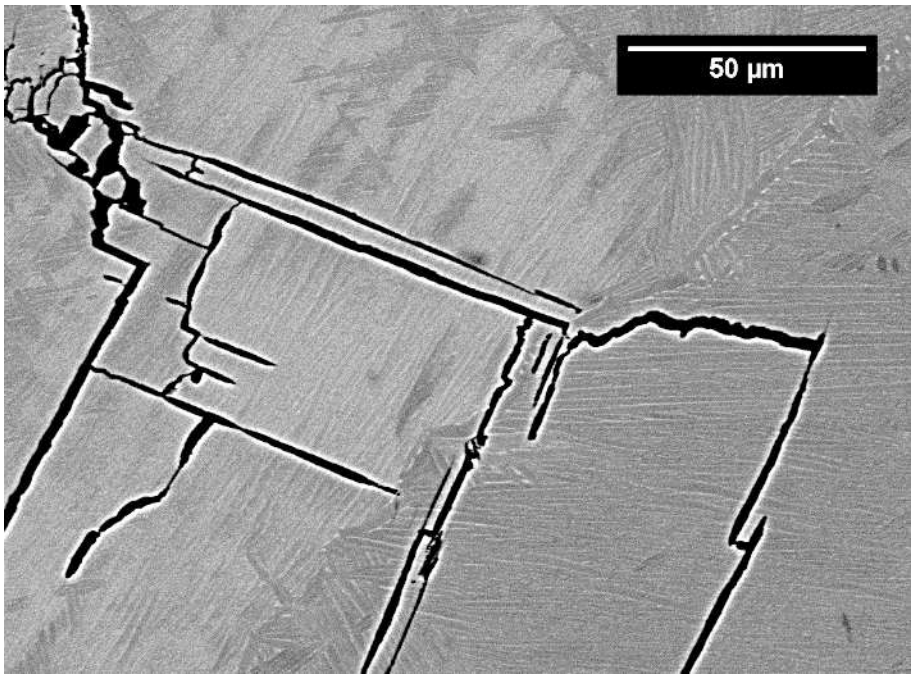

Figure 4.5: SEM micrographs of tortuous and linear branched cracking taken in BSE mode, approximately 500 µm away from the coating-substrate interface. Ti-6-4 ß-STOA material taken from the hydraulic actuator wall thickness. Macroscopic crack propagation was from the top of the images to bottom, with tensile loading horizontally left and right. Micrograph (a) shows the contrasting crack propagation path in a continuous α colony (left) and in multivariant α (right). Meanwhile, (b) shows crack path interaction and redirection across a ß grain boundary.

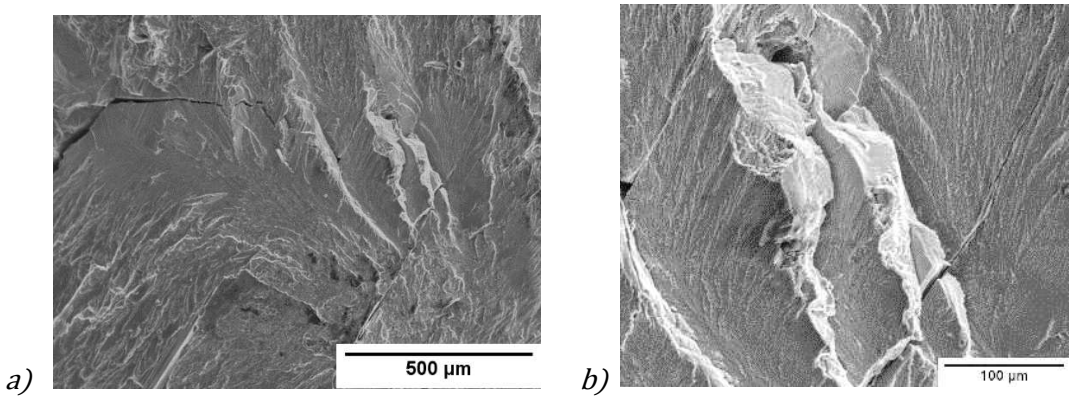

Figure 4.6: Fracture surface of a hydraulic damper unit showing (a) large facet features that form with (b) parallel facet planes. Tensile loading directions for these fracture surfaces were in and out of plane, with macroscopic crack propagation from the bottom to the top of the images.

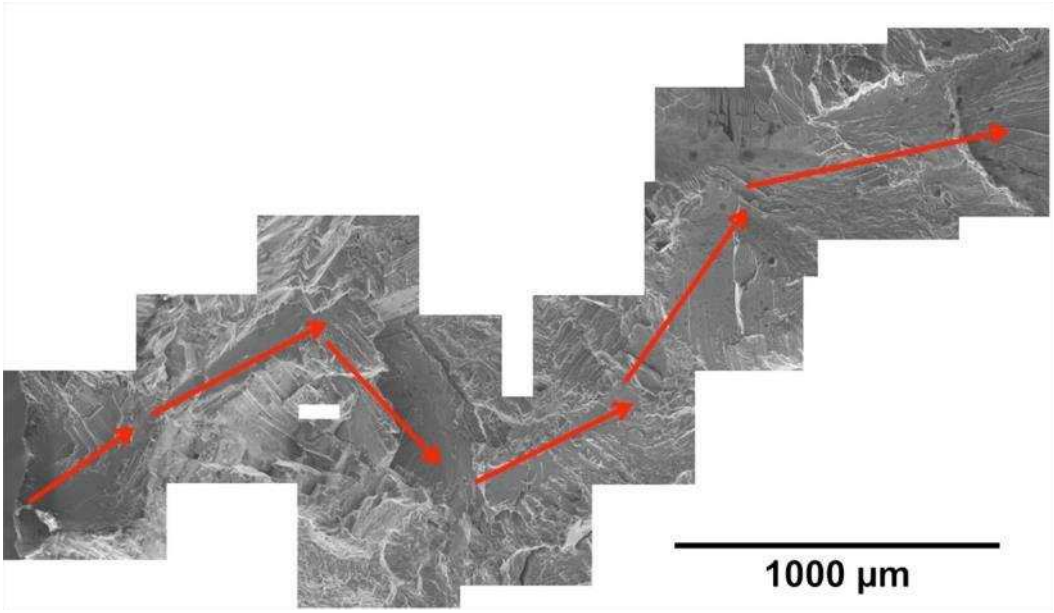

Figure 4.7: SEM micrographs of the fracture surface, showing faceted initiation (left) and propagation (right), with increasing facet surface roughness as crack length increases. Ti-6-4 ß-STOA material was taken from the hydraulic actuator wall thickness in a fully propagated crack with a fracture surface harvested by wire EDM. Tensile loading directions for this fracture surface was in and out of plane.

4.2 Quench Delay and Dilatometry Experiments

Preliminary diffusional ß → α transformations performed using quartz encapsulated specimens showed an increasing occurrence, continuity and thickness of GBα with increasing quench delay time. Likewise, α side plate formation in colonies/packets were observed to increase in a similar manner; lath

lengths ranged from 20 µm to 100 µm for QDs between 15 and 60 seconds, respectively (e.g. Figure 4.8). Note the jagged GBα in Figure 4.8a and an apparent preferred prior ß grain for colony α growth in Figure 4.8c.

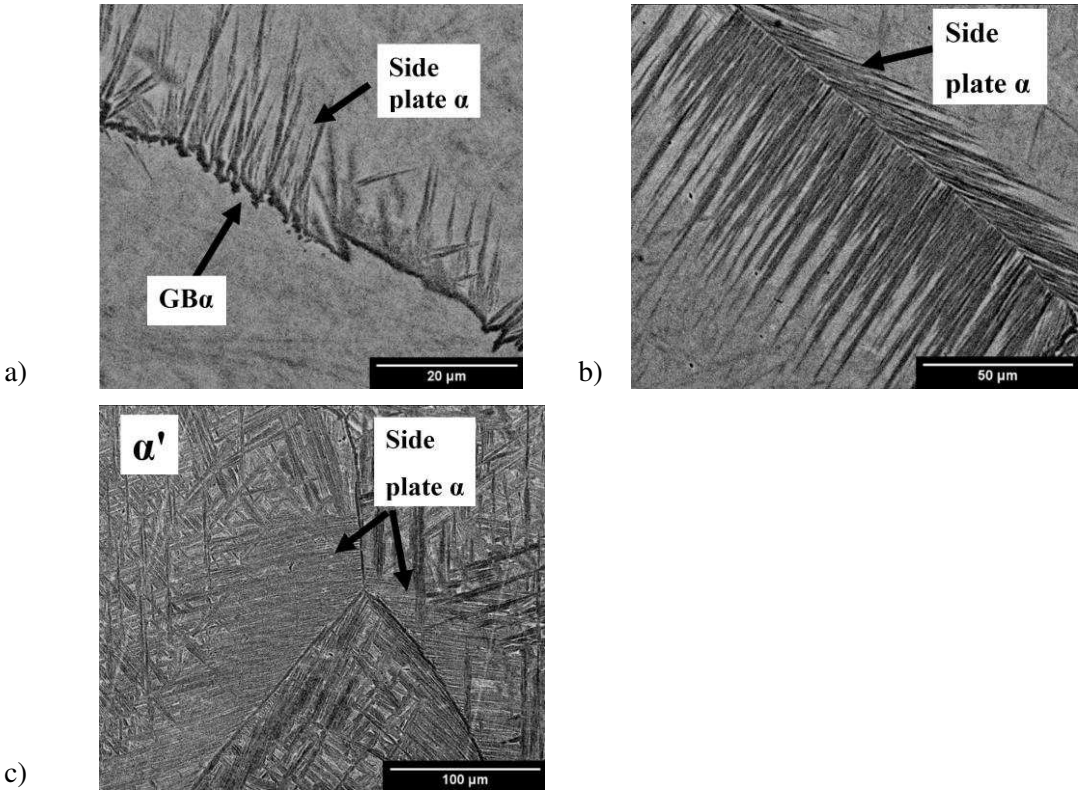

Figure 4.8: Microstructures produced in 10 mm diameter Ti-6-4 specimens for quench delays of (a) 15, (b) 30 and (c) 60 seconds.

Subsequent analysis of material was performed with the dilatometer to provide information for cooling rates not influenced by specimen thickness or capsule effects. Particular attention was given to α colony formation. Microstructures were produced using an argon gas quench dilatometer under continuous cooling between temperatures ranging from 1050 °C to 25 °C. Constant cooling rates performed in the quench dilatometer varied between 1 °C/s and 550 °C/s. The effects of neighboring grain orientations on GBα formation were examined. Due to large grain sizes reducing the number of available grains, orientation effects, and software thresholding limitations, metallographic analysis was used to report trends instead of quantified levels of α colony formation. Microstructural analysis revealed the formation of continuous GBα occurred at cooling rates of 25 °C/s and lower. At these relatively low cooling rates, the GBα thickness was approximately 10 µm for 1 °C/s, and quickly decreased to

approximately 3 µm for cooling rates between 2 and 50 °C/s. Sporadic and discontinuous GBα was present at cooling rates of 50 °C/s to 150 °C/s, with decreasing continuity and presence as the cooling rate was increased. The presence of GBα was completely suppressed at 550 °C/s.

Colony structures, or "packets" of single variant α precipitation, occurred via side plate growth off of GBα. Higher cooling rates that decrease the continuity of the GBα promoted smaller colony widths, as well as shorter colony lath lengths. At cooling rates less than 5 °C/s, entire prior-β grains were transformed to α colonies. At increasing cooling rates of 5, 10 and 25 °C/s, colony lengths were approximately 50 µm, 25 µm, and 10 µm, respectively. Additionally, for these intermediate cooling rates, the occurrence of colonies was reduced and often occurred at prior-β grain boundary triple junctions. At cooling rates above 25 °C/s, no appreciable colony structure was observed. At all cooling rates explored using the quench dilatometer, including 550 °C/s, vanadium partitioning was evident from Z-contrast in the backscattered electron mode of the SEM.

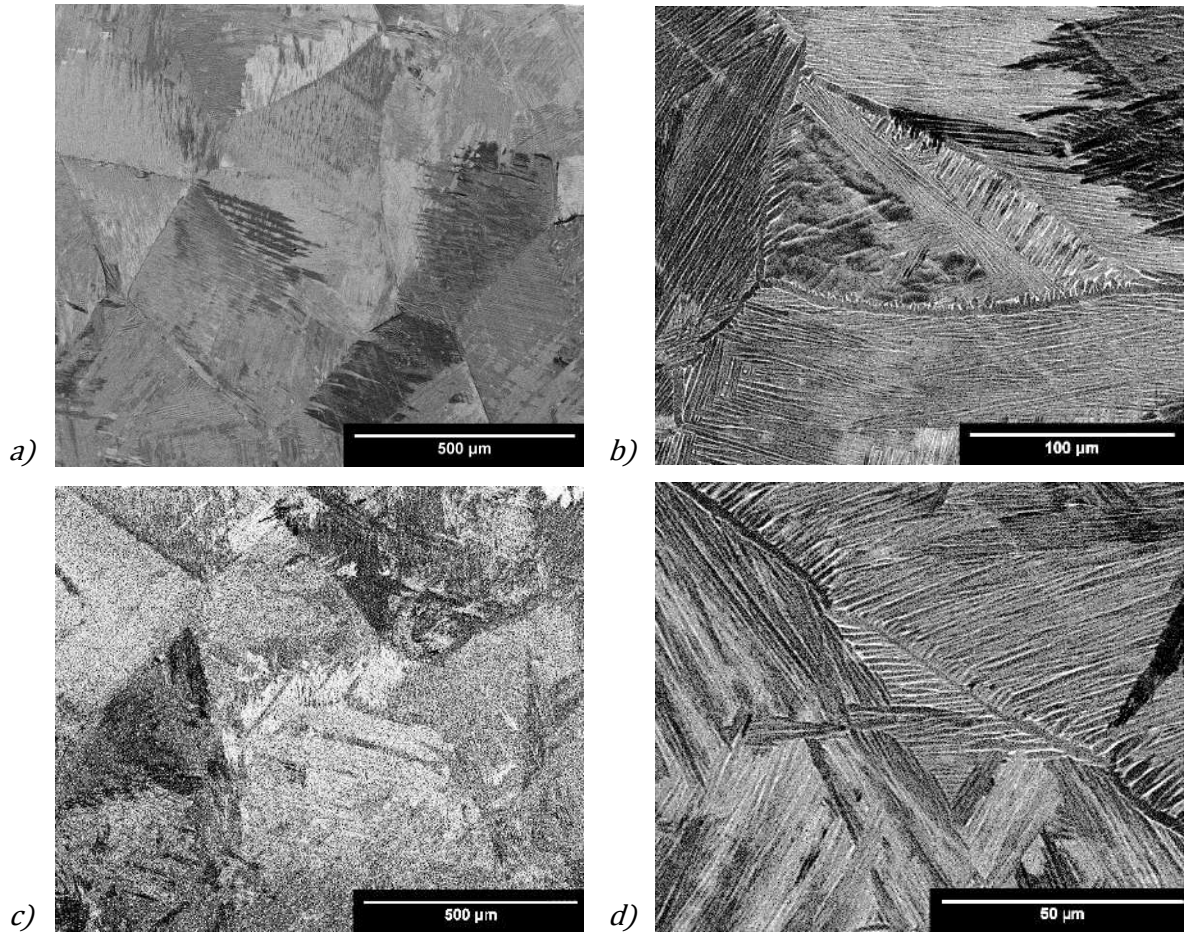

Figure 4.9: SEM-BSE micrographs showing effects of cooling rate on the microstructure of Ti-6-4 for 1 °C/s (a,b), 2 °C/s (c,d), 5 °C/s (e,f), 10 °C/s (g,h), 25 °C/s (i,j), 50 °C/s (k,l), and 550 °C/s (m,n).

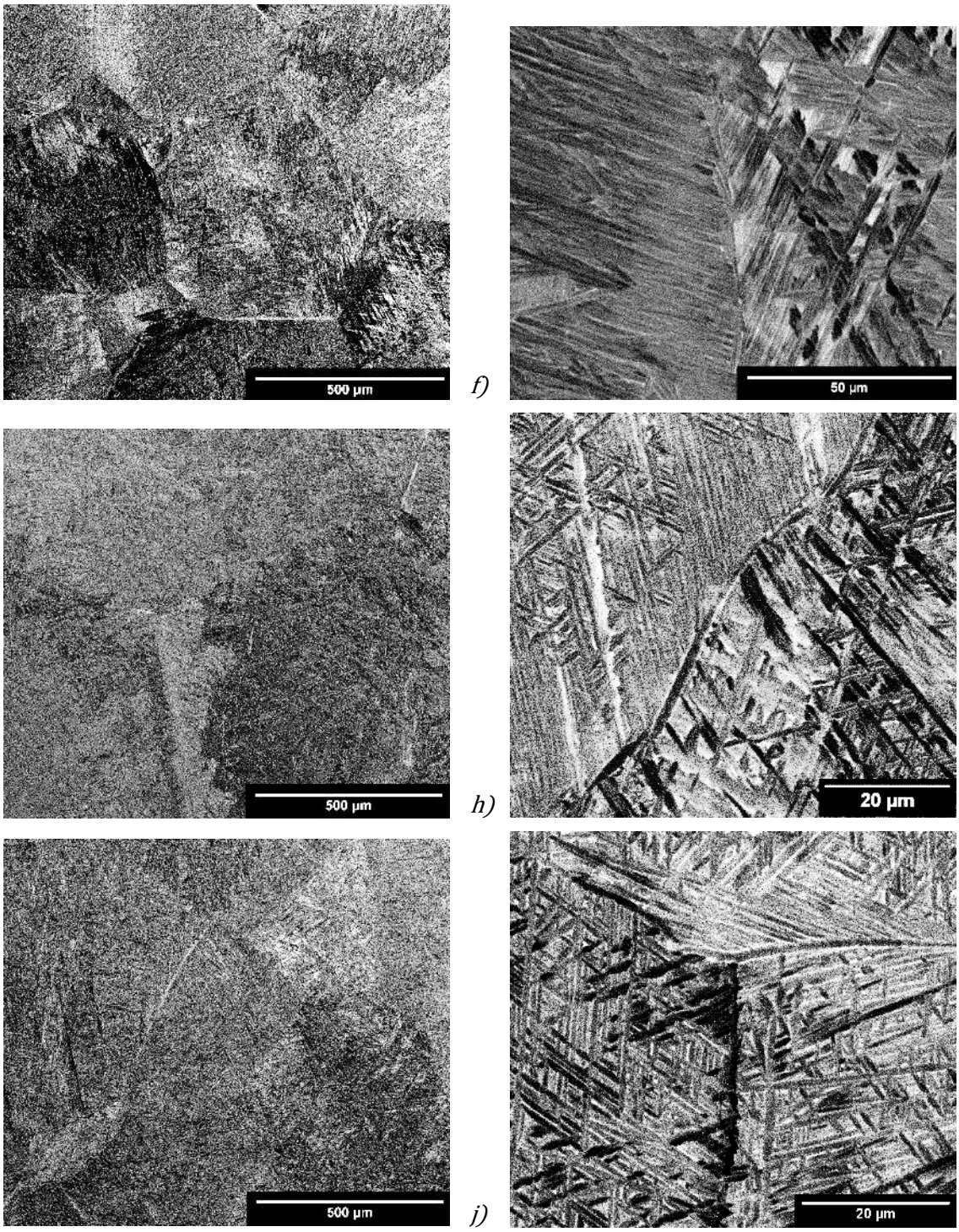

Figure 4.9: Continued.

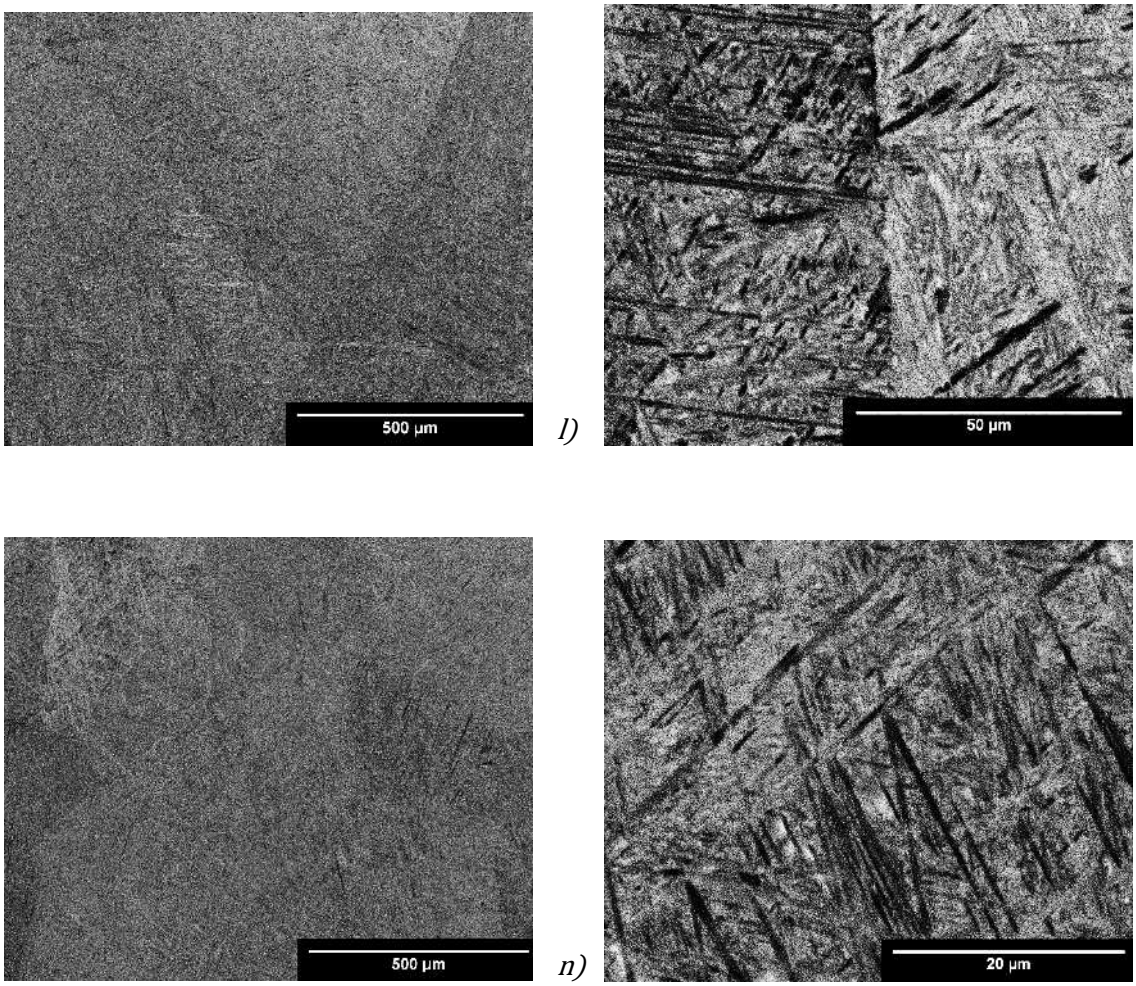

Figure 4.9: Continued.

The effects of temperature on the β to α transformation were explored using interrupted cooling studies in the quench dilatometer. Samples were quenched rapidly from 1050 °C to a desired temperature in the α + β phase field (950 °C – 700 °C) and held for a defined time (5, 30, or 300 s) before quenching rapidly to room temperature. The data produced using this method are similar to those used to produce time-temperature-transformation (TTT) plots. At 5 s hold times, GBα precipitation started at 925 °C and produced minor (20 µm in length) side plate growth from 875 °C to 825 °C. At 800 °C for a 5 s hold time, side plate growth decreased in length and occurrence. Utilizing 30 s hold times, GBα with minor side-plate growth occurred at triple junctions for temperatures of 950 °C to 875 °C. At 850 °C for a 30 s hold time, continuous GBα was present and the entire prior-β grain contained thin, interpenetrating packets of "basketweave" α laths, as seen in Figure 4.14. At 825 °C, the 30 s hold time prevented most GBα formation, and α lath morphology was multi-variant without colony formation. A 300 s hold time at 950 °C resulted in relatively thick GBα, as well as coarse side plate growth at triple junctions. From 925 °C to

875 °C, 300 s hold times produced GBα side plate growth throughout the entire prior-β grain, similar to the 30 s hold time. At 850 °C and 825 °C, 300 s hold times produced the same results as 30 s hold times; limited GBα with basketweave and multi-variant α morphology. With decreased hold temperatures of 800 °C through 700 °C, the α morphology remained a multi-variant Widmänstatten morphology.

Observations from the heat treatment operations in the dilatometer provided roughly three microstructural morphologies of the α, produced as a result of cooling from above the β transus (1050 °C). Slower cooling rates below 5 °C/s produced colony growth throughout the entire prior-β grain, and TTT information showed GBα formation at 925 °C and complete α colony formation from 900 °C through 875 °C. Intermediate cooling rates and transformation temperatures of 5 °C/s to 25 °C/s and 850 °C to 825 °C, respectively, produced a basketweave of interrupted α packets. Finally, at cooling rates exceeding 25 °C/s and transformation temperatures below 825 °C, GBα is suppressed and α laths precipitated in a multi-variant manner.

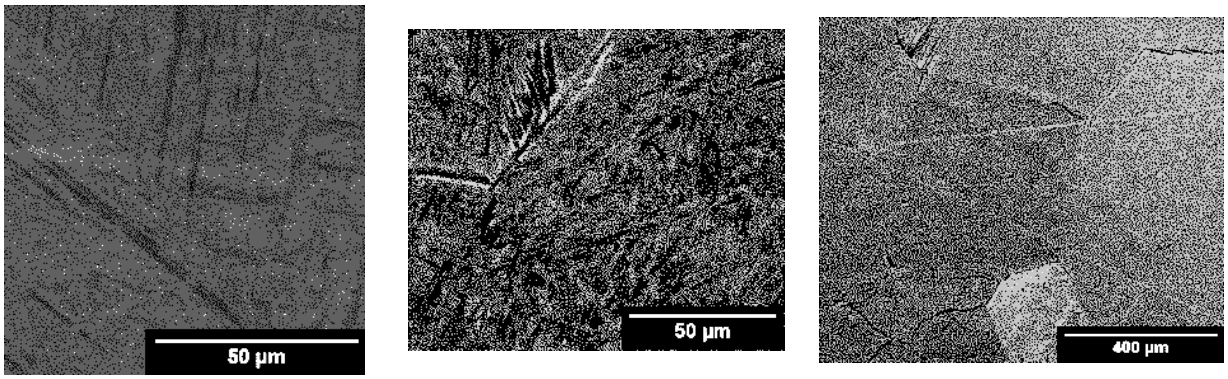

a) *b)* *c)*

Figure 4.10: Microstructures produced in Ti-6-4 from holding at 950 °C for times of (a) 5, (b) 30, and (c) 300 seconds with subsequent water quenching.

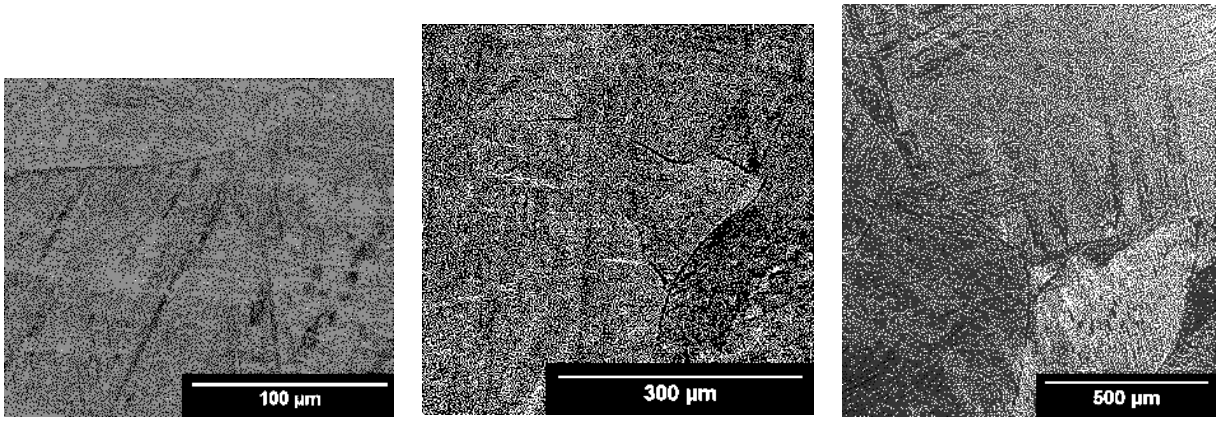

a) *b)* *c)*

Figure 4.11: Microstructures produced in Ti-6-4 from holding at 925 °C for times of (a) 5, (b) 30, and (c) 300 seconds with subsequent water quenching

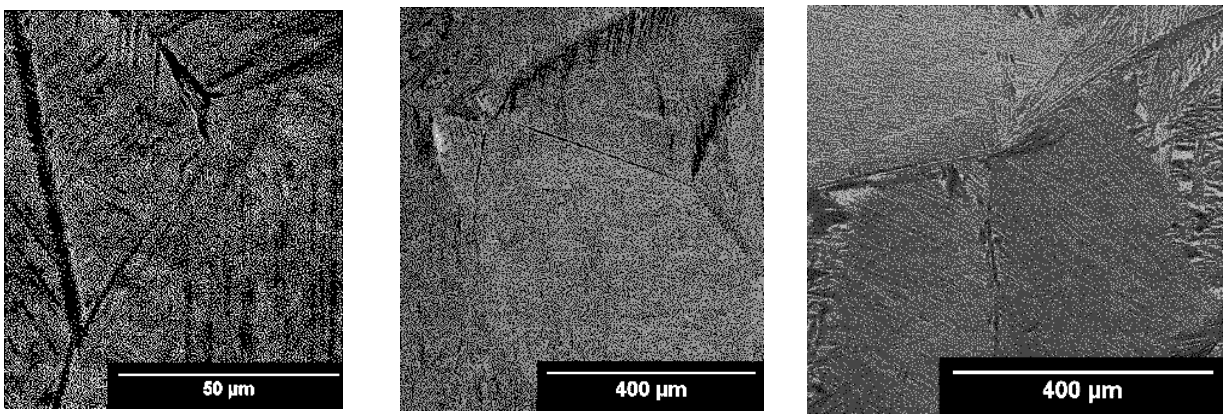

a) *b)* *c)*

Figure 4.12: Microstructures produced in Ti-6-4 from holding at 900 °C for times of (a) 5, (b) 30, and (c) 300 seconds with subsequent water quenching.

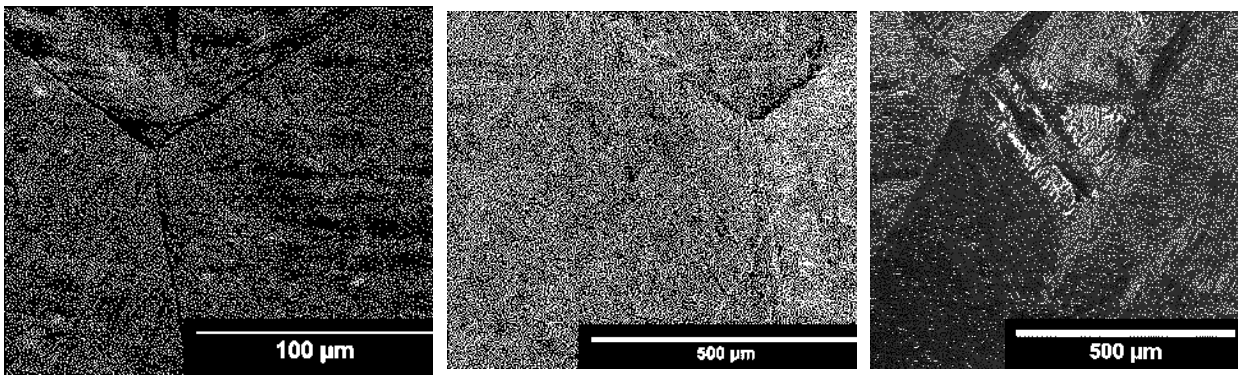

a) *b)* *c)*

Figure 4.13: Microstructures produced in Ti-6-4 from holding at 875 °C for times of (a) 5, (b) 30, and (c) 300 seconds with subsequent water quenching.

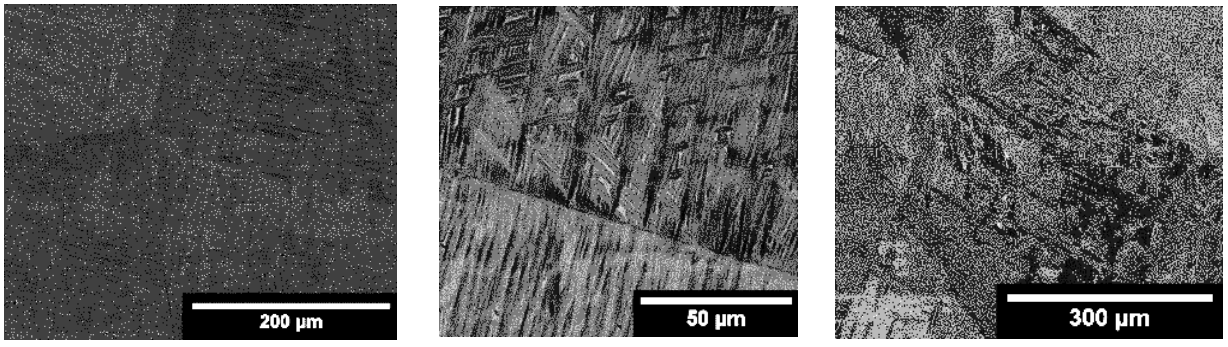

a) *b)* *c)*

Figure 4.14: Microstructures produced in Ti-6-4 from holding at 850 °C for times of (a) 5, (b) 30, and (c) 300 seconds with subsequent water quenching.

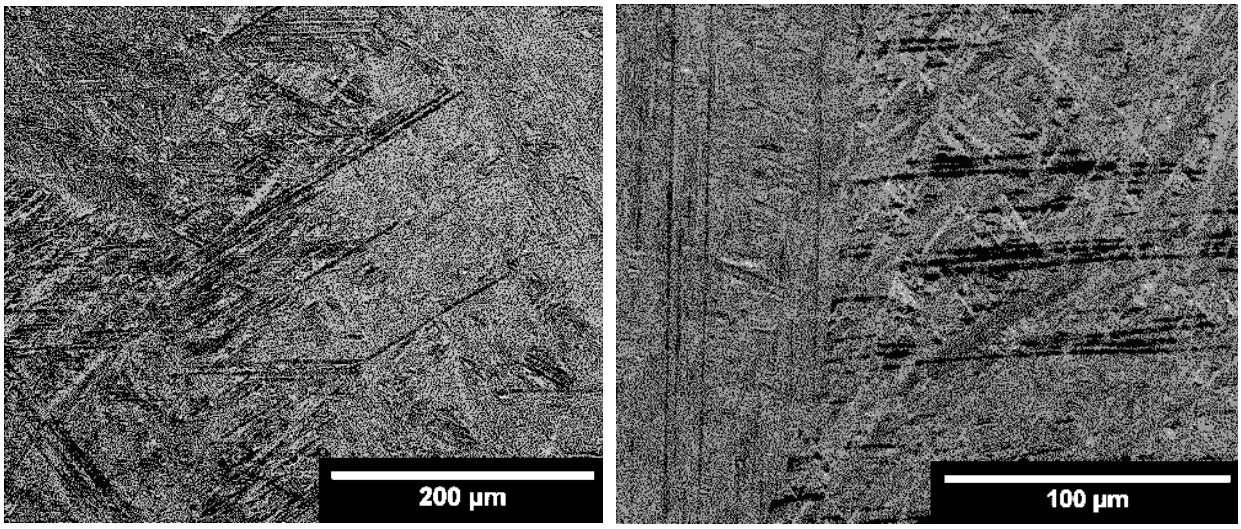

a) *b)*

Figure 4.15: Typical microstructures produced in Ti-6-4 from holding at 825 °C and lower temperatures for 300 seconds with subsequent water quenching, shown in (a) and (b).

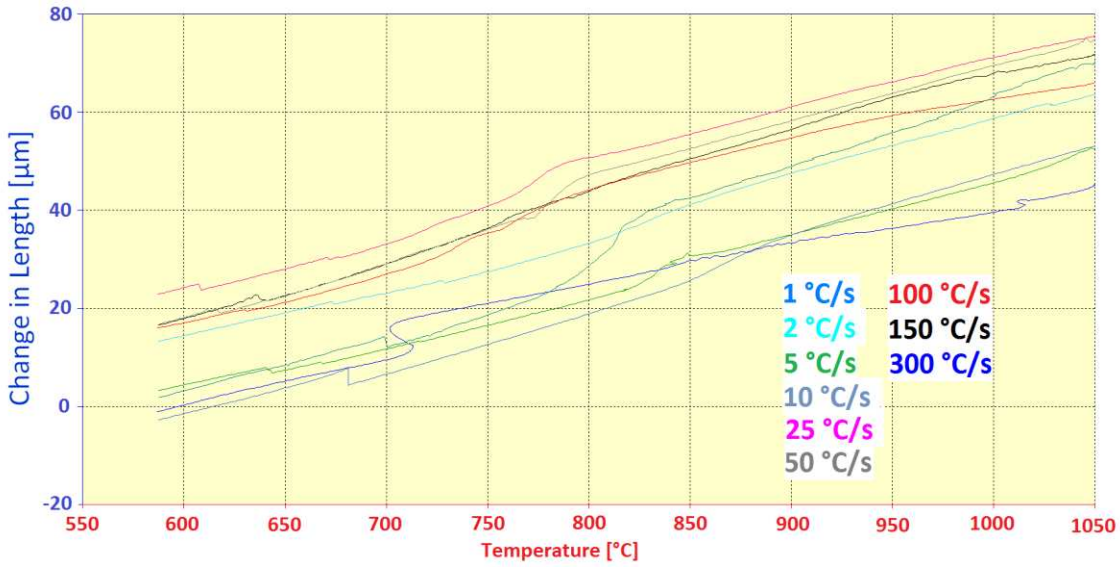

Figure 4.16: Compiled dilatometry results for various cooling rates from 1050°C (above the ß transus). Results show a decreasing transformation temperature with increasing cooling rates.

Table 4.3: Transformation temperatures for various cooling rates

Cooling rate (°C/s)	*Transformation Start Temperature (°C)*	*Transformation Finish Temperature (°C)*
1	*900*	*850*
2	*875*	*825*
5	*850*	*825*
10	*840*	*815*
25	*810*	*760*
50	*800*	*775*
100	*775*	*750*
150	*775*	*740*
300	*700*	*700*

In addition to providing precise control of the temperature and cooling rates, the dilatometer's linear variable differential transformer (LVDT) measured change in length of the sample. Figure 4.16 displays the decreasing transformation temperature (shown by the non-linear region of each plot) with increasing cooling rates. Approximate values for transformation start and finish temperatures, taken from Figure 4.16, are shown in Table 4.3. Note that the 550 °C/s specimen had significant vibrations due to high gas flow, so the dilatometry data was not utilized.

Compilation of this information into a graphical format can be done by the familiar continuous cooling rate transformation (CCT) and time-temperature-transformation (TTT) curves shown in Figure 4.17a and b, respectively. Dilatometry data of change in length versus temperature was used in conjunction with the micrographs for the CCT curve construction. Note the required cooling rates to fully suppress continuous GBα and subsequent colony formation are in excess of 50 °C/s; however, the α colony formation is reduced with cooling rates exceeding 5 °C/s to small packets of ~50 μm in width and length. These results differ from Ahmed's [1], showing that low cooling rates at or less than 5°C/s are required for α colony formations (labeled "massive α" by Ahmed), rather than being produced from 410°C/s cooling rates. It is proposed that Ahmed misinterpreted the actual temperatures and cooling rates that the transformations occurred at, due to not having any method of measuring the transformation temperatures.

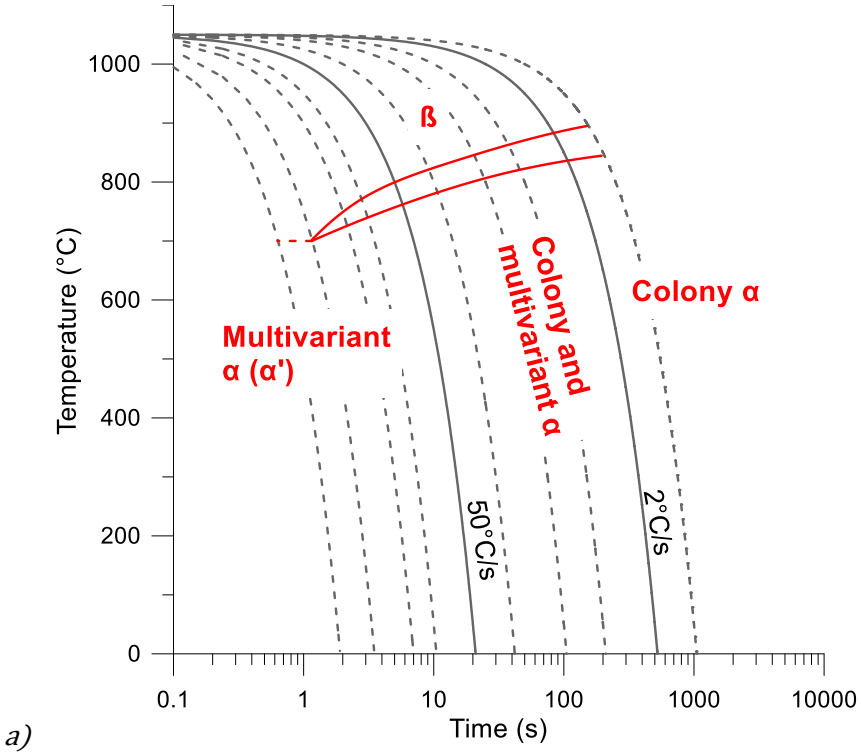

a)

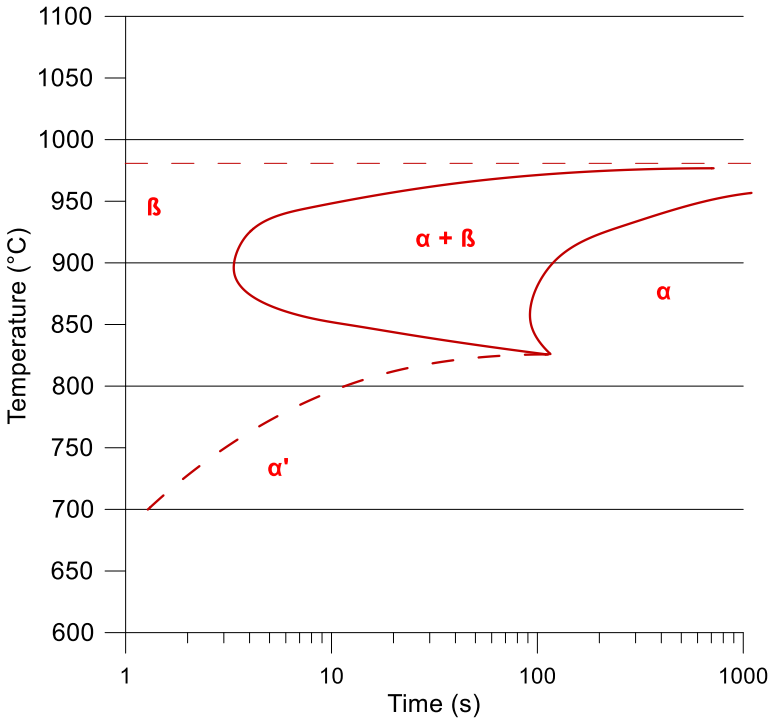

b)

Figure 4.17: Graphical summary of dilatometry work in (a) CCT and (b) TTT curves for Ti-6-4, based upon α morphology. Note that the α' line is tentatively based upon dilatometry results and more work is required for

4.3 Determining Attainable Cooling Rates

Establishing which cooling rates are feasible for Ti-6-4 forgings is important, as part size, surface condition, and quenching media will all play a role. The present dilatometry work laid the groundwork for predicting the microstructure, based upon a known thermal history for the material. Thermal modeling of water quenching requires a convective cooling coefficient value, "h", to account for surface effects of the material and boiling of the quenching media. A large specimen size, representative of a large forging, and cooling conditions were modeled in ANSYS FEA software and compared to experimental data, as shown in Figure 4.18, to determine an appropriate convective cooling rate coefficient. Note the better fit of 1000 $\frac{W}{m^2K}$, appropriate for stirred media, compared to the 800 $\frac{W}{m^2K}$ that was previously determined for a stagnant quench. It is believed that industrial capabilities utilizing tooling with pressurized water quench jets are capable of higher forced convection than manually stirring the part in a water quench tank. This convective cooling coefficient value allows for more complex geometries to be modeled, such as the original hydraulic actuator forging.

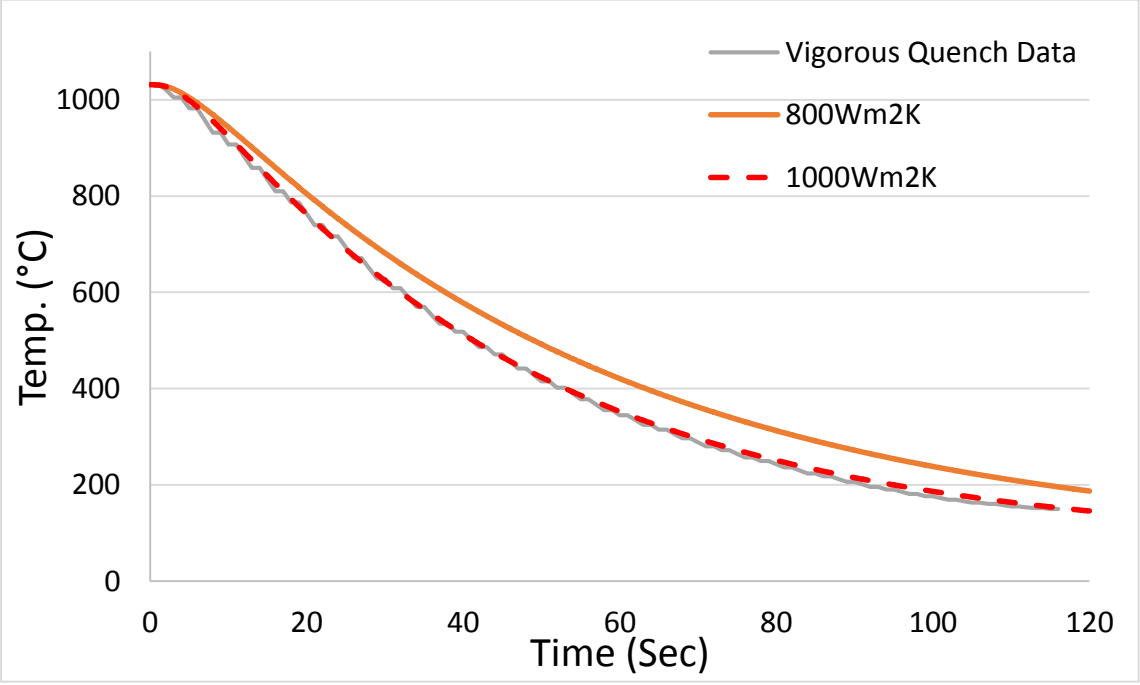

Figure 4.18: Temperature vs. time curve fitting for FEA model predictions with various convective cooling coefficient values for the experimental data.

Transient thermal finite element modeling utilizing this convective cooling coefficient was performed on the hydraulic damper forging as a case example. Thermal probes were input in the model at

locations of increasing distance from the surface of the internal diameter, as shown in Figure 4.19 (with a cross sectional view), and temperature data for each location was acquired. Note the approximate locations of the thermal probes highlighted by the black rectangle in Figure 4.19.

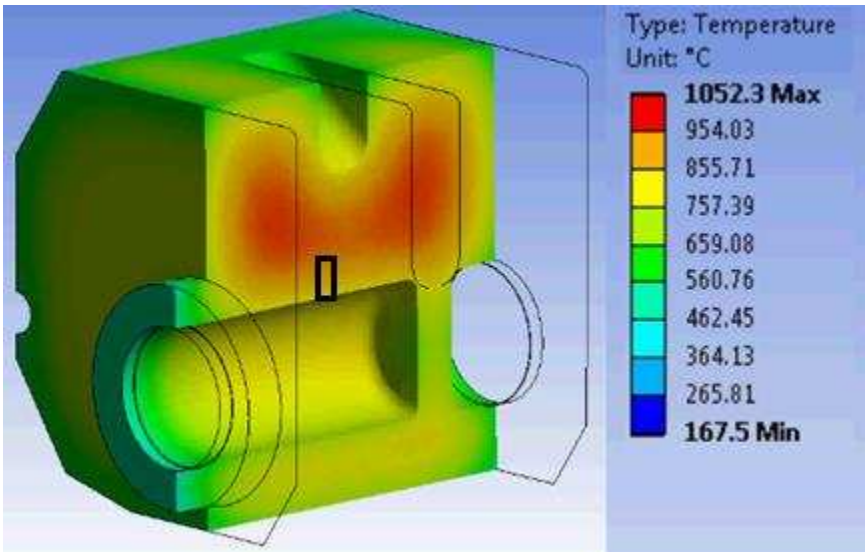

Figure 4.19: Image from a time-lapse transient thermal model for convective cooling of a Ti-6-4 hydraulic damper forging.

This modeling data is plotted in a manner to view cooling rate as a function of temperature (Figure 4.20). Note that time is not a displayed variable here, and increasing depths are cooling through these temperatures at increasing times. From these results, combined with the knowledge from previous dilatometry work, it can be seen that the cooling rates are approximately 5 °C/s in the transformation temperature range of 850-900 °C. This is a sufficiently high cooling rate to suppress large α colony formation; however, an interwoven basketweave α morphology of thin elongated packets with small α colonies near prior ß grain boundaries is expected, based upon the dilatometry work performed here.

4.4 Crystallographic Analysis of Facet Features

Using EBSD, facet features shown in a 2-dimensional representation were observed to share a close relation with the $(0001)_{\alpha}$ trace of the α colony that the crack was propagating through. The regions analyzed are shown in Figure 4.21, with EBSD map overlays in Figure 4.22. Material removal using a FIB allowed observation of a second trace to obtain full 3-dimensional information confirmed a near basal plane facet orientation. Angular differences between the facet plane and $(0001)_{\alpha}$ were between 10-15° for three independent features. Note the different α colony orientations within a single ß grain in

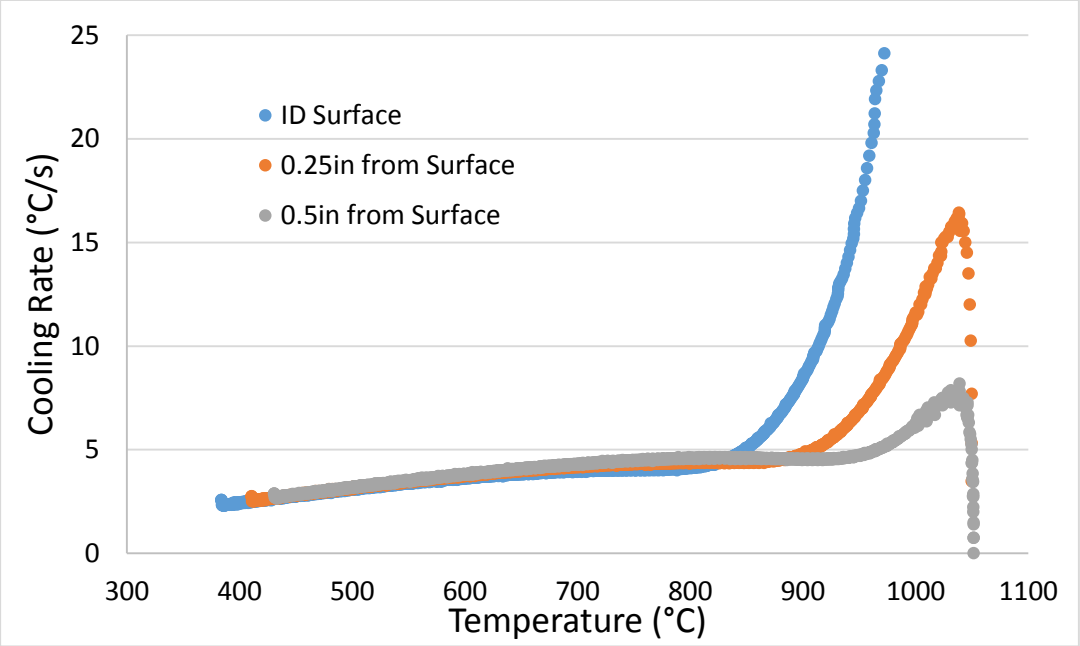

Figure 4.20: Thermal model data plotted as cooling rate versus temperature plot for different locations in the forging unit.

Figure 4.22b having similar crystallographic orientations, with rotations about the $(0001)_{\alpha}$, while still creating high geometric angular variations. As previously demonstrated by Sharma et al. [8], α colony formations of similar orientations existing in two neighboring ß grains are possible when the ß grains share a common $\{110\}_{ß}$ plane. These neighboring ß grains may have a high angle grain boundary, while still precipitating closely oriented α colonies by a rotation about the common $\{110\}_{ß}$ plane. Determination of the ß orientation requires back calculation from multiple α orientations or a higher resolution diffraction technique such as Transmission Kikuchi Diffraction (TKD).

4.5 Rotating Bending Fatigue Testing

Fatigue testing to evaluate the crack initiation stages in high cycle fatigue was performed to compare the two different heat treatments (minimal QD and representative QD) and resulting microstructures, as shown in Figure 4.23. The majority of the specimens were tested at the same maximum stress level of 728 MPa; other specimens were used to find the optimum loading for desired cycles-to-failure, but were not used for further analysis. Results from rotating bending fatigue of smooth specimens, shown in

Figure 4.24, include more than a two orders of magnitude difference in fatigue life

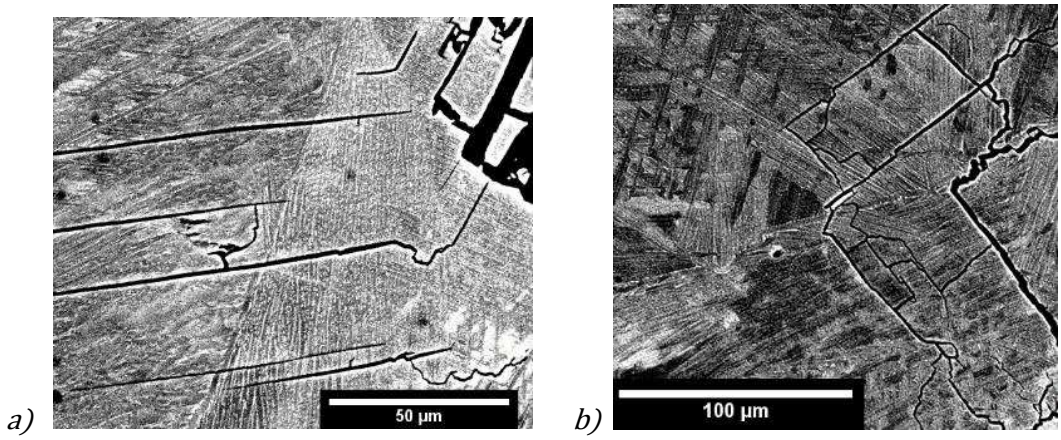

Figure 4.21: Parallel crack growth regions taken from two independent cracks taken from the hydraulic actuators in a quench delayed ß-STOA condition. Note the crack path in (a) propagating across the ß GB and maintaining a linear growth. Additionally, the crack path in both (a) and (b) demonstrates linear crack growth through different α variants sharing a $(0001)_\alpha$. Tensile loading in these harvested fracture surfaces are left to right, with macroscopic crack propagation from top to bottom of the micrographs.

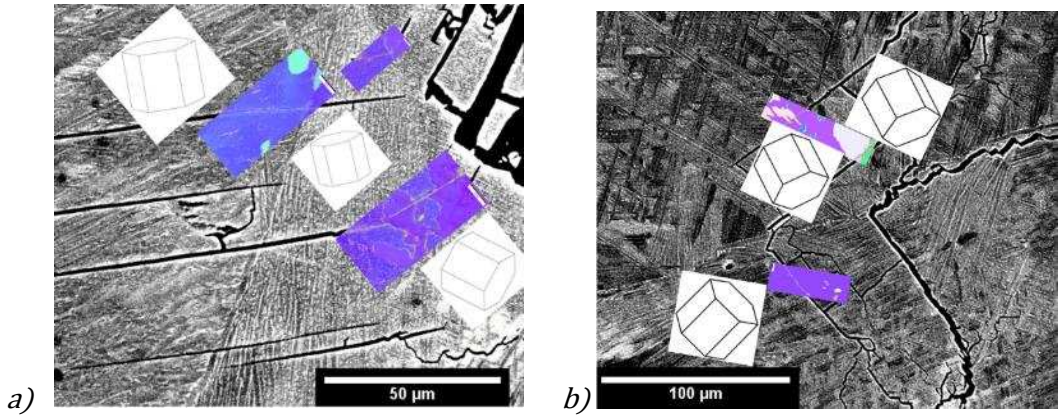

Figure 4.22: EBSD map and α HCP orientation overlays for regions analyzed.

in the high cycle fatigue regime, due to the colony α formation as a result of the representative quench delay. A single specimen of the "minimal QD" condition failed quite early (approximately 53,000 cycles). Observations of the specimen's outer surface indicated that failure appeared to be due to a surface defect caused by machining or improper handling.

Post-mortem fractography of the fracture surfaces showed differences in regions of crack initiation and propagation for the different QD conditions. Figure 4.25Figurea shows a macroscopic fracture surface for a minimal QD specimen with initiation occurring at the top of the image and crack propagation along the perimeter of the specimen and downward, due to stress gradients inherent in

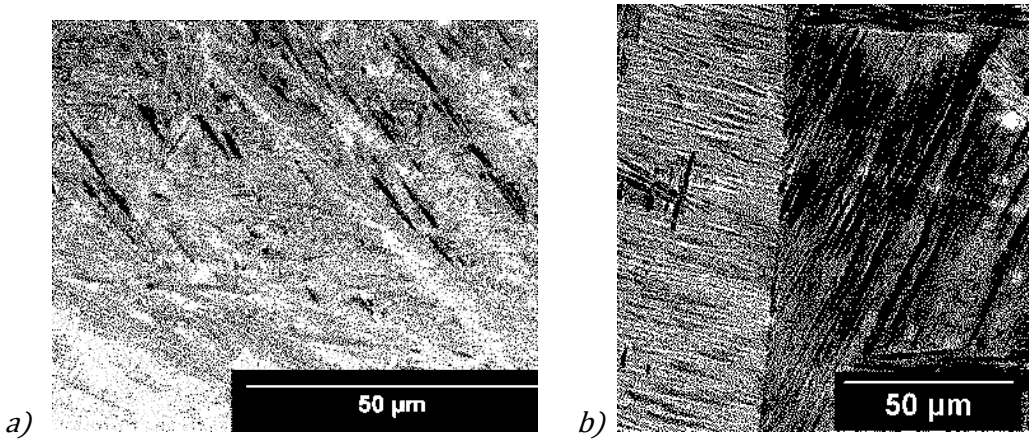

Figure 4.23: Microstructures produced in the (a) minimal quench delay (less than 5 seconds) and (b) representative quench delay (90 seconds) rotating bending fatigue specimens. Note that the quench delay time occurred under vacuum, within the quartz capsule.

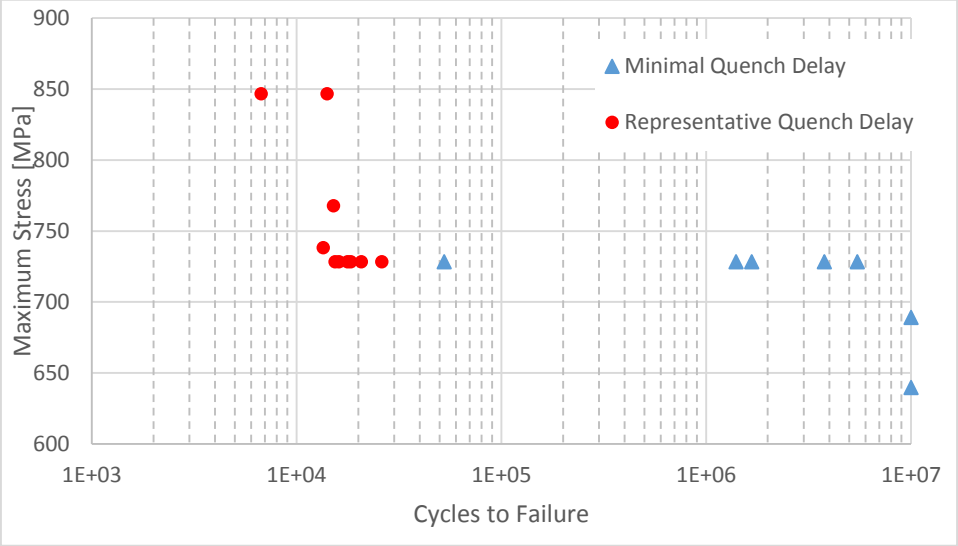

Figure 4.24: Rotating bending S-N fatigue curve with results for two different heat treatment conditions.

bending. Fast fracture occurrs on the last half of the specimen, showing prior ß grain boundary separation during overload. Figure 4.25Figureb is a higher magnification image of the same specimen, showing the initiation region. Interpretation of this fracture surface is impaired, due to fracture surface damage inherent with the compressive loading conditions. However, it appears that damage accumulation along a prior ß grain boundary was the source and location of fatigue crack initiation. Figure 4.26 shows the fracture surface of the "representative QD" specimen with colony α microstructure. Multiple initiation facet features were located along the perimeter of the specimen, particularly located along the left and

right side of the specimen, with final fracture occurring in the central, upper, and lower regions. Note the raised, out of plane features at the top and bottom of the image.

4.6 Fatigue Crack Growth Rate Measurements

Determination of the fatigue crack growth rates were performed with in situ voltage measurements. Normalized results for the two heat treatment conditions are shown in Figure 4.27. Note this is a cropped data set that only contains the stage 1 regime of fatigue crack growth rates. The full data set extends to a normalized voltage of approximately 1.3.

Utilizing a correlation between voltage ratio and crack length, fatigue crack growth rates were determined as a function of stress intensity; commonly known as a da/dN vs. ΔK curve. This plot, shown in Figure 4.28, shows a similar crack growth rate for each condition, with the representative QD specimen having a slightly lower growth rate. Note the break in data at approximately 15 MPa$\sqrt{m}$, due to separate curve fitting techniques required to eliminate systematic noise in the data. Unstable crack propagation (i.e.; fast fracture) occurred shortly after the high stress intensity fatigue crack propagation in Figure 4.28, but is not displayed. Threshold stress intensities for each heat treatment condition are nearly identical, but this may have been forced, due to identical loading conditions and starting geometries. Load shedding methods for threshold stress intensity values may be required for more accurate determinations.

Fracture surfaces displayed different features at the initiation stages of the notch for the representative and minimal quench delay specimens. Facet initiation and propagation was observed in the representative quench delay specimen (Figure 4.29), while a surface-intersecting ß grain boundary appeared to initiate crack growth with propagation occurring through multi-variant α (Figure 4.30). Qualitatively, the representative quench delay specimen had a macroscopically rough fracture surface, resulting from the crack path redirection associated with the α colonies. The minimal quench delay specimen had a macroscopically flat and smooth fracture surface, allowing for crack propagation perpendicular to the loading axis.

4.7 Tensile Testing and Microhardness

Tensile loading of specimens demonstrated a 5% lower calculated ultimate tensile strength of the representative quench delay material in comparison to the minimal quench delay (90 seconds and < 5 seconds, respectively). The load versus displacement curves are shown in Figure 4.31; however, note that

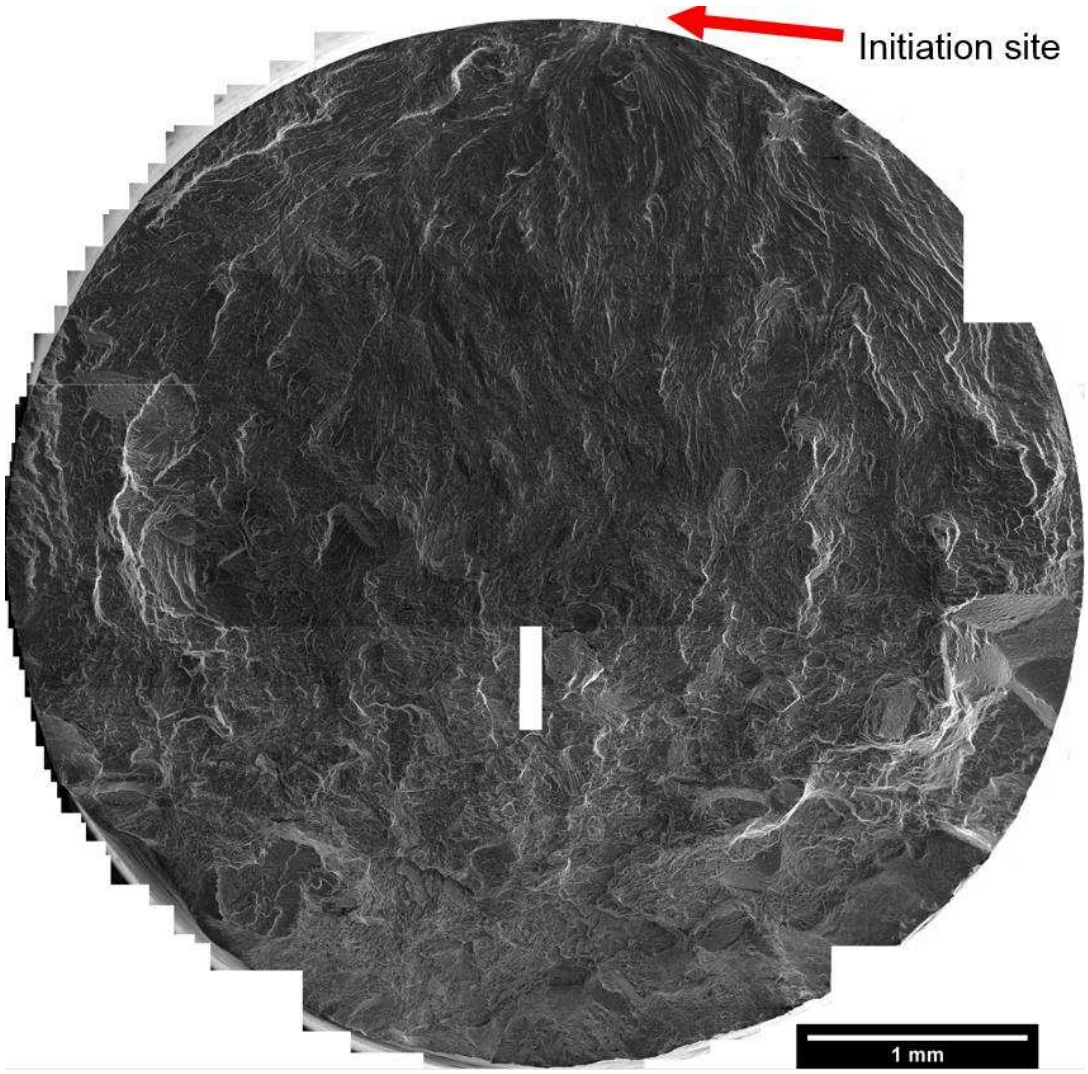

a)

Figure 4.25: Fracture surface of a typical “minimal QD” (less than 5 seconds) ß-STOA specimen, showing (a) initiation at the top region with subsequent propagation and final fracture with separation along prior ß grain boundaries. Higher magnification (b) of the initiation region displays an apparent initiation on the upper right region of the image, with crack redirection at an α colony or ß GB in the middle region. Note the fracture surface damage due to compressive loading in and out of the plane. Cycles to failure for this specimen were approximately 3.8M.

b) 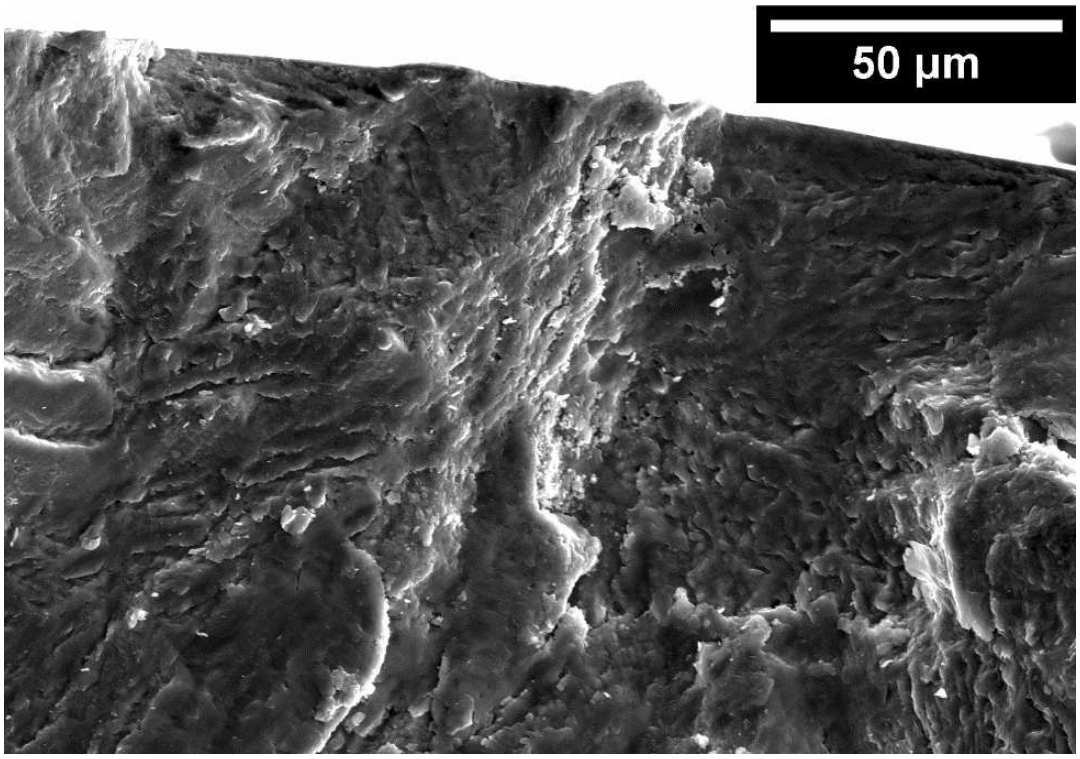

Figure 4.25: Continued.

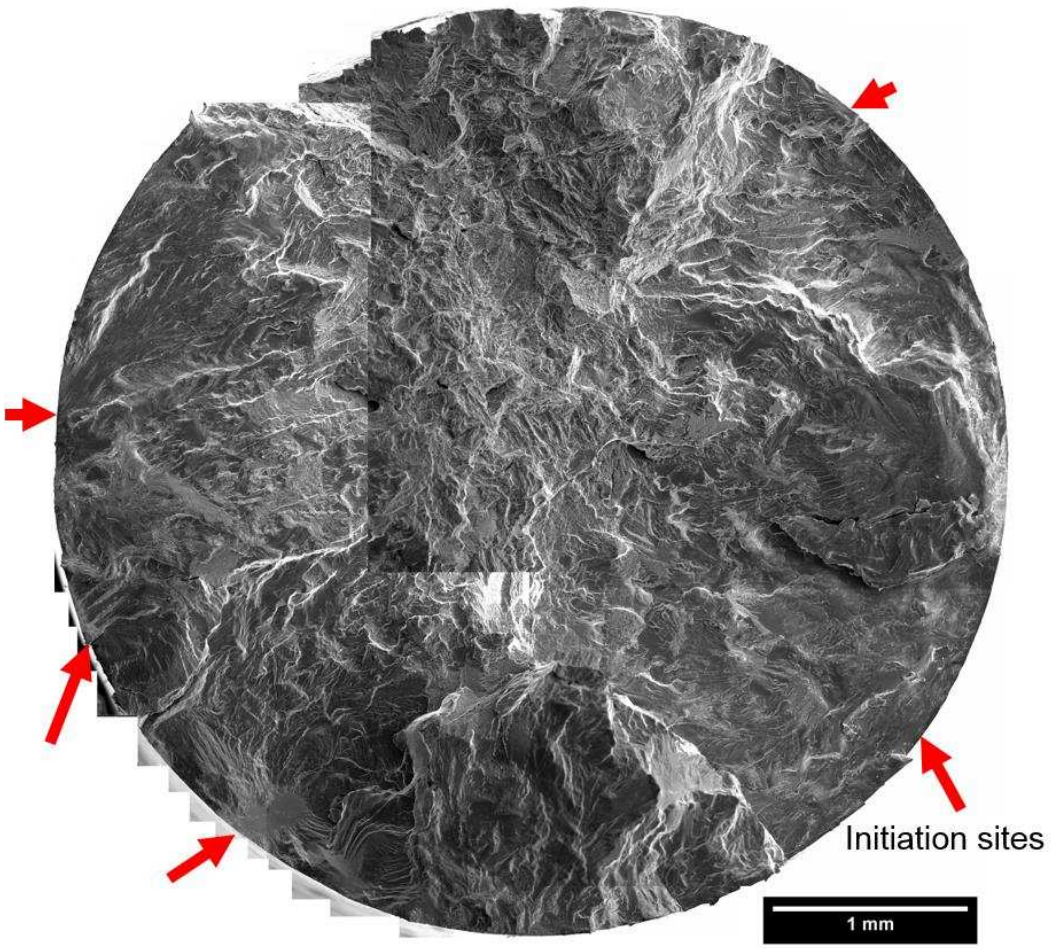

Figure 4.26: Fracture surface of a typical “representative QD” (90 seconds) ß-STOA specimen, showing multiple initiation features on many sides of the fracture surface. Note the feature at the lower central position coming out of plane and secondary cracking on the central right position. Cycles to failure for this specimen were approximately 16,000.

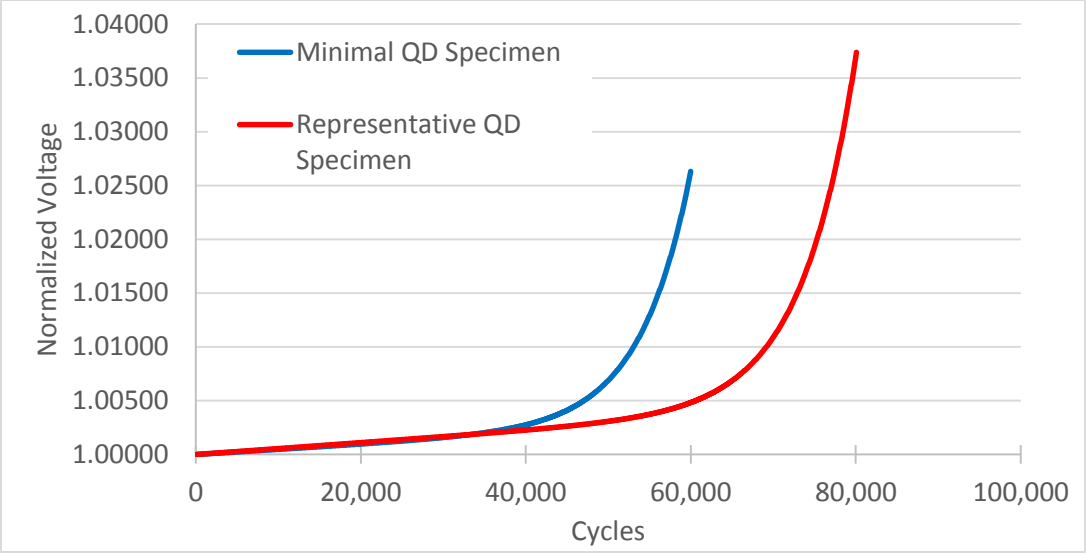

Figure 4.27: Normalized voltage measurements as a function of cycles for the initiation stages for minimal quench delay (less than 5 seconds) and representative quench delay (90 seconds) ß-STOA Ti-6-4.

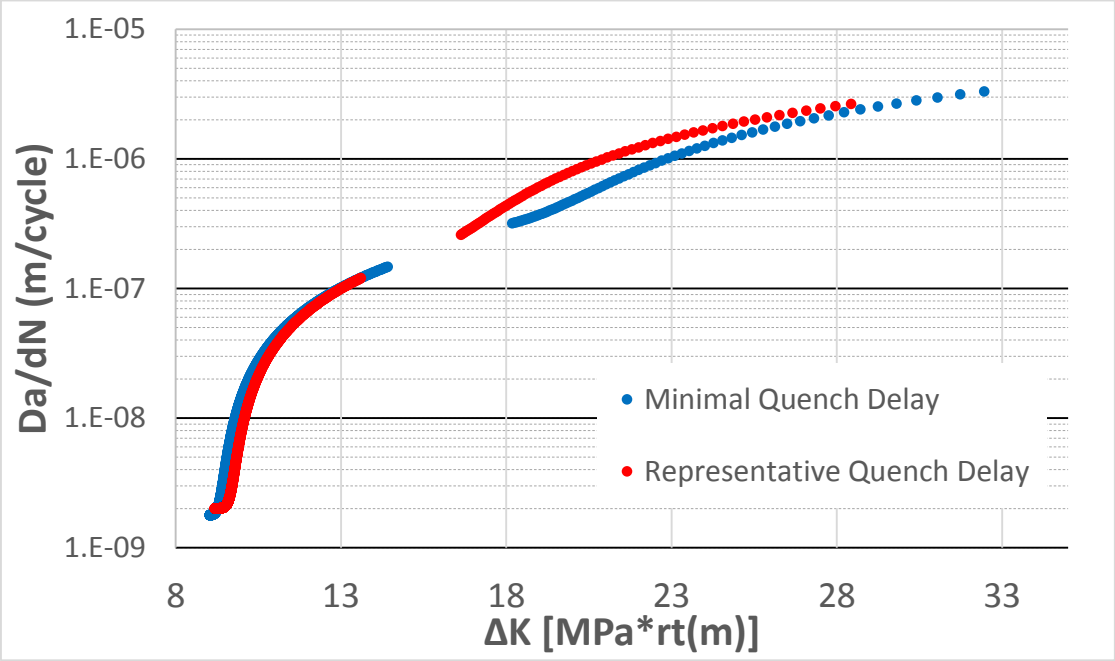

Figure 4.28: Fatigue crack growth rate of minimal (< 5 seconds) and representative (90 seconds) quench delay Ti-6-4. Cropped data shows stage I and stage II fatigue crack growth regimes.

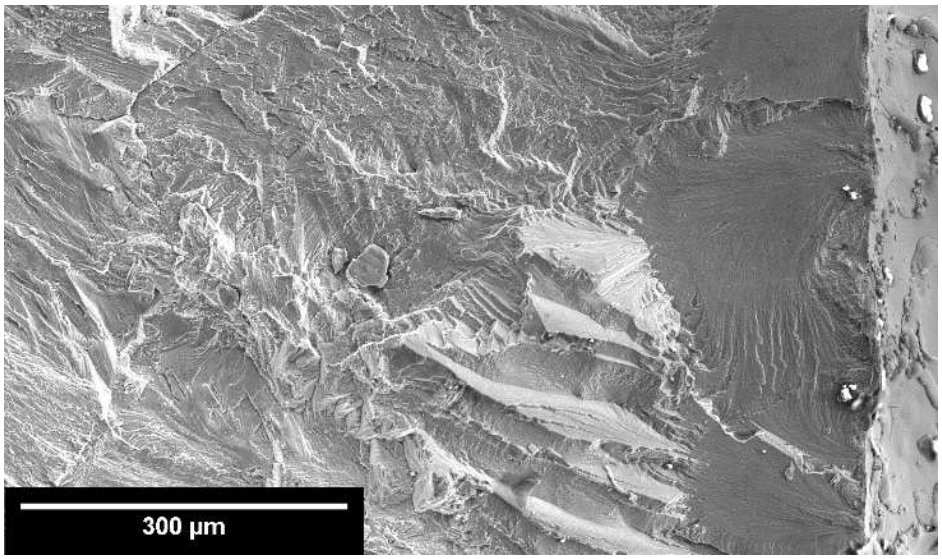

Figure 4.29: Fatigue crack initiation of the representative quench delay (90 seconds) specimen with faceted initiation and propagation. Note the EDM wire cut notch at the far right of the image highlights a recast surface. Tensile loading direction in these specimens is in and out of plane, with crack growth from right to left of the image.

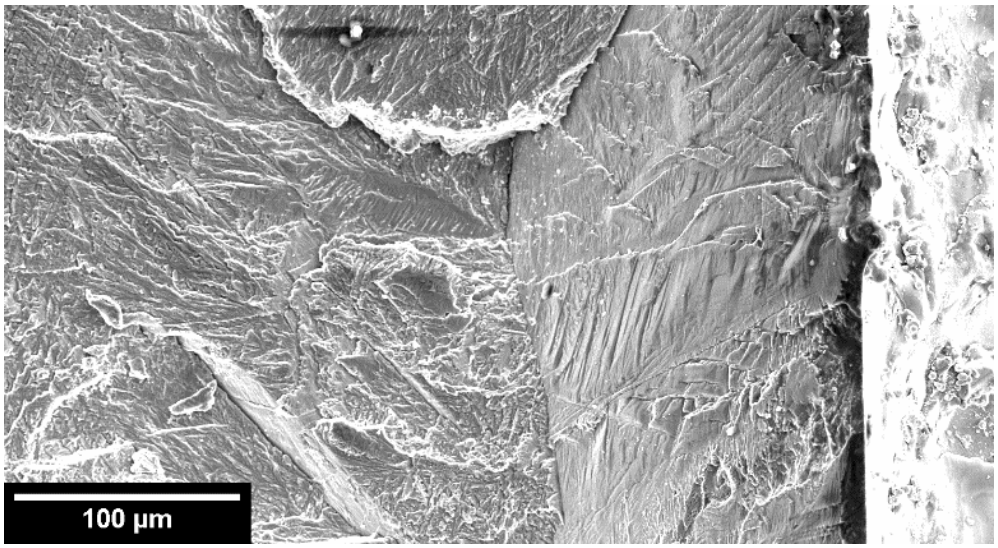

Figure 4.30: Fatigue crack initiation of the minimal quench delay specimen (less than 5 seconds), showing crack initiation and propagation appearing to follow prior-ß grain boundaries. Note the EDM wire cut notch at the far right of the image highlights a recast surface. Tensile loading direction in these specimens is in and out of plane, with crack growth from right to left of the image.

the differences of slope in the elastic region for the material do not signify different modulus of elasticity. Yield strength, ductility and other values of the plastic deformation region may not be appropriate to calculate as these specimens had a constant radius taper and not an appropriate ASTM E8 configuration.

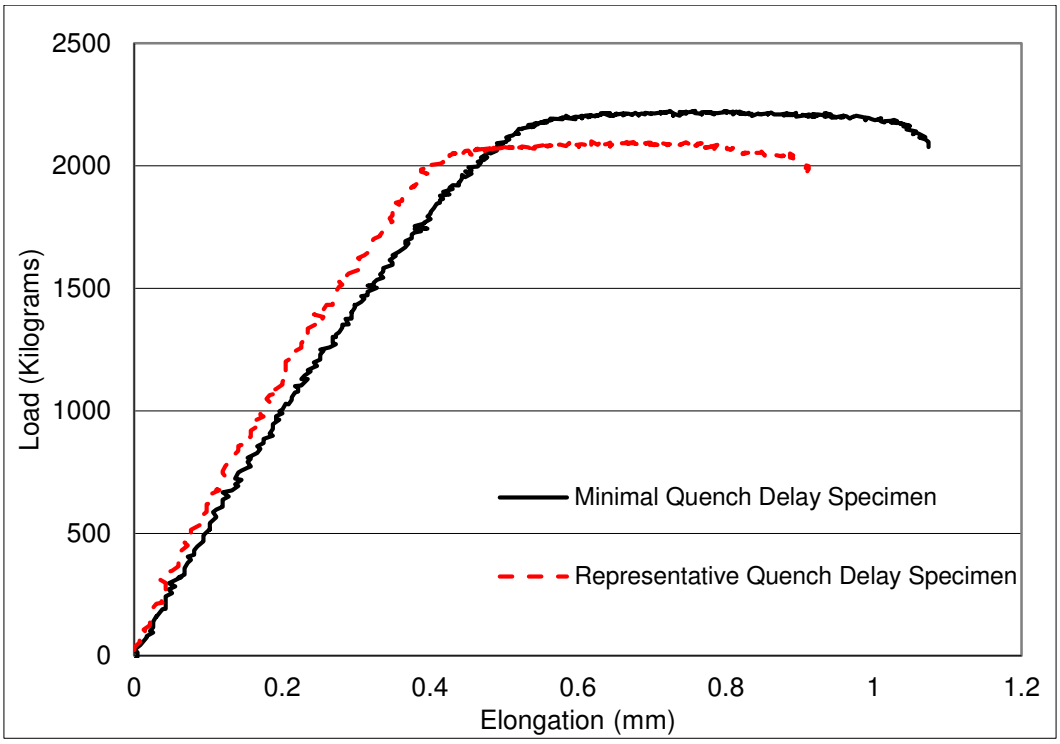

Figure 4.31: Tensile load versus displacement data comparing effects of minimal (< 5 seconds) versus representative (90 seconds) quench delays for ß-STOA heat treatments.

Microvickers hardness testing of the two heat treatment conditions showed nearly identical hardness results (Table 4.4), with an increased standard deviation of the data for the representative quench delay specimen. A possible answer for the latter result is the indentations were located on regions of various α colony sizes; larger α colonies were near the ß grain boundaries and smaller α colonies were near the center of the ß grains. Smaller α colony packet sizes would be expected to have higher hardness values, due to a more homogeneous strain accommodation of multiple orientations of α colonies interacting. This is supported by anisotropic deformation occurring for hardness indents in α colonies (Figure 4.32a), while multivariant α (Figure 4.32b) behaving more isotropic. For each heat treatment condition, 20 hardness indents were made.

Table 4.4: Microvickers hardness data comparing effects of quench delays

	Representative Quench Delay	*Minimal Quench Delay*
Average Hardness (HV)	*370*	*371*
Standard deviation (HV)	*18*	*12*

a. 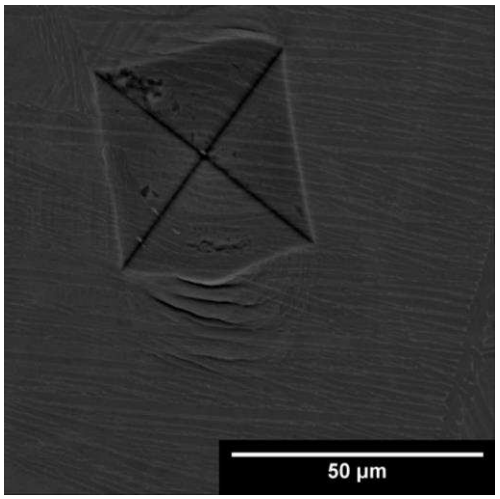

b. 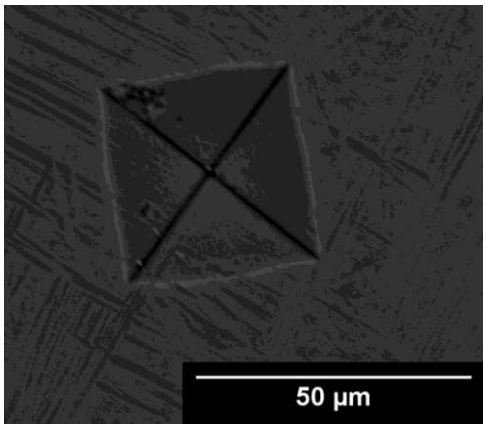

Figure 4.32: Vickers hardness indentations of representative quench delay specimens showing (a) anisotropic deformation in α colony. Note the grain boundary α on the lower right. An intragranular region of the same specimen (b) contains a multivariant α region and displays relatively more isotropic behavior.

CHAPTER 5: DISCUSSION

5.1 Initial Investigation

The initial motivation for this project was to determine the cause of the hydraulic actuators not meeting the required fatigue life during accelerated, representative service testing. Further goals were to recreate the cause of failure in a controlled manner, quantify its deleterious effects, and provide a method of alleviating the cause with data to support it. Failure analysis already underway prior to the author's involvement was directed at stress corrosion cracking, due to the tortuous and branched crack morphology. Prior to SEM-BSE imaging, the crack morphology (Figure 5.1a), which turned out to be the facet features (Figure 5.1b) was thought to be fractured titanium hydrides at the α/ß interface.

a) 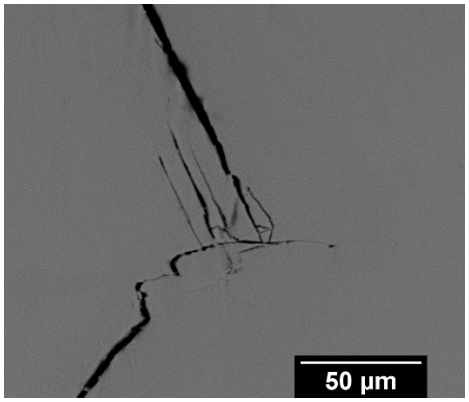

b) 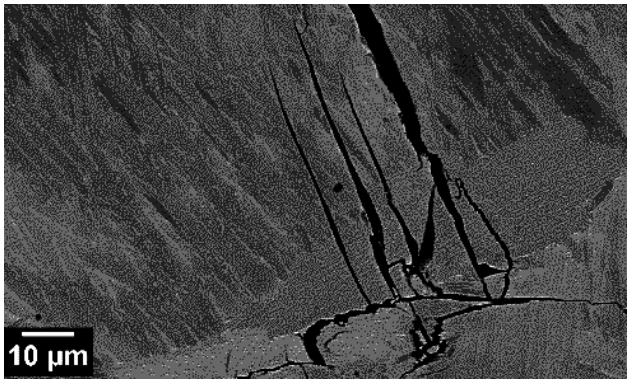

Figure 5.1: Parallel crack propagation in secondary electron imaging and back scattered electron imaging of the same feature. Propagation direction is top to bottom in these images, with tensile loading horizontally left and right.

This theory was supported at the time by previous experience with other material systems that showed susceptibility to hydrogen embrittlement, caused by electroplating of thick coatings similar to the cobalt phosphorus plating used on this actuator. However, the hydrogen-content, fracture surface and metallographic analysis did not support the hypothesis of hydrogen induced fatigue life degradation. Environmental and/or corrosion degradation of the hydraulic actuator in service was unsupported by existing literature, and further attempts to find experimental evidence of this were unsuccessful. With the ability to see the underlying microstructure morphology, two things became apparent: 1) the α lath morphology was not what was required by the material specification and 2) fatigue crack morphology and propagation was influenced by the α lath morphology.

5.2 Effects of Cooling Rate on α Morphology

For being such a widely used alloy, there have been few publications regarding the cooling rate effects on the ß → α transformation and morphology in Ti-6-4. The Jominy end-quench test performed by Ahmed et al. [1] provides some data for construction of a CCT curve, but is limited by the varying cooling rates as a function of temperature. Ahmed's results show significantly higher cooling rates required to produce multivariant α lath microstructures. Additionally, Ahmed proposed a massive transformation to describe the colony formation of α.

The results in this current study are based upon independent specimens for each data point, without unintentional aging of the material, due to decreased cooling rates at intermediate temperatures. The α colony formation is shown to occur through a two-step process: 1) allotriomorphic GBα precipitating along prior ß grains, followed by 2) side plate formation and growth through a diffusional transformation. Vanadium segregation to the ß matrix is apparent in the SEM-BSE images (Figure 4.8), indicating a long range diffusive component that is inconsistent with a partitionless, short range diffusional/reconstructive massive transformation. Furthermore, unlike massive transformations, these α colony formations appear to have no minimum required cooling rate for creation. It is apparent from the preliminary quench delay specimens (Figure 4.8) that the contrast in SEM-BSE is due to atomic weight contrast (i.e., vanadium partitioning out of the α phase, creating a darker region) rather than channeling contrast. This is evident as the GBα and side plates are darker than the ß matrix, while the intragranular α' laths show much less contrast.

Utilizing the dilatometer to provide controlled temperatures, these α colony formations were predominately suppressed with cooling rates of approximately 5 °C/s or higher. Thermal modeling of a large forging, using the experimentally derived convective cooling coefficient, confirmed that a properly controlled QD can achieve cooling rates required to suppress large α colony formation for this geometry. A second actuator was provided late in this study and demonstrated a microstructure indicative of short QD, containing only small α colony packets of 30 µm at triple junctions and supporting the thermal modeling results. Note that increased section thickness and part size does limit the achievable cooling rates, due to low thermal conductivity of titanium. Intensive quenching, a high pressure application of water to break through steam-film barriers, is proposed to achieve higher cooling rates when necessary, particularly near the surface of the material.

In agreement with Sharma et al. [8], α colony formations were observed to be sourced from GBα, and did not form intragranularly as proposed by Ahmed et al. [1]. The α colonies that appear to be intragranularly formed, when viewing in 2-dimensions on a metallographic sample, are thought to be caused by a sectioning effect, as demonstrated by Sharma et al. [8]. The 'zig-zag' GBα was found to exist

at all transformation temperatures and cooling rates that promoted GBα, but the continuity increased with increasing transformation temperatures and decreasing cooling rates. It is believed that the existence of these features is more dependent upon the relative orientations of the $(110)_{ß}$ planes between neighboring grains, as proposed by Sharma et al. [8], rather than the transformation temperature and cooling rate.

Though not thoroughly explored in this study, EBSD analysis of α side plate formations in a single ß grain from a single GBα appear to grow in different directions, but share a common $(0001)_{\alpha}$ plane (Figure 4.21a). In addition, they appear to form in adjacent ß grains that share a common $\{110\}_{ß}$ plane (Figure 4.21b) and resulting $(0001)_{\alpha}$ plane. The crack morphology in these regions suggests a low impedance to crack propagation, as a result of the similarly aligned basal plane. Some parallel cracks were arrested at the ß grain, possibly due to stress shielding from other cracks. These α colony formations and orientations are in agreement with those explored by Bhattacharya in Figure 2.7 [10].

A particularly interesting result obtained by comparing the microstructures produced from the spectrum of cooling rates studied is the gradual transition in α morphology. As cooling rates increase and GBα becomes sparser and less continuous due to lower diffusion rates, the interwoven basketweave microstructure appears (Figure 4.14b) with α laths longer than the laths produced in α colony formation, despite having lower times at higher temperatures. This higher undercooling should produce a higher driving force for nucleation and growth with long-range diffusional growth components being less dominant. At the highest cooling rates tested, it is unclear whether these are short-range diffusional (reconstructive, without composition change) or truly pure displacive components. At relatively high cooling rates (Figure 4.9l) and undercoolings (Figure 4.15b), α laths precipitate from discontinuous GBα in a co-oriented manner. Dilatometry data in intermediate and relatively high cooling rates indicates diffusional transformations still occur, however the resulting microstructures can often resemble that of water quenched martensite and are often classified as such, based solely upon morphology.

5.3 Dislocation Motion and Microstructural Effects

As discussed previously, work performed by Savage et al. [20] provides a thorough basis for <a1> basal slip transmission through α-ß interfaces. Combined with QDs that produce α colonies sharing $(0001)_{\alpha}$ planes across ß grain boundaries, this allows for relatively-unimpeded dislocation motion. The high CRSS of the pyramidal slip systems and lack of twinning prevents <c+a> stress accommodation, limiting dislocations to planar features at low stresses and stress intensities. The planar slip prevents dislocation interactions and appreciable strain hardening for <a1> slip, until pileups at high angle grain boundaries where crack initiation may occur. The ease of <a1> basal slip compared to <a2> and <a3>

basal slip may contribute to the apparent preferred growth direction of the facet features shown in Figure 4.7.

The controlling microstructural unit (CMU) of α colony size proposed by Yoder et al. [40] for the mill annealed condition appears applicable for the QD microstructures as well. The short crack length regime is defined to exist until the cyclic plastic zone size is on the order of the CMU size, and then propagates in a microstructurally-sensitive manner. During short crack growth, LEFM and the cyclic plastic zone size are not technically valid due to anisotropic strain accommodation in the material. An approximate calculation of the cyclic plastic zone radius from the crack length and applied stress (Table 5.1) correlates with observations of facet features existing at crack lengths up to 2.5 mm away from the initiation. The α colonies observed were approximately 300 μm in width, which is near the magnitude of the cyclic plastic zone radius for this crack length.

Table 5.1: Increasing cyclic plastic zone radius as a function of crack length

Crack Length [μm]	*Cyclic Plastic Zone Radius [μm]*
2.5	*0.37*
25.4	*3.7*
127	*18*
254	*37*
1270	*186*
2540	*372*
6350	*931*

5.4 Fatigue Life Considerations

The deleterious effects of the QD are apparent from the rotating bending fatigue results and lead to a decrease in fatigue life in excess of two orders of magnitude. The shift in tensile strength due to the quench delay does not fully account for the difference in fatigue strength (by increasing the effective stress). A shift in applied stress of 5%, the difference in tensile strength of the quench delay conditions, creates a shift in fatigue life of less than a factor of two in the MMPDS data set (Figure 2.18), and does not account for the significant shift in fatigue life. Thus, the microstructural contributions due to the quench delay are more complex than lowering the S-N fatigue curve.

The total high cycle fatigue life of the material without notches or pre-cracking is dominated by the initiation stage of the crack, which is negatively impacted by the presence of GBα colonies. After initiation, the propagation rate is decreased by the tortuous crack path across α colonies and multi-variant α in the central regions of the grains; these features increase the resistance to crack propagation, as shown

by the tortuous fracture surface. In theory this may appear beneficial from the perspective of sacrificing total fatigue life for the sake of lower crack growth rates between inspection intervals; however, this assumes surface initiation is always present or that NDE techniques are capable of resolving these features. Sub-surface faceted initiation and growth has been shown to exist in fatigue specimens, but X-ray computed tomography was required for their detection [34]. Thus this does not appear to be a reliable manner to life limit aerospace components for this material condition. In all tests within this study, including the hydraulic actuator with a fractured brittle coating, surface initiation resulted from the loading conditions and/or stress concentrators. Subsurface facet formation for the microstructures produced by QDs needs further investigation. Therefore, it is recommended that the α colony formations should be limited by controlling and enforcing QD times. Recommended cooling rates are 5°C/s through the temperature range of 925-825°C to avoid these α colonies. Additionally, surface initiation may be suppressed by shot peening. DonXing et al. [41] demonstrated a two-fold increase in endurance limit for a titanium alloy by shot peening prior to the application of a hard, wear-resistant coating, in comparison to non-shot peened and coated material.

CHAPTER 6: CONCLUSIONS AND FUTURE WORK

The goals of this study were to (1) determine the cause of premature fatigue failure of the example hydraulic actuators, (2) to recreate it in a controlled manner, and (3) to quantify the decrease in fatigue life, and provide a method for improvement. The cause was shown to be a combined effect of the quench delay (QD) and the brittle coating, which together provided easy initiation of a fatigue crack. The QD produced GBα colonies that led to the formation of long, planar slip bands during fatigue; these led to fatigue crack initiation. This result was reproduced using rotating bending fatigue tests that demonstrated a two orders of magnitude fatigue life reduction due to these α colonies. Fatigue crack propagation rates determined from da/dN vs. ΔK tests showed a slight decrease in crack growth rates for the QD microstructure. This increased crack growth resistance was caused by crack bifurcation, roughness induced crack closure, and inducing mixed modes of stress. Since the fatigue life is largely initiation controlled, recommendations for alleviating the degradation in fatigue life include: 1) controlled transfer time between the furnace and water quenching operation to avoid cooling between 925°C and 825°C at a rate slower than 5°C/s and 2) shot peening of fatigue critical surfaces.

Future research should include further ß →α transformation studies, quantitative tilt fractographic analysis, and short crack growth rate analysis. Controlling the ß thickness between α laths by slow cooling rates is thought to be a possible method of inducing ß cross slip and preventing planar dislocation motion. However, this likely has secondary effects on mechanical properties due to increased GBα thickness. Higher ß phase fraction alloys may be more suitable for the ß annealed conditions than these near-α titanium alloys. Texture analysis of the rotating bending fatigue and fatigue crack growth rate specimens would provide useful data to supplement the fatigue data. The existing fracture surfaces harvested from the hydraulic actuators provide large amounts of initiation and propagation facet features created through a biaxial stress state with a stress ratio of 1:2 that could be used for statistical quantitative tilt fractography to contribute to existing literature data sets [30][31] for the relative orientations of the loading directions, α basal plane and facet plane. Finally, fatigue crack growth rates for specimens that utilize a reduced gauge section without a starter notch or crack may capture the crack initiation stages in a more realistic manner. The previously used electrical potential differential (EPD) method would allow for high resolution of small crack propagation rates as well as any internal crack initiation.

REFERENCES

[1] T. Ahmed and H. J. Rack, "Phase transformations during cooling in α+β titanium alloys," *Mater. Sci. Eng. A*, vol. 243, no. 1–2, pp. 206–211, 1998.

[2] M. Peters and C. Leyens, *Titanium and Titanium Alloys: Fundamentals and Applications*, vol. 1. Wiley, 2003.

[3] R. Boyer, *Materials Properties Handbook: Titanium Alloys*. ASM International, 1994.

[4] S. L. Semiatin, J. C. Soper, and I. M. Sukonnik, "Short-time beta grain growth conventional kinetics alloy," *Acta Metall.*, vol. 44, no. 5, pp. 1979–1986, 1996.

[5] DOD, "MIL-H-81200," 1968.

[6] F. J. Gil, M. P. Ginebra, J. M. Manero, and J. A. Planell, "Formation of α Widmanstatten structure: effects of grain size and cooling rate on the Widmanstatten morphologies and on the mechanical properties in Ti6Al4V alloy," *J. Alloys Compd.*, vol. 329, pp. 142–152, 2001.

[7] D. A. Porter and K. E. Easterling, *Phase Transformations in Metals and Alloys*. Hong Kong: Chapman & Hall, 1992.

[8] H. Sharma, S. M. C. van Bohemen, R. H. Petrov, and J. Sietsma, "Three-dimensional analysis of microstructures in titanium," *Acta Mater.*, vol. 58, no. 7, pp. 2399–2407, 2010.

[9] A. J. Williams, R. W. Cahn, and C. S. Barrett, "The crystallography of the β-α transformation in titanium," *Acta Metall.*, vol. 2, no. 1, pp. 117–128, 1954.

[10] D. Bhattacharyya, G. B. Viswanathan, R. Denkenberger, D. Furrer, and H. L. Fraser, "The role of crystallographic and geometrical relationships between α and ß phases in an α/ß titanium alloy," *Acta Mater.*, vol. 51, no. 16, pp. 4679–4691, 2003.

[11] C. Hammond and P. Kelly, "The crystallography of titanium alloy martensites," *Acta Metall.*, vol. 17, pp. 869–882, 1969.

[12] K. Bhattacharya, S. Conti, G. Zanzotto, and J. Zimmer, "Crystal symmetry and the reversibility of martensitic transformations.," *Nature*, vol. 428, no. 6978, pp. 55–59, 2004.

[13] S. G. Srinivasan, D. M. Hatch, H. T. Stokes, A. Saxena, R. C. Albers, and T. Lookman, "Mechanism for BCC to HCP Transformation: Generalization of the Burgers Model," p. 20, 2002.

[14] Duerig, Albrecht, Richter, and Fischer, "Formation and Reversion of Stress Induced Martensite in Ti- 10V- 2Fe- 3Al," *Acta Metall.*, vol. 30, pp. 2161–2172, 1982.

[15] S. Banerjee and P. Mukhopadhyay, *Phase Transformations: Examples from Titanium and Zirconium Alloys*. Oxford: Elsevier, 2007.

[16] H. Beladi, Q. Chao, and G. S. Rohrer, "Variant selection and intervariant crystallographic planes distribution in martensite in a Ti-6Al-4V alloy," *Acta Mater.*, vol. 80, pp. 478–489, 2014.

[17] H. Li, D. E. Mason, T. R. Bieler, C. J. Boehlert, and M. A. Crimp, "Methodology for estimating the critical resolved shear stress ratios of α-phase Ti using EBSD-based trace analysis," *Acta Mater.*, vol. 61, no. 20, pp. 7555–7567, 2013.

[18] D. Hull and D. J. Bacon, *Introduction to Dislocations*, Fifth. Burlington: Elsevier, 2011.

[19] G. Welsch, G. Lütjering, K. Gazioglu, and W. Bunk, "Deformation characteristics of age hardened

Ti-6Al-4V," *Metall. Trans. A*, vol. 8, no. 1, pp. 169–177, 1977.

[20] M. F. Savage, J. Tatalovich, and M. J. Mills, "Anisotropy in the room-temperature deformation of α – β colonies in titanium alloys: role of the α – β interface," *Philos. Mag.*, vol. 84, no. 11, pp. 1127–1154, 2004.

[21] B. M. Institute, *Metallic Materials Properties Development and Standardization (MMPDS-10)*, 1st ed., no. January. District of Columbia: Battelle Memorial Laboratories, 2015.

[22] D. R. Tobergte and S. Curtis, *ASM Handbook Volume 19 - Fatigue and Fracture*, Second., vol. 19. ASM International, 1996.

[23] "ASTM E647-15: Standard Test Method for Measurement of Fatigue Crack Growth Rates," West Conshohocken, 2016.

[24] R. Hertzberg, *Deformation and Fracture Mechanics of Engineering Materials*, Second. Hoboken: Wiley, 1996.

[25] G. R. Yoder, L. A. Cooley, T. W. Crooker, M. Science, and T. Division, "Quantitative analysis of microstructural effects on fatigue crack growth in Widmanstatten Ti-6Al-4V and Ti-8Al-1Mo-1V," vol. 11, pp. 805–816, 1979.

[26] S. Shademan, V. Sinha, A. B. O. Soboyejo, and W. O. Soboyejo, "An investigation of the effects of microstructure and stress ratio on fatigue crack growth in Ti-6Al-4V with colony α/ß microstructures," *Mech. Mater.*, vol. 36, no. 1–2, pp. 161–175, 2004.

[27] D. Eylon, J. A. Hall, C. M. Pierce, and D. L. Ruckle, "Microstructure and mechanical properties relationships in the Ti-11 alloy at room and elevated temperatures," *Metall. Trans. A*, vol. 7, no. 11, pp. 1817–1826, 1976.

[28] G. R. Yoder, L. a. Cooley, and T. W. Crooker, "Observations on microstructurally sensitive fatigue crack growth in a Widmanstätten Ti-6Al-4V alloy," *Metall. Trans. A*, vol. 8, no. 11, pp. 1737–1743, 1977.

[29] M. R. Bache, "A review of dwell sensitive fatigue in titanium alloys: The role of microstructure, texture and operating conditions," *Int. J. Fatigue*, vol. 25, no. 9–11, pp. 1079–1087, 2003.

[30] A. L. Pilchak, "Fatigue crack growth rates in alpha titanium: faceted vs. striation growth," *Scr. Mater.*, vol. 68, no. 5, pp. 277–280, 2013.

[31] A. L. Pilchak, A. H. Young, and J. C. Williams, "Stress corrosion cracking facet crystallography of Ti-8Al-1Mo-1V," *Corros. Sci.*, vol. 52, no. 10, pp. 3287–3296, 2010.

[32] A. l. Pilchak, A. Bhattacharjee, a. H. Rosenberger, and J. C. Williams, "Low stress intensity faceted crack growth in titanium alloys," *Int. J. Fatigue*, vol. 31, no. 5, pp. 989–994, 2009.

[33] A. Pilchak, M. Brandes, R. Williams, and J. Williams, "The role of facet formation in fatigue crack initiation and early stages of crack growth," no. February, pp. 1–39, 2013.

[34] A. L. Pilchak and J. C. Williams, "Observations of facet formation in near-α titanium and comments on the role of hydrogen," *Metall. Mater. Trans. A Phys. Metall. Mater. Sci.*, vol. 42, no. 4, pp. 1000–1027, 2011.

[35] B. F. Brown, "Stress corrosion cracking in high strength steels and in titanium and aluminum alloys," *Nav. Res. Lab.*, vol. ADA030783, 1972.

[36] D. A. Meyn, "An analysis of frequency and amplitude effects on corrosion fatigue crack

propagation in Ti-8Al-1Mo-1V," *Metall. Mater. Trans. A*, vol. 2, no. 3, pp. 853–865, 1971.

[37] W. J. Evans and M. R. Bache, "Dwell and environmental aspects of fatigue in alpha/beta titanium alloys," *Miner. Met. Mater. Soc.*, 1999.

[38] D. S. Shih, I. M. Robertson, and H. K. Birnbaum, "Hydrogen embrittlement of α titanium: in situ TEM studies," *Acta Metall.*, vol. 36, no. 1, pp. 111–124, 1988.

[39] R. J. H. Wanhill, "Environment and frequency effects during fatigue crack propagation in Ti-2.5Cu Sheet at room temperature.," *Corrosion*, vol. 30, no. 1. NACE, Amsterdam, pp. 28–35, 1974.

[40] G. R. Yoder, L. A. Cooley, T. W. Crooker, M. Science, and T. Division, "Quantitative analysis of microstructural effects on fatigue crack growth in widmanstatten Ti-6Al-4V and Ti-8Al-1Mo-1V," vol. 11, pp. 805–816, 1979.

[41] D. Du, D. Liu, B. Meng, and X. Zhang, "Effects of pretreatment and HVOF sprayed cermet coating on fatigue properties of TC21 titanium alloy," *Sci. China Technol. Sci.*, vol. 56, no. 4, pp. 1029–1037, 2013.